The effect of the relativistic Doppler in the clustering of multiple tracers of Dark Matter

Miguel Godinho
Master in Physics
Department of Physics and Astronomy
Faculty of Sciences of the University of Porto
2025

The effect of the relativistic Doppler in the clustering of multiple tracers of Dark Matter

Miguel Godinho

Dissertation carried out as part of the Master in Physics

Department of Physics and Astronomy

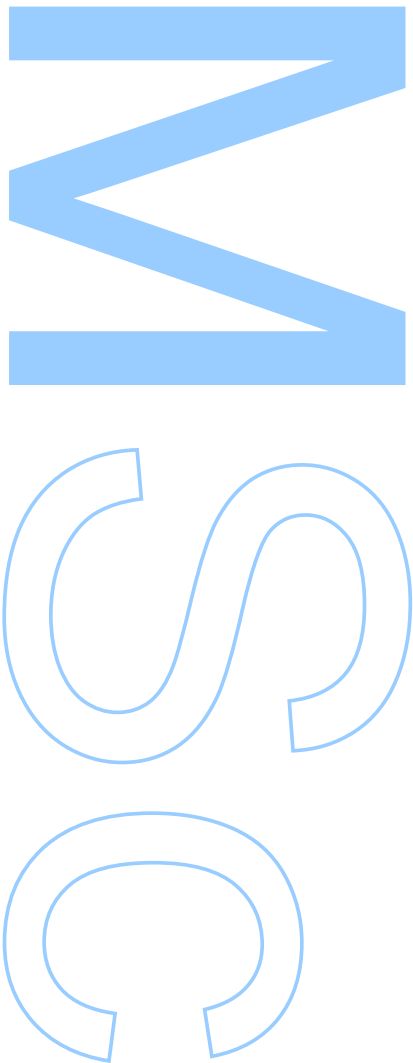
2026

Supervisor

Dr. José Fonseca, Assistant Researcher,
Institute of Astrophysics and Space Sciences,
Faculty of Sciences of the University of Porto

Cosupervisor

Prof. Stefano Camera, Associate Professor,
Department of Physics,
University of Turin



UNIVERSITY OF PORTO

MASTERS THESIS

The effect of the relativistic Doppler in the clustering of multiple tracers of Dark Matter

Author:
Miguel GODINHO

Supervisor:
Dr. José FONSECA

Co-supervisor:
Prof. Stefano CAMERA

A thesis submitted in fulfilment of the requirements
for the degree of MSc. Physics

at the

Faculty of Sciences of the University of Porto
Department of Physics and Astronomy

February 12, 2026

À minha família, pelo amor e apoio constante ao longo de todos estes anos.

" Tenho em mim todos os sonhos do mundo. "

Álvaro de Campos, "Tabacaria"

Acknowledgements

When I first came to University of Porto, I was not sure if it had been the right decision, and I struggled to adapt. However, with the help of many people, I was able to overcome these difficulties and succeed. I cannot miss the opportunity to reflect and thank those who have supported me in achieving this important milestone in my life.

First and foremost, I want to thank my family, especially my mother, grandmother, and aunt, who have supported me not only throughout this journey but throughout my entire life in every possible way, allowing me to reach this step. I cannot put into words how grateful I am, nor how much they worked and helped along the way to make this possible. I am also deeply thankful to my brothers who, each in their own way, have been present throughout this path.

I would also like to thank my friends, roommates, and colleagues who helped me reach this goal, whether through study sessions, words of encouragement, moments of fun, or our shared activities. Their companionship and support made daily life not only easier but also much more rewarding.

I am also deeply grateful to my supervisors, Dr. José Fonseca and Prof. Stefano Camera, for introducing me to such a fascinating topic, and for their guidance, discussions, and encouragement that brought me to this point. This was not what I had initially expected to pursue academically when I came to Porto, but working on this thesis has been a deeply rewarding experience, one in which I learned a lot but also had a blast doing it.

Finally, I want to acknowledge the journey itself. During my time in Porto, I was able to study physics and the universe in depth, but also broaden my horizons by exploring economics and engineering. I was fortunate to take part in extracurricular activities that fulfilled me both personally and academically. This path was not always easy and came with many frustrations, yet those challenges ultimately helped me grow and prepared me for what comes next, making the experience all the more rewarding. I truly enjoyed it as a whole.

All of this, the people who accompanied me and the journey itself, has led me to this milestone, and I will carry it with me forever.

UNIVERSITY OF PORTO

Abstract

Faculty of Sciences of the University of Porto
Department of Physics and Astronomy

MSc. Physics

The effect of the relativistic Doppler in the clustering of multiple tracers of Dark Matter

by Miguel GODINHO

The clustering of galaxies encodes valuable information about both the distribution of matter and the underlying laws of gravity. In addition to the dominant redshift-space distortions, relativistic effects introduce subdominant but potentially detectable contributions. Among these, the relativistic Doppler effect is of particular interest, as it provides a direct test of the Euler equation with in General Relativity and may serve as a probe of modified gravity theories. In Fourier space, this effect appears as an imaginary component that is suppressed in the auto power spectrum but preserved in cross-correlations, making it a promising observable.

In this thesis, we develop and assess novel observational strategies aimed at enhancing the detectability and parameter inference of the relativistic Doppler effect in galaxy clustering. The analysis is built upon cross-power spectra, focusing on both their multipole expansions and their decomposition into symmetric (real part) and antisymmetric (imaginary part) contributions. To this end, we combine signal-to-noise ratio studies with Fisher forecast techniques, applied to a DESI-like Bright Galaxy Sample at low redshift, in order to quantify parameter constraints and investigate degeneracies.

The results obtained from the multipole expansion did not prove consistent, as the relative errors obtained, when compared with those from the full power spectrum, fluctuated between being larger or smaller without any clear justification. Therefore, no robust conclusions could be drawn, indicating the need for further investigation. On the other hand, the decomposition into real and imaginary estimators demonstrates that Doppler parameters can be constrained with relative errors ranging from approximately 32% to 2%

across redshifts, while the global amplitude parameter A_D can be measured with a precision of order 7×10^{-4}, representing a substantial improvement over previous results. These findings underscore the potential of upcoming large-scale surveys to detect relativistic Doppler signatures, offering not only observational guidance but also theoretical implications for testing General Relativity on cosmological scales.

UNIVERSIDADE DO PORTO

Resumo

Faculdade de Ciências da Universidade do Porto
Departamento de Física e Astronomia

Mestrado em Física

O efeito Doppler relativístico na aglomeração de múltiplos traçadores de Matéria Escura

por Miguel GODINHO

O estudo da distribuição em larga escala de galáxias fornece informações cruciais sobre a composição do Universo e sobre as leis fundamentais da gravidade. Para além das distorções de espaço de redshift, efeitos relativistas introduzem contribuições subdominantes, mas potencialmente detetáveis. Entre estes, o efeito Doppler relativista é particularmente relevante por permitir testar diretamente a equação de Euler no contexto da Relatividade Geral, constituindo também uma possível via para sondar teorias de gravidade modificada. No espaço de Fourier, este efeito manifesta-se como uma componente imaginária que é suprimida no autoespetro de potência, mas preservada em correlações cruzadas, tornando-se assim um observável promissor.

Nesta dissertação, desenvolvemos e avaliamos novas estratégias observacionais destinadas a melhorar a detectabilidade e a inferência de parâmetros do efeito Doppler relativístico no agrupamento de galáxias. A análise baseou-se em espectros de potência cruzada, com foco nas suas expansões multipolares e na sua decomposição em contribuições simétricas (parte real) e antissimétricas (parte imaginária). Para tal, combinamos estudos da relação sinal-ruído com técnicas de previsão de Fisher, aplicadas a uma amostra de galáxias brilhantes semelhante à DESI em baixo redshift, a fim de quantificar as restrições dos parâmetros e investigar as degenerações.

Os resultados obtidos a partir da expansão em multipolos não se mostraram consistentes, uma vez que os erros relativos obtidos, quando comparados com os do espectro de potência completo, oscilaram entre serem maiores ou menores sem qualquer justificação clara. Assim, não foi possível retirar conclusões robustas, o que indica a necessidade de

uma investigação mais aprofundada. Por outro lado, a decomposição em estimadores reais e imaginários demonstrou que os parâmetros Doppler podem ser restringidos com erros relativos que variam de aproximadamente 32% a 2% em todos os redshifts, enquanto o parâmetro de amplitude global A_D pode ser medido com uma precisão da ordem de 7×10^{-4}, representando uma melhoria substancial em relação aos resultados presentes na literatura. Essas descobertas ressaltam o potencial de futuras pesquisas em grande escala para detectar assinaturas Doppler relativísticas, oferecendo não apenas orientação observacional, mas também implicações teóricas para testar a Relatividade Geral em escalas cosmológicas.

Contents

Acknowledgements vii

Abstract ix

Resumo xi

Contents xiii

List of Figures xv

Notation xvii

1 Introduction 1
- 1.1 Motivation . . . 1
- 1.2 Objectives . . . 2
- 1.3 Thesis Outline . . . 3

2 Cosmology of the homogeneous and isotropic background universe 5
- 2.1 Friedmann-Lemaître-Robertson-Walker Universe . . . 6
- 2.2 Friedmann Equations and the Standard Model of Cosmology . . . 8
- 2.3 Cosmological Distances . . . 10

3 Effect of Peculiar Velocities in Large-Scale Matter Distribution 13
- 3.1 Tracers of Large-Scale Matter Distribution . . . 13
- 3.2 "Newtonian" Distortion of the Observed Density Field of Number of Galaxies 15
  - 3.2.1 Perturbations on Observed Position . . . 15
  - 3.2.2 Perturbations on Observed Number of Galaxies . . . 16
- 3.3 Relativistic Doppler Effect . . . 19

4 The Impact of Doppler Effect in the Galaxy Power Spectrum 23
- 4.1 Matter Power Spectrum . . . 23
- 4.2 Galaxy Power Spectrum . . . 25
- 4.3 Multipoles of the Cross Power Spectrum . . . 26
- 4.4 Discrete Fourier Transform and Estimators of the Galaxy Power Spectrum . 29

5 Prospects of Constraining the Doppler effect in Future Surveys 35
- 5.1 DESI-like low redshift Bright Galaxy Sample . . . 35

5.2 Signal-to-Noise Ratio Analysis . . . 36
5.2.1 SNR of Legendre Multipoles of the Cross-Power Spectrum . . . 37
5.2.2 SNR of the Anti-Symmetric Estimator of the Cross Power Spectrum and Its Legendre Multipoles . . . 39
5.3 Parameter Analysis . . . 42
5.3.1 Fisher Information Matrix . . . 42
5.3.2 Degeneracies Analysis . . . 45
5.3.3 Relative Errors Analysis . . . 49
α Parameter Set . . . 49
A_D Parameter Set . . . 50
Discussion . . . 51

6 Conclusion **53**

A On the Derivation of the Discrete Fourier Power Spectrum and Poisson Noise **57**

B Detailed Derivation of the Covariance of the Real, Imaginary, and Mixed Components of the Cross Power Spectrum **61**

C Detecting the Relativistic Doppler Effect with Auto- and Cross-Power Spectra **65**
C.1 Analysis Setup . . . 65
C.2 Detection Significance Analysis . . . 66
C.3 Parameter Constraints . . . 68

Bibliography **71**

List of Figures

2.1 The Universe can be foliated into spatial hypersurfaces of constant curvature: flat ($K = 0$), spherical ($K > 0$), or hyperbolic ($K < 0$) [5]. 7

2.2 Expansion of the Universe illustrated by a comoving coordinate grid. The comoving separation between two points, r_0 and r_1, remains constant throughout cosmic evolution, while the corresponding physical distance grows proportionally to the scale factor [4]. 8

3.1 Schematic representation of the challenges involved in measuring the three-dimensional galaxy density field. Galaxies are selected within a narrow redshift interval (solid arcs) centered at the mean redshift $\bar{z}$ (dotted arc). A galaxy is observed at an angular position $\hat{\boldsymbol{n}}$ on the sky with measured redshift z. It is then assigned the apparent comoving position $\boldsymbol{r}_{\rm obs}$, which differs from its true position $\boldsymbol{r}$ because the distance–redshift relation is perturbed by the Doppler effect arising from the galaxy's line-of-sight velocity component, $u_{\parallel}$ [4]. 17

3.2 Ratio of $\left(b_g + f\mu^2\right) / \left(\alpha_g f\mathcal{H}\mu/k\right)$ for the different $\bar{z} = (0.133, 0.3, 0.45)$, for the bright subsample (see Section 5.1). Relativistic effects are included in the calculation (which will be introduced in the next Section). 19

4.1 Matter power spectrum, $P_m(k)$, evaluated at redshift $z = 0.467$ 24

4.2 Amplitudes of the different terms of the cross spectrum, $P_{gg'}$ evaluated $\bar{z} = 0.467$), using the BGS (see Section 5.1). Here $\propto k^0$ refers to the term $\left(b_g + f\mu^2\right)\left(b_{g'} + f\mu^2\right)$, $\propto k^1$ to $\frac{\mathcal{H}}{k}\left[\alpha_g\left(b_{g'} + f\mu^2\right) - \alpha_{g'}\left(b_g + f\mu^2\right)\right] f\mu$, $\propto k^2$ to $\frac{\mathcal{H}^2}{k^2}\alpha_g\alpha_{g'}f^2\mu^2$. 26

4.3 Legendre multipoles ($\ell = 0, 1, 2, 3$) of the cross-power spectrum $\mathcal{P}_{gg'}(k)$ evaluated at $\bar{z} = 0.467$), using the BGS (see Section 5.1). For reference, these results are compared against the underlying matter power spectrum. . 29

5.1 SNR of the Legendre multipoles ($\ell = 0, 1, 2, 3$) of the cross-power spectrum $\mathcal{P}_{gg'}$ for three mean redshifts ($\bar{z}_1 = 0.133$, $\bar{z}_2 = 0.300$, and $\bar{z}_3 = 0.467$) with the BGS. Each panel corresponds to a different multipole order. The markers represent the discrete values in k, while the solid line denotes the fitted function. 38

5.2 SNR of the imaginary power spectrum as a function of the wavenumber k for three mean redshifts forecasted with the BGS sample. Dashed grey line represent SNR = 10. 40

5.3 SNR of the legandre multipoles of the imaginary power spectrum as a function of the wavenumber k for three mean redshifts forecasted with the BGS sample. Dashed grey line represent SNR $= 10$. 41

C.1 Detection significance of the relativistic Doppler contribution for the model described in Section 5.1, assuming full-sky coverage. The test statistic Δ^2_χ is evaluated with respect to the null hypothesis of no Doppler contribution to the galaxy power spectrum. The colour coding is as follows: orange/yellow for the auto-correlation power spectrum of the faint sample, green for the auto-correlation of the bright sample, and red for the cross-correlation between the faint and bright samples. 67

C.2 Detection significance of the relativistic Doppler contribution for the model described in Section 5.1. The test statistic Δ^2_χ is evaluated with respect to the null hypothesis of no Doppler contribution to the galaxy power spectrum. The colour coding is as follows: orange/yellow for the auto-correlation power spectrum of the faint sample, green for the auto-correlation of the bright sample, and red for the cross-correlation between the faint and bright samples. 68

C.3 Relative errors on the amplitudes A_N, A_K, and A_D obtained for survey areas of 10,000 deg^2 and full sky coverage. The dashed horizontal lines indicate the maximum errors reported in [16]: A_D 0.4, A_N 0.002, and $A_K < 0.01$. The black dashed line marks the 1σ level. 69

C.4 Relative errors on the amplitudes A_N and A_K for the survey area of 10,000 deg^2, obtained using the Doppler-only parameter set θ_1 and the extended set θ_{1+}. 70

Notation

Derivatives with respect to physical (cosmic) time t are denoted by a prime, while derivatives with respect to conformal time η are denoted by a dot,

$$t = \text{physical (cosmic) time}, \qquad \frac{dX}{dt} \equiv X',$$
$$\eta = \text{conformal time}, \qquad \frac{dX}{d\eta} \equiv \dot{X}.$$

Spatial three-vectors are denoted by bold symbols, e.g. $\mathbf{x}$, whereas four-dimensional spacetime vectors are written as $x = (x^\mu)$.

The metric signature $(-,+,+,+)$ is adopted throughout. The Fourier transform is defined as

$$f(\mathbf{k}) = \int d^3x\, f(\mathbf{x})\, e^{-i\mathbf{k}\cdot\mathbf{x}},$$

so that the inverse relation is

$$f(\mathbf{x}) = \frac{1}{(2\pi)^3} \int d^3k\, f(\mathbf{k})\, e^{i\mathbf{k}\cdot\mathbf{x}}.$$

Natural units are employed throughout, with the speed of light, Planck's constant, and Boltzmann's constant set to unity: $c = \hbar = k_B = 1$.

The symbol $\equiv$ is used to denote a definition, whereas $\approx$ indicates an approximate equality.

Chapter 1

Introduction

1.1 Motivation

Cosmology has undergone remarkable progress over the past decades, driven by observations of the Cosmic Microwave Background [1] and Type Ia supernovae [2, 3], which led to the establishment of the standard model of cosmology. This model This model successfully accounts for the history of the Universe [4, 5]. At the same time, the advent of large galaxy surveys, both in terms of the number of observed objects and the surveyed volume, has enabled detailed studies of the large-scale distribution of matter. These surveys provide a powerful tool to probe fundamental physical processes in much greater depth, as will be explored throughout this thesis.

Galaxies are the primary tracers of this underlying matter distribution. What we actually observe from them is the light carried by photons, whose wavelength is stretched by the expansion of the Universe. On top of this global redshift, additional distortions arise due to the galaxies' peculiar motions and relativistic effects, which perturb the observed signal before it reaches us. As a result, the clustering pattern inferred from galaxy surveys is not a direct image of the underlying matter density field, but rather a combination of the cosmological redshift and these secondary contributions [6–11].

Among the various effects that contribute to these distortions, the relativistic Doppler effect is of particular interest. Although subdominant, it encodes valuable information about the dynamics of galaxies and offers the opportunity to test the Euler equation within General Relativity, thereby providing a novel probe of gravity on cosmological scales [12–16].

In Fourier space, the relativistic Doppler effect gives rise to an imaginary component of the density contrast. In scales well inside of the horizon, this component is largely suppressed in auto-power spectra, where it contributes only through its real projection, but is preserved in cross-power spectra, which retain both real and imaginary parts and thereby recover the signal on smaller scales [14–16]. In particular, [16] demonstrated that employing cross-power spectra showed that employing cross-power spectra yields good results for the detectability and parameter constraints of the Doppler effect. Moreover, although focused on gravitational redshift, [17] showed that using an estimator based on the imaginary component of the cross-power spectrum yields a favorable signal-to-noise ratio. This suggests that constructing such an estimator while accounting for the Doppler effect could lead to improved detectability of this signal.

In practice, however, analyzing the full cross-power spectrum, characterized by the wavenumber k and the directional cosine μ between the wavevector and the line of sight, is computationally demanding, owing to the large amount of data spanning both k and μ. For this reason, the Legendre multipole expansion in μ is frequently used as an alternative. Although multipole moments involve some loss of information, previous studies have shown that including terms up to the hexadecapole recovers nearly the same constraining power as the full spectrum [18]. Attempts to detect the Doppler effect with multipoles have been made, but only in the context of auto-power spectra [12]. This opens the possibility of applying a multipole expansion to cross-power spectra, where the odd multipoles in particular allow the Doppler contribution to be isolated [13].

The relevance of these approaches is twofold: observationally, they offer optimized strategies for detecting relativistic Doppler signatures in forthcoming surveys; theoretically, they provide a null test of testing General Relativity and alternative gravity models on cosmological scales.

1.2 Objectives

This thesis is guided by two main objectives. First, we aim to evaluate the potential loss of information arising from the use of Legendre multipoles in constraining the Doppler effect within the cross-power spectrum. Second, we seek to investigate the performance of an estimator specifically designed to isolate the imaginary part of the cross-power spectrum. More concretely, the work is structured around the following goals:

1. Provide an introduction and overview of the theoretical framework underlying the cross-power spectrum.

2. Develop the Legendre multipole expansion and construct an estimator for the imaginary component of the cross-power spectrum.

3. Assess the detectability of these observables through signal-to-noise ratio analyses, identifying which data vectors can realistically constrain the Doppler effect.

4. Quantify the achievable parameter constraints via Fisher forecast studies, including analyses of parameter degeneracies and relative errors.

5. Discuss the broader implications of these findings for the design and optimization of future cosmological surveys.

By pursuing these objectives, the thesis aims to bridge the gap between theoretical predictions of relativistic effects and their observational prospects, thereby offering guidance on how cosmological surveys can be optimized to detect them.

For the computational forecasts and numerical results, the analysis will rely on `CAMB` [19], in which we will be using a DESI-like low-redshift Bright Galaxy Sample* [15, 16, 20] in a ΛCDM universe† [21].

1.3 Thesis Outline

The thesis is organized as follows. Chapter 2 introduces the homogeneous and isotropic background universe, reviewing the standard cosmological framework and the role of dark matter. Chapter 3 discusses the impact of peculiar velocities and relativistic corrections on galaxy clustering. In Chapter 4, I present the theoretical description of the Doppler effect in the auto and cross correlation galaxy power spectrum, its multipole decomposition and of estimators. Chapter 5 contains the Fisher forecast analysis for a Dark Energy Spectroscopic Instrument-like sample, including signal-to-noise calculations and parameter constraints. In Chapter 6, we provide a brief review of our findings and outline future perspectives for subsequent work. Finally, Appendices A and B present more

*DESI stands for Dark Energy Spectroscopic Instrument, which will be described in more detail in Section 5.1.

†ΛCDM stands for Lambda Cold Dark Matter. The name reflects that the Universe is dominated by a cosmological constant Λ and by cold dark matter (CDM). We will return to this in Section 2.2.

detailed derivations, while Appendix C revisits part of the work related to the Doppler effect.

Chapter 2

Cosmology of the homogeneous and isotropic background universe

Modern cosmology is founded on the *cosmological principle*, which states that the Universe is homogeneous and isotropic when viewed on sufficiently large scales. This assumption generalizes the Copernican idea by requiring that no location or direction in the Universe is distinguished. However, on small scales, e.g. as solar systems, galaxies, or even galaxy clusters, the distribution of matter is clearly inhomogeneous. Indeed, statistical analyses indicate that only beyond tens to hundreds of Mpc* does the Universe begin to approach homogeneity. Moreover, compelling evidence demonstrates that the Universe is expanding. This implies that, in its early history, the distances between observers and distant galaxies were smaller than they are at present. The combination of large-scale uniformity and cosmic expansion underpins the description of the Universe using the Friedmann-Lemaître-Robertson-Walker metric and the Friedmann equations, which constitute the foundation of modern background cosmology.

In this chapter, we examine the background Universe. We begin by discussing the geometry and expansion of a homogeneous and isotropic spacetime, together with its dynamical properties. We then provide an overview of the current standard cosmological model. Finally, we turn to the study of cosmological distances, which play a central role in observational cosmology. This chapter establishes the theoretical foundation for the subsequent ones, where we will address perturbations on top of the background. We follow [4, 5, 22], which will remain central references for the discussions to come.

*Distances in cosmology are typically measured in megaparsecs (Mpc), where 1Mpc $\approx 3 \times 10^{19}\, km$.

2.1 Friedmann-Lemaître-Robertson-Walker Universe

The cosmological principle together with the observed expansion of the Universe leads to the Friedmann-Lemaître-Robertson-Walker (FLRW) metric, which in terms of *conformal time* η[*] can be written as[†]

$$ds^2 = a^2(\eta)\left(-d\eta^2 + \gamma_{ij}\, dr^i dr^j\right), \tag{2.1}$$

where $a(\eta)$ is the *scale factor* and γ_{ij} denotes the metric of a maximally symmetric three-space of constant curvature K.

The spatial metric γ_{ij} encodes the geometry of the Universe, which admits three distinct possibilities corresponding to constant spatial curvature: *flat* ($K = 0$), *open* ($K < 0$), or *closed* ($K > 0$) universes (see Fig. 2.1). These cases can be intuitively understood by considering two freely moving particles that begin their trajectories parallel to one another. In a flat universe, the particles behave exactly as in Euclidean geometry: their trajectories remain parallel indefinitely. This corresponds to three-dimensional Euclidean space, where parallel lines never intersect, and the FLRW metric reduces to

$$ds^2 = a^2(\eta)\left(-d\eta^2 + \delta_{ij}\, dr^i dr^j\right). \tag{2.2}$$

If the Universe is closed ($K > 0$), also referred to as *spherical space*, initially parallel geodesics gradually converge, analogously to lines of longitude on a two–sphere meeting at the poles. Conversely, in an open universe ($K < 0$), also known as *hyperbolic space*, initially parallel trajectories diverge, much like marbles rolling apart on a saddle–shaped surface. In what follows, we shall restrict our analysis to the case of a flat universe, since this geometry is most consistent with current cosmological observations and provides the simplest theoretical framework.

On the other hand, the scale factor encapsulates the temporal evolution of the Universe's expansion. By convention, it is normalized such that $0 < a(\eta) < a_0 = 1$, i.e. the scale factor vanishes at the initial singularity and increases monotonically, attaining unity at the present epoch.To quantify the rate of expansion we define the *Hubble parameter*

$$H \equiv \frac{da}{dt}\frac{1}{a} = \frac{1}{a^2}\frac{da}{d\eta}. \tag{2.3}$$

[*]The conformal time η is defined by $d\eta = dt/a(t)$, with t the cosmic time and $a(t)$ the scale factor.
[†]Throughout this work we employ natural units, identifying the speed of light with unity, $c \equiv 1$.

Its present value is called the *Hubble constant* [21],

$$H_0 \approx 100\,h\,\mathrm{km\,s^{-1}\,Mpc^{-1}}, \tag{2.4}$$

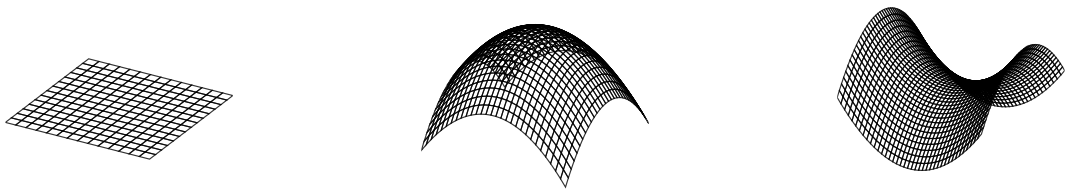
where h is a dimensionless parameter of order unity, with the latest measurements giving $h \approx 0.674$ [21]. It is also customary to introduce the *conformal Hubble parameter*

$$\mathcal{H}(\eta) \equiv aH = \frac{1}{a}\frac{da}{d\eta}. \tag{2.5}$$

It is crucial to stress that the notion of cosmic expansion does not imply that galaxies are moving through a static background space. Rather, it is spacetime itself that undergoes expansion: the separations between objects not bound by local interactions, e.g distant galaxies, increase with cosmic time. To illustrate this concept, one may consider a spatial grid, as depicted in Fig. (2.2), which expands homogeneously as time progresses. The points of this grid, representing *comoving* observers, retain fixed coordinate positions, r_0 and r_1, such that the *comoving distance*, $r = |r_1 - r_0|$, between any two points, defined simply as the difference in their coordinates and computable by counting grid cells as indicated in Fig. (2.2), remains invariant. By contrast, the *physical distance*, x, between these points is proportional to the scale factor, and thus evolves with time. This relationship can be formally expressed as

$$x = a(\eta)\,r. \tag{2.6}$$

Another closely related phenomenon is the stretching of the physical wavelength of photons emitted by distant sources, which increases in direct proportion to the cosmic scale factor. Consequently, the wavelength measured by an observer at the present epoch is larger than the wavelength at emission $\lambda \to a(\eta)\lambda$. This effect is conveniently parametrized by the redshift z, defined as



flat spherical hyperbolic

FIGURE 2.1: The Universe can be foliated into spatial hypersurfaces of constant curvature: flat ($K = 0$), spherical ($K > 0$), or hyperbolic ($K < 0$) [5].

$$1 + z \equiv \frac{\lambda_{\text{obs}}}{\lambda_{\text{emit}}} = \frac{a_{\text{obs}}}{a_{\text{emit}}} = \frac{a_{\text{today}}}{a_{\text{emit}}} = \frac{1}{a_{\text{emit}}}. \tag{2.7}$$

This relation reflects what we actually observe from distant galaxies: the light carried by photons, whose wavelength is stretched by the expansion of the Universe. It shows that the measured redshift z provides a direct measure of the scale factor at the time of emission, linking theoretical cosmic expansion to observable quantities.

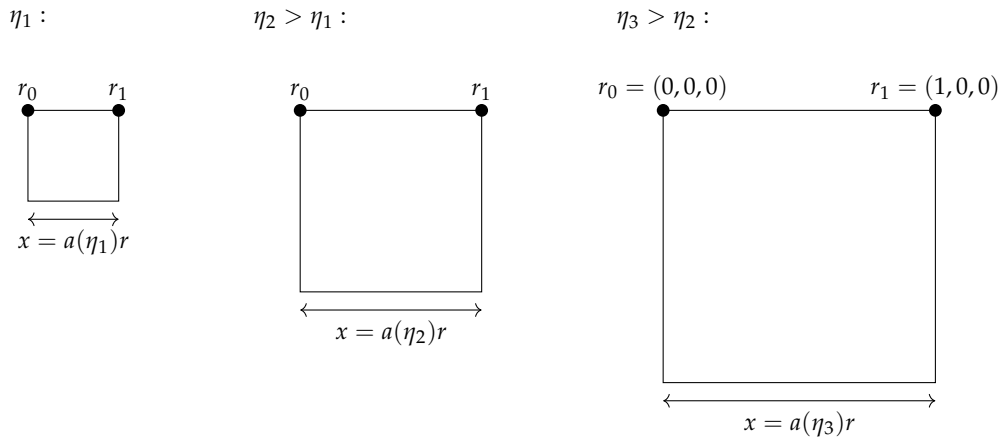


FIGURE 2.2: Expansion of the Universe illustrated by a comoving coordinate grid. The comoving separation between two points, r_0 and r_1, remains constant throughout cosmic evolution, while the corresponding physical distance grows proportionally to the scale factor [4].

2.2 Friedmann Equations and the Standard Model of Cosmology

When we apply the FLRW metric to Einstein's field equations,

$$G_{\mu\nu} + \Lambda g_{\mu\nu} = 8\pi G T_{\mu\nu}, \tag{2.8}$$

where $G_{\mu\nu}$ is the Einstein tensor, $g_{\mu\nu}$ the metric tensor, $T_{\mu\nu}$ the stress–energy tensor, Λ the cosmological constant, and G the Einstein gravitational constant, we obtain the *Friedmann equations*. For a flat universe, in terms of conformal time, they read

$$\mathcal{H}^2 \equiv \left(\frac{\dot{a}}{a}\right)^2 = \frac{8\pi G}{3}\,\rho\, a^2, \tag{2.9}$$

$$\frac{\ddot{a}}{a} = -\frac{4\pi G}{3}\,(\rho + 3p)\, a^2. \tag{2.10}$$

Here ρ denotes the *matter-energy density* and p the *pressure*. These equations govern the expansion rate of the Universe and describe its evolution depending on its matter and energy content.

The *critical density* today is defined as the energy density of a spatially flat universe today, i.e.,

$$\rho_{\text{crit},0} \equiv \frac{3H_0^2}{8\pi G}. \tag{2.11}$$

It is often convenient to express all densities relative to the critical density by defining the dimensionless density parameters

$$\Omega_{i,0} \equiv \frac{\rho_{i,0}}{\rho_{\text{crit},0}}, \qquad i = r, m, \Lambda, \dots \tag{2.12}$$

where r, m, and Λ denote radiation, matter, and dark energy (cosmological constant), respectively. In terms of these density parameters, the first Friedmann equation can be written as

$$H^2(a) = H_0^2 \left(\Omega_{r,0} a^{-4} + \Omega_{m,0} a^{-3} + \Omega_{\Lambda,0} \right). \tag{2.13}$$

Evaluating both sides of the Friedmann equation at the present time ($a_0 = 1$) leads to the density parameters to the closure relation

$$\Omega_{r,0} + \Omega_{m,0} + \Omega_{\Lambda,0} = 1. \tag{2.14}$$

Current cosmological observations are in strong agreement with the so-called standard cosmological model, known as ΛCDM. This framework describes a spatially flat universe dominated by the cosmological constant Λ and cold dark matter (CDM), while also containing a baryonic component, i.e. "ordinary" matter composed of protons, neutrons, and electrons — that is, atoms. The density parameters inferred from current measurements are given by [21]

$$\Omega_{r,0} \simeq 0, \tag{2.15}$$

$$\Omega_{m,0} \simeq 0.315, \tag{2.16}$$

$$\Omega_{\Lambda,0} \simeq 0.685, \tag{2.17}$$

which are consistent with the closure relation above. The matter density parameter $\Omega_{m,0}$ can be further decomposed into baryonic matter and cold dark matter as

$$\Omega_{b,0}h^2 \simeq 0.022, \tag{2.18}$$

$$\Omega_{c,0}h^2 \simeq 0.120, \tag{2.19}$$

respectively.

2.3 Cosmological Distances

A final concept of central importance in cosmology concerns the definition of distance measures. Observational cosmology requires a careful distinction between several notions of distance, as these are not equivalent in an expanding universe. In the smooth background spacetime described by the FLRW metric, physical distances are related to comoving coordinates through the scale factor.

The natural starting point is the comoving distance, which is defined on the comoving grid (as seen in Fig. (2.2)). During an infinitesimal conformal time interval $d\eta$, light travels a comoving distance

$$dr = d\eta. \tag{2.20}$$

Hence, it follows from the FLRW metric (Eq. 2.1) that the comoving distance traversed by a photon emitted at conformal time η and observed today at η_0 is

$$r(\eta) = \int_{\eta}^{\eta_0} d\eta = \int_0^z \frac{dz'}{(1+z')\mathcal{H}(z')}. \tag{2.21}$$

This quantity provides the baseline notion of distance in cosmology. From it, we can construct observable distance measures that relate comoving separations to quantities actually measured, such as angles or fluxes.

A classical method for distance determination is based on *standard rulers*. An object of physical size $l_{\text{physical}} = a\, l_{\text{comoving}}$ subtending an angle θ defines the *angular diameter distance* as

$$d_A = \frac{l_{\text{physical}}}{\theta}. \tag{2.22}$$

In comoving coordinates, the observed angle is

$$\theta \approx \frac{l_{\text{comoving}}}{r(\eta)} = \frac{l_{\text{physical}}}{a\, r(\eta)}, \tag{2.23}$$

yielding

$$d_A = a\, r(\eta) = \frac{r(\eta)}{1+z}. \tag{2.24}$$

A complementary method relies on the observed flux of objects of known luminosity, leading to the definition of the *luminosity distance*. In an expanding universe, the flux from a source is affected by the cosmological redshift in two ways. First, the energy of each photon is reduced by a factor of a. Second, the photon arrival rate is dilated by another factor of a. Consequently, the total observed flux is suppressed by a^2 relative to the intrinsic luminosity. For a source at comoving distance $r(\eta)$, the observed flux is therefore

$$F = \frac{La^2}{4\pi r^2(\eta)}, \tag{2.25}$$

where L denotes the source luminosity at emission. This motivates the definition of the luminosity distance,

$$d_L \equiv \frac{r(\eta)}{a} = (1+z)r(\eta). \tag{2.26}$$

These two notions of distance are not independent. In fact, they are connected through the exact reciprocity relation, valid in any FLRW universe, which states that

$$d_L = (1+z)^2 d_A. \tag{2.27}$$

Chapter 3

Effect of Peculiar Velocities in Large-Scale Matter Distribution

Observations of the universe do not provide a direct picture of the underlying matter distribution. Instead, they are affected by various perturbations arising from different physical processes. Among the most relevant are the peculiar velocities of galaxies, which induce apparent anisotropies in the observed large-scale structure through their effect on measured redshifts. A key consequence of these motions is the Doppler effect, which alters the observed redshift of galaxies and encodes information about their velocities.

In this chapter, we introduce the formalism of the density contrast to describe the large-scale structure of the Universe. We then discuss how peculiar velocities distort observations, beginning with the non-relativistic Doppler contribution, for which our treatment follows [4], and extending to the relativistic case. The full relativistic derivation lies beyond the scope of this work; instead, we only summarize the main ingredients and refer the reader to [8] for a comprehensive presentation. Since these two references will be used extensively throughout, we cite them here at the outset.

3.1 Tracers of Large-Scale Matter Distribution

Before we begin our discussion of the effects of peculiar velocities, it is essential to understand what we call *large-scale matter distribution* and how we can measure it.

The cosmological principle is only valid when considering the spatial *average*, $\langle\cdot\rangle$. Consequently, when describing the properties of the universe as a whole, it is necessary to

focus on averaged quantities. For instance, when discussing the matter-energy density of the universe, we consider

$$\bar{\rho}(\eta) = \langle \rho(\boldsymbol{r}, \eta) \rangle, \tag{3.1}$$

where $\bar{\rho}(\eta)$ denotes the average value of ρ over a sufficiently large cosmological volume, representative of the universe as a whole. Similarly, for the *number of galaxies* of type g, n_g, we define

$$\bar{n}_g(\eta) = \langle n_g(\boldsymbol{r}, \eta) \rangle, \tag{3.2}$$

For simplicity, we will omit the time dependence, η, assuming it to be fixed.

This assumption implies that, locally, the density exhibits fluctuations around its average value. To characterize these deviations, we introduce the *density contrast*, defined as [4]

$$\delta(\boldsymbol{r}) \equiv \frac{\rho(\boldsymbol{r}) - \bar{\rho}}{\bar{\rho}}, \tag{3.3}$$

which, in the context of this work, represents the matter density contrast.The density contrast for the galaxy number density is then defined as

$$\delta_g(\boldsymbol{r}) \equiv \frac{n_g(\boldsymbol{r}) - \bar{n}_g}{\bar{n}_g}. \tag{3.4}$$

These fluctuations are not random but exhibit a structured organization that arises from variations in the initial energy density, commonly referred to as *initial density fluctuations*. The study of these initial density fluctuations is a central topic in modern physics, as their influence predates the cosmic microwave background (CMB) [4, 22].

The number of galaxies also varies locally, giving rise to the observed spatial distribution known as galaxy clustering. This large-scale structure is primarily driven by gravity: initial density fluctuations caused regions with slightly higher densities to attract more matter, eventually leading to the formation of galaxies. A key role in this process is played by dark matter halos, which formed from the initial density fluctuations and created regions of strong gravitational potential. Baryonic matter subsequently fell into these halos, giving rise to the formation of galaxies that trace the underlying dark matter distribution and reinforce the observed clustering [4, 22].

From this, it is reasonable "fair" to infer a relationship between fluctuations in the number of galaxies and the matter density as

$$\delta_g(\boldsymbol{r}) \propto \delta(\boldsymbol{r}), \tag{3.5}$$

Thus, galaxies serve as *tracers* of the large-scale matter density field. It is important to note that while this proportionality holds intrinsically, the observed galaxy distribution is affected by peculiar velocities, which will be the focus of the subsequent sections.

3.2 "Newtonian" Distortion of the Observed Density Field of Number of Galaxies

In cosmological observations, we infer the positions of distant galaxies primarily through their redshifts. However, the redshift of an object encodes not only the cosmological expansion but also contributions from its peculiar velocity along the line of sight. This leads to systematic deviations between the true spatial distribution of matter and the one reconstructed from redshift measurements, thereby also impacting how galaxies appear to us in observations.

To formalize this, we begin by establishing the relationship between the true position of a galaxy and its observed redshift-space position, highlighting how peculiar velocities project into redshift measurements. We then apply this framework to the observed number of galaxies, which becomes distorted in redshift space due to these velocity effects. For the time being, we shall disregard relativistic effects and adopt a more "Newtonian" derivation.

3.2.1 Perturbations on Observed Position

A given galaxy at a comoving distance from us will have a three-dimensional position vector $\boldsymbol{r}$ with components

$$\boldsymbol{r}_{\text{obs}}(z,\theta,\phi) = r(z)\hat{\boldsymbol{n}}(\theta,\phi); \quad \hat{\boldsymbol{n}} = \frac{\boldsymbol{r}_{\text{obs}}}{|\boldsymbol{r}_{\text{obs}}|}. \tag{3.6}$$

The unit vector $\hat{\boldsymbol{n}}$ is in one-to-one correspondence with the galaxy's position on the sky, which in turn is specified by the two angles θ, ϕ. However, Eq. (3.6) does not account for the fact that galaxies have peculiar motions with respect to the background. Because of

this, $|\boldsymbol{r}_{\rm obs}|$ does not exactly correspond to the true distance of the galaxy: the observed redshift is shifted relative to the background value according to

$$1 + z_{\rm obs} = \frac{1}{a}\left[1 + u_{\parallel}\right], \tag{3.7}$$

where $u_{\parallel} = \boldsymbol{u}_g \cdot \hat{\boldsymbol{n}}$ and a is the scale factor at emission time. The factor $1/a$ is the true cosmological redshift (Eq. (2.7)) while the second term is the *Doppler shift* due to the peculiar velocity $\boldsymbol{u}_g$ of the galaxy, at linear order in $\boldsymbol{u}_g$[*]. Notice that $1/a$ is present on the Doppler shift which means that the fractional effect of a given peculiar velocity on the redshift is independent of how far away the galaxy is. In the following, we assume that the galaxy velocity coincides with that of the underlying matter, $\boldsymbol{u}_g = \boldsymbol{u}_m$, as there is currently no evidence for a velocity bias[†] [23]. There are other contributions to the redshift which were neglected in Eq. (3.7).

We can expand $r(z)$ around z, from Eq. (2.21) Eq. (3.6) and Eq. (3.7) we have

$$\boldsymbol{r}_{\rm obs}(z,\theta,\phi) \approx \boldsymbol{r} + \Delta\boldsymbol{r} = \boldsymbol{r} + \mathcal{H}^{-1} u_{\parallel}\hat{\boldsymbol{n}}(\theta,\phi), \tag{3.8}$$

where $\boldsymbol{r}$ is the true position. Because the observed position of each galaxy is shifted along its line of sight, $\Delta\boldsymbol{r}_{\rm obs}$ is proportional to $\hat{\boldsymbol{n}}$, i.e., the observed (angular) position on the sky is unchanged. An illustrative example is shown in Fig. (3.1).

3.2.2 Perturbations on Observed Number of Galaxies

Regardless of whether we are using the observed or true position, the number of galaxies must be the same within the same volume. If we divide this volume into infinitesimal volumes and count the galaxies within each position, the result will be the same, so

$$n_{g,\rm obs}(\boldsymbol{r}_{\rm obs})d^3\boldsymbol{r}_{\rm obs} = n_g(\boldsymbol{r})d^3\boldsymbol{r}, \tag{3.9}$$

where the infinitesimal volume element around a point in observed coordinates is

$$d^3\boldsymbol{r}_{\rm obs} = r_{\rm obs}^2 dr_{\rm obs} d\Omega, \tag{3.10}$$

[*]We have assumed that the velocities of galaxies are much smaller than the speed of light, allowing us to stop at linear order in $\boldsymbol{u}_g$.

[†]While galaxies typically follow the large-scale matter velocity field, their peculiar velocities *distribution* may differ from those of the underlying matter [23].

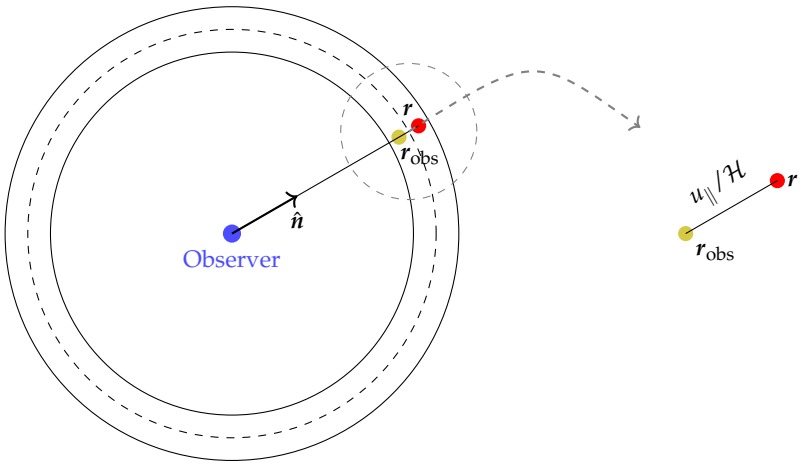


FIGURE 3.1: Schematic representation of the challenges involved in measuring the three-dimensional galaxy density field. Galaxies are selected within a narrow redshift interval (solid arcs) centered at the mean redshift $\bar{z}$ (dotted arc). A galaxy is observed at an angular position $\hat{\boldsymbol{n}}$ on the sky with measured redshift z. It is then assigned the apparent comoving position $\boldsymbol{r}_{\rm obs}$, which differs from its true position $\boldsymbol{r}$ because the distance–redshift relation is perturbed by the Doppler effect arising from the galaxy's line-of-sight velocity component, $u_\parallel$ [4].

with $\mathrm{r}_{\rm obs} \equiv |\boldsymbol{r}_{\rm obs}|$, while the volume around a point in proper space is

$$d^3\boldsymbol{r} = r^2 dr d\Omega, \tag{3.11}$$

with $\mathrm{r} \equiv |\boldsymbol{r}|$. The angular volume elements $d\Omega$ are identical, so

$$n_{g,\rm obs}(\boldsymbol{r}_{\rm obs}) = n_g(\boldsymbol{r}) J, \tag{3.12}$$

where the Jacobian J encondes the mapping between real and observed coordinates and, to first order of perturbation, is given by [7]

$$J \equiv \left| \frac{d^3\boldsymbol{r}}{d^3\boldsymbol{r}_{\rm obs}} \right| \approx 1 - \frac{2}{\mathcal{H}r} u_\parallel - \mathcal{H}^{-1}\partial_r u_\parallel. \tag{3.13}$$

From Eq. (3.4), the number densities in true and observed coordinates are $n_g(\boldsymbol{r}) = \bar{n}_g(\boldsymbol{r})\left(1+\delta_g(\boldsymbol{r})\right)$ and $n_{g,\rm obs}(\boldsymbol{r}_{\rm obs}) = \bar{n}_g(\boldsymbol{r}_{\rm obs})\left(1+\delta_{g,\rm obs}(\boldsymbol{r}_{\rm obs})\right)$, respectively. Then Eq. (3.9) can be rewritten as

$$\delta_{g,\rm obs}(\boldsymbol{r}_{\rm obs}) \approx b_g \delta_m(\boldsymbol{r}) - \mathcal{H}^{-1}\partial_r u_\parallel - u_\parallel \alpha_{\rm newt}, \tag{3.14}$$

where we have assumed a *linear bias relation* [6]

$$\delta_g(\boldsymbol{r}) = b_g \delta_m(\boldsymbol{r}) \tag{3.15}$$

and $\alpha_{\text{newt},g}$, which shall be referred to as the *Newtonian Doppler term* and is dimensionless, is given by [7]

$$\alpha_{\text{newt},g} \equiv \frac{\mathcal{H}^{-1}}{r} \frac{\mathrm{d}\ln\left(\boldsymbol{r}^2 \bar{n}_g(\boldsymbol{r})\right)}{\mathrm{d}\ln(\boldsymbol{r})}. \tag{3.16}$$

It is notable that both the bias parameter b_g and $\alpha_{\text{newt},g}$ are sensitive to the galaxy sample considered and are generally redshift-dependent.

We now introduce the distant-observer approximation, which is essentially a flat-sky approximation. The idea is that we can treat the direction vector, $\hat{\boldsymbol{n}}$, as fixed, neglecting variations from galaxy to galaxy. This is justified if the angular scales involved are small. That is, as long as the galaxies are relatively close to each other in the $\left(r^1, r^2\right)$ plane, we can approximate $\hat{\boldsymbol{n}} \cdot \boldsymbol{u}_m \to \hat{\boldsymbol{e}}_z \cdot \boldsymbol{u}_m$, where $\hat{\boldsymbol{e}}_z$ is chosen to be a constant unit vector along the z-axis, corresponding to the fixed line-of-sight direction toward the center of the sky area covered by the survey of interest.

In the distant-observer approximation, we can directly compute the Fourier transform of the overdensity [7]

$$\begin{aligned}\delta_{g,\text{obs}}(\boldsymbol{k}) &= \int d^3\mathrm{r}_{\text{obs}} \delta_{g,\text{obs}}(\boldsymbol{r}_{\text{obs}}) e^{-i\boldsymbol{k}\cdot\boldsymbol{r}_{\text{obs}}} \\ &\approx \left(b_g + f\mu^2 - \frac{1}{k}\alpha_{\text{newt}} i f\mathcal{H}\mu\right)\delta_m(\boldsymbol{k})\end{aligned} \tag{3.17}$$

where we used

$$\boldsymbol{u}(\boldsymbol{k}) = i f\mathcal{H}\frac{\hat{\boldsymbol{k}}}{k}\delta_m(\boldsymbol{k}), \tag{3.18}$$

$\mu = \hat{\boldsymbol{k}} \cdot \hat{\boldsymbol{n}}$ and f is the linear growth rate, $f \equiv d\ln(D_+)/d\ln(a)$.

If we take $\bar{z} = 0.133$, $\mu = 1$, select bright galaxies, and consider the absolute value, we find that for $k = 0.2\, Mpc^{-1}$ (small distances),

$$b_g + f\mu^2 \approx 1.894 \gg \alpha_{\text{newt}} f\mathcal{H}\mu/k \approx 0.001,$$

meaning that the imaginary part is roughly 10^{-3} smaller than the real part. Therefore, for surveys probing small distances or very large k, the α_{newt} term becomes negligible compared to the others, and thus

$$\delta_{g,\text{obs}}(\boldsymbol{k}) \approx \left(b_g + f\mu^2\right)\delta_m(\boldsymbol{k}), \tag{3.19}$$

which corresponds to the well-known linear redshift-space distortion (RSD), first derived by Kaiser in 1986 and extensively studied since then, and is therefore not the focus of modern investigations [7].

If we increase the survey distance (decreasing k) down to $0.008\,\mathrm{Mpc}^{-1}$, we obtain

$$\alpha_{\mathrm{newt}} f\mathcal{H}\mu/k \approx 0.035,$$

which reduces the ratio between the real and imaginary parts, making the Doppler effect more significant and enabling its detection which is our main goal. This behavior is further illustrated in Fig. 3.2, where the ratio is seen to decrease substantially, showing an inverse dependence on both k.

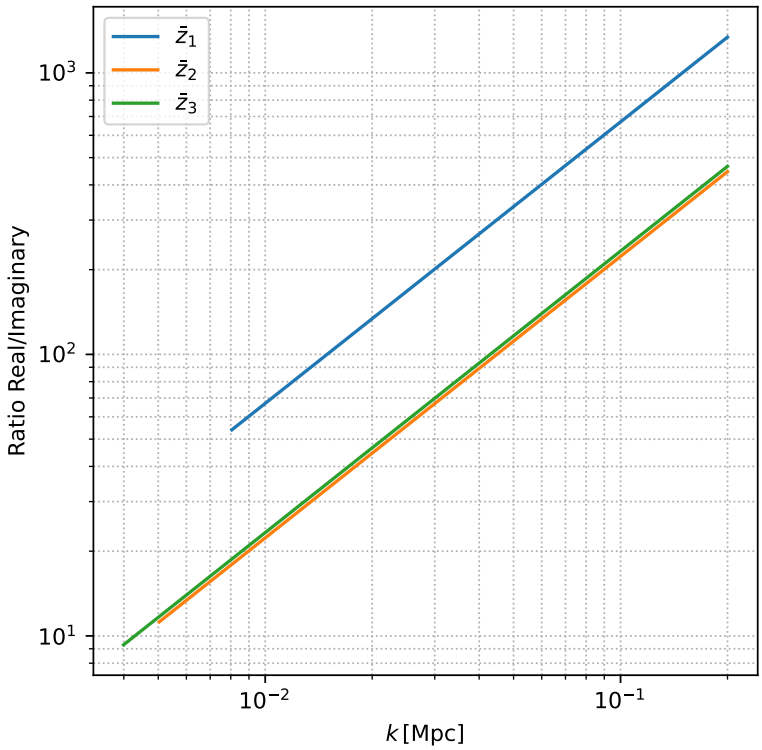


FIGURE 3.2: Ratio of $\left(b_g + f\mu^2\right) / \left(\alpha_g f\mathcal{H}\mu/k\right)$ for the different $\bar{z} = (0.133, 0.3, 0.45)$, for the bright subsample (see Section 5.1). Relativistic effects are included in the calculation (which will be introduced in the next Section).

3.3 Relativistic Doppler Effect

Up to this point, we have neglected relativistic corrections. However, in order to properly account for the relativistic Doppler effect, such corrections must be incorporated.

The starting point is to obtain the relativistic counterpart of Eq. (3.12). In the Newtonian case, only perturbations in position are considered; however, in a general relativistic framework the situation is considerably more involved. Peculiar velocities induce perturbations not only in the redshift but also in the observed volume [10]. To properly account for these effects, we introduce a perturbed metric built upon the flat ($K = 0$) background metric (Eq. (2.1)), restricted to linear order with scalar perturbations. For convenience, we adopt the conformal Newtonian gauge, in which the metric takes the form

$$ds^2 = a^2(\eta)\left[-(1+2\psi)d\eta^2 + (1-2\phi)\delta_{ij}dr^i dr^j\right], \tag{3.20}$$

where ψ and ϕ denote the Bardeen potentials. We assume throughout that the underlying theory of gravity is GR, which satisfies the Euler equation [10]

$$\dot{\boldsymbol{u}} + \mathcal{H}\boldsymbol{u} + \nabla\psi = 0. \tag{3.21}$$

Finally, it should be emphasized that the observable quantity provided by galaxy surveys is typically the flux (Eq. (2.25)) of the energy emitted by galaxies, F [15]*. Consequently, perturbations in the source luminosity, L, must also be taken into account. The full expression is [8]

$$\begin{aligned}
\delta_{g,\mathrm{obs}}(z,\hat{\boldsymbol{n}}) = {} & \delta_g - \frac{1}{\mathcal{H}}\partial_r \boldsymbol{u}\cdot\hat{\boldsymbol{n}} + (5s-2)\left[\kappa - \frac{1}{r}\int^{\eta_A}(\phi+\psi)\mathrm{d}\eta\right] \\
& + \left[\frac{2-5s}{\mathcal{H}r} + 5s - b_e + \frac{\dot{\mathcal{H}}}{\mathcal{H}^2}\right]\left[\psi + \int^{\eta_A}(\dot{\phi}+\dot{\psi})\mathrm{d}\eta - \boldsymbol{u}\cdot\hat{\boldsymbol{n}}\right] \\
& + \frac{1}{\mathcal{H}}\dot{\phi} + \psi + (5s-2)\phi = \\
= {} & \delta_g - \frac{1}{\mathcal{H}}\partial_r \boldsymbol{u}\cdot\hat{\boldsymbol{n}} - \left[\frac{2-5s}{\mathcal{H}r} + 5s - b_e + \frac{\dot{\mathcal{H}}}{\mathcal{H}^2}\right]\boldsymbol{u}\cdot\hat{\boldsymbol{n}} \\
& + (5s-2)\kappa \\
& - (5s-2)\frac{1}{r}\int^{\eta_A}(\phi+\psi)\mathrm{d}\eta \\
& + \left[\frac{2-5s}{\mathcal{H}r} + 5s - b_e + \frac{\dot{\mathcal{H}}}{\mathcal{H}^2}\right]\left[\psi + \int^{\eta_A}(\dot{\phi}+\dot{\psi})\mathrm{d}\eta\right] \\
& + \frac{1}{\mathcal{H}}\dot{\phi} + \psi + (5s-2)\phi.
\end{aligned} \tag{3.22}$$

*Surveys may also report apparent magnitudes, m [15]; however, this distinction is not relevant for the present derivation and will therefore be omitted here. A more detailed discussion is given in Section 5.1.

The parameter s is defined as

$$s\left(z, L > L_c\right) \equiv -\frac{2}{5}\frac{\partial \ln \bar{n}_g\left(z, L > L_c\right)}{\partial \ln(1+z)}, \tag{3.23}$$

and is commonly referred to as the magnification bias. Similarly, the parameter b_e is defined as

$$b_e\left(z, L > L_c\right) \equiv \frac{\partial \ln \bar{n}_g\left(z, L > L_c\right)}{\partial L_c}, \tag{3.24}$$

and is known as the evolution bias. Here, $\bar{n}_g\left(z, L > L_c\right)$ denotes the comoving number density of galaxies with luminosity above the critical threshold L_c, which typically corresponds to the detector sensitivity limit. In addition, we introduce the parameter κ, the convergence, given by

$$\kappa \equiv -\frac{1}{2}\nabla^2_{\hat{\boldsymbol{n}}}\int_{\eta_A}^{\eta} d\eta' \frac{(\eta' - \eta)}{(\eta_A - \eta)(\eta_A - \eta')}(\phi + \psi), \tag{3.25}$$

where $\nabla^2_{\hat{\boldsymbol{n}}}$ is the Laplacian on the unit sphere.

All the terms in Eq. (3.22) correspond to perturbations relating the matter density contrast to the observed number of galaxies. Although we will not work out each of them in detail, we briefly identify all contributions for completeness. The first contribution is the perturbation to the galaxy number density, δ_g, a Newtonian-gauge quantity. As in Eq. (3.15), we assume a linear bias [10], $\delta_g = b_g\delta_m$. The second contribution is the redshift–space distortion, δ_{RDS}, which is identical to the Newtonian derivation of Eq. (3.17). The third contribution is the relativistic Doppler contribution δ_α,

$$\delta_\alpha = \alpha_g \boldsymbol{u}\cdot\hat{\boldsymbol{n}}, \tag{3.26}$$

where the amplitude, α_g, is given by[9, 10, 13, 15, 16]

$$\alpha_g = \frac{\dot{\mathcal{H}}}{\mathcal{H}^2} + 5s + \frac{2-5s}{r\mathcal{H}} - b_e. \tag{3.27}$$

The fourth contribution, known as the convergence or lensing term, $\delta_{\mathrm{lensing}}$, accounts for the distortions produced by gravitational lensing on the observed solid angle. The remaining contributions arise from potential terms: the perturbation to the spatial metric (ψ) in converting dz to a proper time interval at the source, the ISW–like effect from $\dot{\phi}$ across the source volume, and the contribution of the spatial metric at the source (2ϕ) to the transverse distances.

In our final expression, in the low-redshift approximation, the Doppler contribution becomes dominant, while other contributions are negligible [15, 24]. Accordingly, Eq. (3.22) can be approximated in Fourier space as

$$\begin{aligned}\delta_{g,\mathrm{obs}}(\boldsymbol{k}) &\approx \delta_g + \delta_{\mathrm{RDS}} + \delta_\alpha \\ &= b_g\delta_m + f\mu^2 - \frac{if\mathcal{H}\mu}{k}\alpha_g,\end{aligned} \tag{3.28}$$

which coincides with Eq. (3.17), except that we now employ the relativistic definition of α_g.

Chapter 4

The Impact of Doppler Effect in the Galaxy Power Spectrum

In the previous chapter, we derived the correlation between the density contrast of the observed galaxy number and that of the "true" matter distribution, as expressed in Eq. (3.17). Furthermore, we also obtained the expression for the relativistic Doppler amplitude, given by Eq. (3.27). However, in a statistical analysis, the lowest-order non-vanishing correlation is the two-point correlation function, which in Fourier space corresponds to the *power spectrum* [*].

In this chapter, we aim to compute the power spectrum using Eq. (3.17), incorporating the relativistic amplitude. We will then explore how the Doppler amplitude can be isolated. In the end, we introduce the final methodological component required for a realistic analysis: the discretization of the galaxy power spectrum; and its estimators [4].

4.1 Matter Power Spectrum

The density contrast, on average, satisfies the property $\langle \delta \rangle = 0$. Therefore, the first non-trivial statistical measure is its covariance, represented by the two-point correlation function [5]

$$\xi\left(\left|\boldsymbol{r}-\boldsymbol{r}'\right|\right) \equiv \left\langle \delta(\boldsymbol{r})\delta\left(\boldsymbol{r}'\right)\right\rangle . \tag{4.1}$$

[*]Although its importance goes beyond being merely the lowest-order non-zero statistic, we do not discuss these aspects further in this thesis.

Given that the Fourier modes of small fluctuations evolve independently, it is often convenient to express the two-point function in Fourier space [5]

$$\left\langle \delta(\boldsymbol{k})\delta^{*}\left(\boldsymbol{k}'\right)\right\rangle \equiv (2\pi)^{3}\delta_{\mathrm{D}}\left(\boldsymbol{k}-\boldsymbol{k}'\right)\mathcal{P}_{m}(k), \tag{4.2}$$

where

$$\delta(\boldsymbol{k}) = \int d\boldsymbol{r}\, e^{-i\boldsymbol{k}\cdot\boldsymbol{r}}\,\delta(\boldsymbol{r}) \tag{4.3}$$

and the proportionality to the Dirac delta function $\delta_{\mathrm{D}}(\boldsymbol{k}-\boldsymbol{k}')$ reflects the translational invariance of the universe's homogeneity. This implies that Fourier modes with different wavevectors are independent. The function $\mathcal{P}_m(k)$, referred to as the *matter power spectrum*, is the three-dimensional Fourier transform of the correlation function $\xi(r)$ (see Fig. 4.1 for a visual representation). Due to rotational invariance, the power spectrum depends only on the magnitude of the wavevector, $k = |\boldsymbol{k}|$.

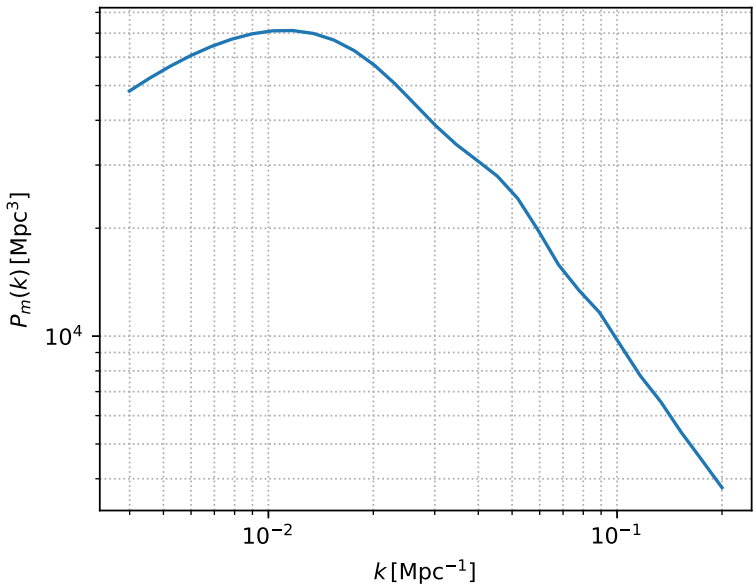


FIGURE 4.1: Matter power spectrum, $P_m(k)$, evaluated at redshift $z = 0.467$

It is important to emphasize that these fields in Fourier space satisfy a reality condition, a direct consequence of the fact that the original field $\delta(\boldsymbol{r})$ is real-valued in configuration space. Specifically, the Fourier transform of a real field obeys the symmetry,

$$\delta(-\boldsymbol{k}) = \delta^{*}(\boldsymbol{k}), \tag{4.4}$$

where the asterisk denotes complex conjugation. This condition implies that the Fourier coefficients are not independent across all modes: the amplitude and phase of the mode at wavevector $\boldsymbol{k}$ determine those at $-\boldsymbol{k}$. As a result, only half of Fourier space contains indepedent information.

4.2 Galaxy Power Spectrum

Analogously to the matter power spectrum, we can define a power spectrum for the galaxy density contrast as

$$\left\langle \delta_g(\boldsymbol{k})\delta_g^*\left(\boldsymbol{k}'\right)\right\rangle \equiv (2\pi)^3\delta_{\mathrm{D}}\left(\boldsymbol{k}-\boldsymbol{k}'\right)\mathcal{P}_g(k,\mu). \tag{4.5}$$

where $\mathcal{P}_g(k,\mu)$ denotes the *auto* power spectrum of the galaxy population g. While Eq. (4.5) assumes a single galaxy type, this formalism can be naturally generalized to describe correlations between two (possibly distinct) galaxy populations, g and g', yielding

$$\left\langle \delta_g(\boldsymbol{k})\delta_{g'}^*\left(\boldsymbol{k}'\right)\right\rangle \equiv (2\pi)^3\delta_{\mathrm{D}}\left(\boldsymbol{k}-\boldsymbol{k}'\right)\mathcal{P}_{gg'}(k,\mu). \tag{4.6}$$

where $\mathcal{P}_{gg'}(k,\mu)$ denotes the *cross* power spectrum between galaxy populations g and g'.

Applying Eq. (3.17), we get [16]

$$\begin{aligned}\mathcal{P}_{gg'}(k,\mu) = \Bigg[&\left(b_g+f\mu^2\right)\left(b_{g'}+f\mu^2\right)+\frac{\mathcal{H}^2}{k^2}\alpha_g\alpha_{g'}f^2\mu^2 \\ &-\mathrm{i}\frac{\mathcal{H}}{k}\left[\alpha_g\left(b_{g'}+f\mu^2\right)-\alpha_{g'}\left(b_g+f\mu^2\right)\right]f\mu\Bigg]\mathcal{P}_m.\end{aligned} \tag{4.7}$$

In the auto power spectrum case [12],

$$\mathcal{P}_g(k,\mu) = \left[\left(b_g+f\mu^2\right)^2+\frac{\mathcal{H}^2}{k^2}\alpha_g^2f^2\mu^2\right]\mathcal{P}_m. \tag{4.8}$$

We observe that when considering only a single galaxy population, the Doppler amplitude appears exclusively in a single additive term, which is suppressed by a factor of k^{-2}. This implies that the Doppler contribution becomes significant only at large scales (small k). However, measurements on such scales are strongly affected by *cosmic variance**, introducing increased noise and thereby limiting the precision of the analysis. In contrast,

*A thorough discussion of this aspect is presented later in the text.

Eq. (4.7) contains an imaginary component that scales as k^{-1}, which potentially allows for its detection at intermediate scales, where cosmic variance is less dominant.

Fig. 4.2 further emphasizes the differences in the amplitudes of the various contributions. First, it shows that the term independent of k dominates, with values > 1, whereas the Doppler-dependent terms are significantly smaller, with amplitudes $\ll 1$. Furthermore, the imaginary Doppler component exhibits substantially higher amplitudes (ranging from 10^3 down to 10) compared to the real Doppler term. Both of these observations are consistent with the predictions discussed previously. Finally, it is worth noting that the imaginary contribution can take negative values in the cross power spectrum; hence, it is necessary to consider its absolute value in order to allow for a consistent comparison with the other amplitudes.

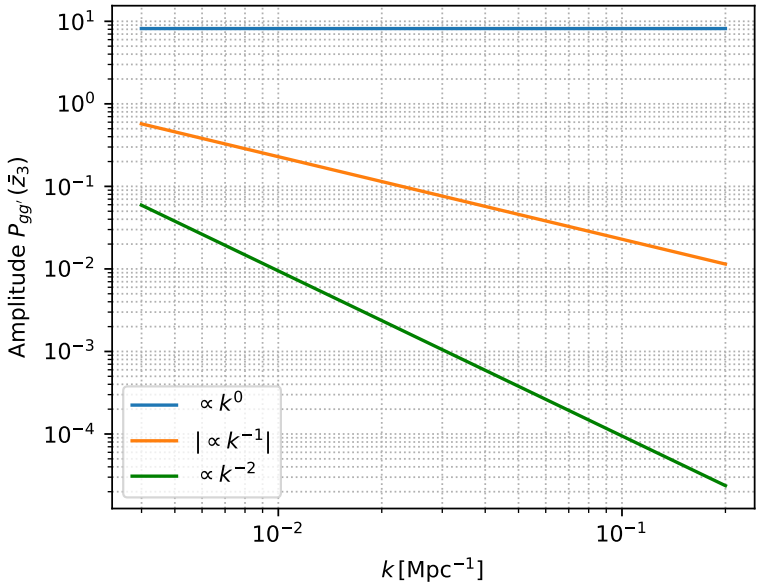


FIGURE 4.2: Amplitudes of the different terms of the cross spectrum, $P_{gg'}$ evaluated $\bar{z} = 0.467$), using the BGS (see Section 5.1). Here $\propto k^0$ refers to the term $\left(b_g + f\mu^2\right)\left(b_{g'} + f\mu^2\right)$, $\propto k^1$ to $\frac{\mathcal{H}}{k}\left[\alpha_g\left(b_{g'} + f\mu^2\right) - \alpha_{g'}\left(b_g + f\mu^2\right)\right] f\mu$, $\propto k^2$ to $\frac{\mathcal{H}^2}{k^2}\alpha_g\alpha_{g'}f^2\mu^2$.

4.3 Multipoles of the Cross Power Spectrum

A direct analysis of Eqs. (4.7) and (4.8) was previously performed in [15, 16], where the Doppler amplitude was constrained with a good precision. Building on these results, our next objective is to develop a Legendre polynomial framework that reduces the degrees of

freedom from (k, μ) to k alone. This reduction enables the analysis to be performed with a substantially smaller amount of data, and is expected to retain nearly the same level of information [18].

Since the power spectrum exhibits anisotropy along the line of sight, it can be decomposed into an orthonormal basis that depends on μ. We choose this basis to be formed by Legendre polynomials, allowing the power spectrum to be expanded as a sum of multipoles [12, 13],

$$\mathcal{P}_{gg'}(k,\mu) = \sum_{\ell} \mathcal{P}^{\ell}_{gg'}(k)\, \mathcal{L}_{\ell}(\mu), \tag{4.9}$$

where $\mathcal{L}_l(\mu)$ are the standard Legendre polynomials. This choice is motivated by their parity symmetry and completeness, which ensures that the multipole coefficients can be obtained via the orthogonality relation [25]

$$\mathcal{P}^{\ell}_{gg'}(k) = \frac{2\ell+1}{2} \int_{-1}^{1} \mathcal{P}_{gg'}(k,\mu)\mathcal{L}_{\ell}(\mu)\, d\mu. \tag{4.10}$$

In particular, Eq. (4.7) can be written as a polynomial expansion in μ, with the real part containing only even powers and the imaginary part only odd powers. Due to the parity of the Legendre polynomials, even powers of μ project exclusively onto even multipoles, while odd powers project exclusively onto odd multipoles. In other words, for even ℓ, $\mathcal{L}_{\ell}(\mu)$ contains only even terms in μ, so when multiplied by Eq. (4.7) the integrand preserves even parity, and only even powers survive the integration. Conversely, for odd ℓ, $\mathcal{L}_{\ell}(\mu)$ contains odd terms, flipping the parity of the product such that only the initially odd powers contribute. Consequently, it becomes possible to isolate the imaginary component within the odd poles. In contrast, Eq. (4.8) lacks the imaginary component, so odd powers will be absent, and therefore only even poles will appear.

Starting with the auto power spectrum, the multipole moments $\mathcal{P}^{\ell}_{g}(k)$ are given by [12]

$$\mathcal{P}^{\ell}_{g}(k) = \frac{2\ell+1}{2} \int_{-1}^{1} \left[\left(b_g + f\mu^2 \right)^2 + \left(\frac{\mathcal{H}\alpha_g f\mu}{k} \right)^2 \right] \mathcal{P}_m(k)\mathcal{L}_{\ell}(\mu)\, d\mu. \tag{4.11}$$

where the non-vanishing multipole contributions are*

*The conventional labels for the multipoles are: $\ell = 0$ (monopole), $\ell = 1$ (dipole), $\ell = 2$ (quadrupole), and so on. These names follow the rule that the number of poles is 2^{ℓ}: for instance, the dipole has 2 poles and the quadrupole has 4.

$$\mathcal{P}_g^0(k) = \left(b_g^2 + \frac{2b_g f}{3} + \frac{f^2}{5} + \frac{\mathcal{H}^2 f^2 \alpha_g^2}{3k^2}\right)\mathcal{P}_m(k), \tag{4.12}$$

$$\mathcal{P}_g^2(k) = \frac{2}{21} f\left(14 b_g + f\left(6 + \frac{\mathcal{H}^2 7\alpha_g^2}{k^2}\right)\right)\mathcal{P}_m(k) \tag{4.13}$$

$$\mathcal{P}_g^4(k) = \frac{8f^2}{35}\mathcal{P}_m(k), \tag{4.14}$$

which are in fact restricted to even poles. On the other hand, the multipoles moments $\mathcal{P}_{gg'}^{\ell}(k)$ of the cross power spectrum are given by [13]

$$\mathcal{P}_{gg'}^{\ell}(k) = \frac{2\ell+1}{2}\int_{-1}^{1}\left[\left(b_g + f\mu^2\right)\left(b_{g'} + f\mu^2\right) + \frac{\mathcal{H}^2}{k^2}\alpha_g\alpha_{g'}f^2\mu^2 \right.$$
$$\left. -\mathrm{i}\frac{\mathcal{H}}{k}\left[\alpha_g\left(b_{g'} + f\mu^2\right) - \alpha_{g'}\left(b_g + f\mu^2\right)\right] f\mu\right]\mathcal{P}_m(k)\mathcal{L}_\ell(\mu)\, d\mu. \tag{4.15}$$

The non-vanishing multipole contributions are

$$\mathcal{P}_{gg'}^0(k) = \left(b_g b_{g'} + \frac{\left(b_g + b_{g'}\right) f}{3} + \frac{f^2}{5} + \frac{\mathcal{H}^2 f^2 \alpha_g \alpha_{g'}}{3k^2}\right)\mathcal{P}_m(k), \tag{4.16}$$

$$\mathcal{P}_{gg'}^1(k) = -\frac{if\mathcal{H}\left(5(b_{g'}\alpha_g - b_g\alpha_{g'}) + 3f(\alpha_g - \alpha_{g'})\right)}{5k}\mathcal{P}_m(k), \tag{4.17}$$

$$\mathcal{P}_{gg'}^2(k) = \frac{2}{21} f\left(7(b_g + b_{g'}) + f\left(6 + \frac{\mathcal{H}^2 7\alpha_g\alpha_{g'}}{k^2}\right)\right)\mathcal{P}_m(k), \tag{4.18}$$

$$\mathcal{P}_{gg'}^3(k) = -\frac{2if^2\mathcal{H}(\alpha_g - \alpha_{g'})}{5k}\mathcal{P}_m(k) \tag{4.19}$$

$$\mathcal{P}_{gg'}^4(k) = \frac{8f^2}{35}\mathcal{P}_m(k). \tag{4.20}$$

The characteristics of the multipole amplitudes follow those of the corresponding components, i.e., even and odd multipoles exhibit the same k-dependence as the real and imaginary parts of Eq. (4.7) (or Eq. (4.8) in the case of the auto power spectrum), respectively. Therefore, the analysis presented at the end of Sec. 4.2 remains valid, as confirmed by Fig. 4.3, where the multipoles of the real part reach amplitudes larger than the underlying power spectrum of matter, whereas the imaginary part has amplitudes much smaller than one.

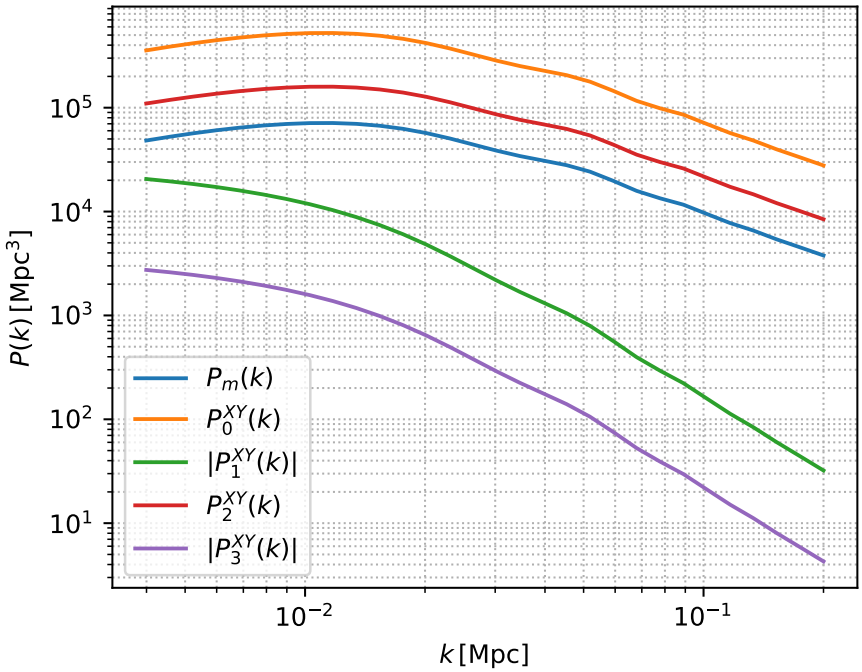


FIGURE 4.3: Legendre multipoles ($\ell = 0, 1, 2, 3$) of the cross-power spectrum $\mathcal{P}_{gg'}(k)$ evaluated at $\bar{z} = 0.467$), using the BGS (see Section 5.1). For reference, these results are compared against the underlying matter power spectrum.

4.4 Discrete Fourier Transform and Estimators of the Galaxy Power Spectrum

It is important to emphasize that cosmological surveys provide discrete data points rather than continuous fields. Consequently, any practical analysis of the galaxy density field must ultimately be formulated in terms of the discrete Fourier transform. In this section, we review the standard formalism used in the literature for transitioning between continuous and discrete descriptions in the context of galaxy power spectrum estimation*.

Consider a survey mapping a cubic comoving volume of side length L, discretized into a regular grid of $K^3_{\rm grid}$ points. The galaxy density contrast field is then defined on this grid, and its discrete Fourier transform is expressed as [4]

$$\delta_{\rm g}(\boldsymbol{k}) = L^{3/2} \sum_{i}^{K^3_{\rm grid}} \delta_{{\rm g},\boldsymbol{r}_i} e^{-i\boldsymbol{k}\cdot\boldsymbol{r}_i}, \quad \text{with} \quad \boldsymbol{k} \in \Big(n_x, n_y, n_z\Big)\, k_F, \tag{4.21}$$

where $(n_x, n_y, n_z) \in \mathbb{Z}$ are integers ranging from $-K_{\rm grid}/2$ to $K_{\rm grid}/2$, and the *fundamental wavenumber* k_F is defined as

*For further details of the derivation, the reader is referred to Appendix A.

$$k_F = \frac{2\pi}{L}. \tag{4.22}$$

The discretization of Fourier in Eq. (4.21) is not solely motivated by the fact that galaxy surveys provide data in the form of discrete points, it also reflects that surveys are limited to a finite comoving volume $V = L^3$. This restriction to a finite volume imposes boundary conditions, which in turn quantize the allowed Fourier modes. Specifically, the wavenumbers $\boldsymbol{k}$ are limited to discrete values that are integer multiples of the fundamental wavenumber. Mathematically, this quantization arises because any function defined on a finite, periodic domain admits a discrete Fourier series representation. In our case, the density field is defined only within the survey volume, which is effectively treated as a periodic box, thereby enforcing the discreteness of the Fourier modes. Physically, this discretization means we have access to only a limited set of independent modes. For example, we cannot resolve structures on scales larger than the survey box (i.e., $k < k_F$ modes are inaccessible), nor can we probe arbitrarily small scales due to resolution limits and observational noise. The finite number of modes available in each k-bin translates into statistical uncertainty in the measurement of the power spectrum, a phenomenon known as *cosmic variance*. This uncertainty persists even in the absence of instrumental noise or shot noise, because it reflects the fundamental limit imposed by our partial view of the Universe.

To estimate the galaxy power spectrum from the observed data, the Fourier modes are binned into spherical shells in $\boldsymbol{k}$-space. Each shell, labeled by an index α, includes all modes satisfying

$$k_\alpha - \Delta k/2 \leq |\boldsymbol{k}| < k_\alpha + \Delta k/2, \tag{4.23}$$

where Δk is the bin width. The number of independent modes within each shell, $N_{k,i}$, is computed by dividing the volume of the shell in Fourier space, $4\pi k_i^2 \Delta k$, by the volume of a single Fourier mode (i.e., the volume of the fundamental cell), k_F^3. This yields* [4, 15, 16]

$$N_{k,i} = \frac{4\pi k_i^2 \Delta k}{k_F^3}. \tag{4.24}$$

Expressed in terms of the total survey volume $V = L^3$, this simplifies to

*There is a minor inconsistency in the literature. While in [4] a factor of $1/2$ appears due to the condition in Eq. (4.4), more recent works such as [15, 16] omit this factor. We follow the more recent convention for consistency.

$$N_{k,i} = \frac{1}{2\pi^2} V k_i^2 \Delta k. \tag{4.25}$$

The estimator for the auto galaxy power spectrum $\hat{P}_g(k_i)$ is then defined as the average over all modes in shell i [4]

$$\hat{\mathcal{P}}_g(k_i) = \frac{1}{N_{k,i}} \sum_{\boldsymbol{k}}^{||\boldsymbol{k}|-k_i|<\Delta k/2} \left\langle \left|\delta_{g,\boldsymbol{k}}\right|^2 \right\rangle - \mathcal{P}_g^N, \tag{4.26}$$

where $\mathcal{P}_g^N$ is the noise contribution. Under the assumption of Poisson noise*, which is commonly used in forecasting analyses, this term is given by [4, 15, 16]

$$\mathcal{P}_g^N = \bar{n}_g^{-1}, \tag{4.27}$$

where $\bar{n}_g$ is the mean galaxy number density.

The uncertainty in $\hat{\mathcal{P}}_g(k_i)$ is quantified via its *covariance*, defined as [4]

$$\begin{aligned} \mathrm{Cov}\left[\hat{\mathcal{P}}_{\mathrm{g}}\left(k_i\right), \hat{\mathcal{P}}_{\mathrm{g}}\left(k_j\right)\right] &\equiv \left\langle \hat{\mathcal{P}}_{\mathrm{g}}\left(k_i\right) \hat{\mathcal{P}}_{\mathrm{g}}\left(k_j\right) \right\rangle - \left\langle \hat{\mathcal{P}}_{\mathrm{g}}\left(k_i\right) \right\rangle \left\langle \hat{\mathcal{P}}_{\mathrm{g}}\left(k_j\right) \right\rangle \\ &= \frac{1}{N_{k,i}} \sum_{\boldsymbol{k}}^{||\boldsymbol{k}|-k_i|<\Delta k/2} \frac{1}{N_{k,j}} \sum_{\boldsymbol{k}'}^{|\boldsymbol{k}'|-k_j|<\Delta k/2} \times \\ &\left[\left\langle \left|\delta_{g,\boldsymbol{k}}\right|^2 \left|\delta_{g,\boldsymbol{k}'}\right|^2 \right\rangle - \left\langle \left|\delta_{g,\boldsymbol{k}}\right|^2 \right\rangle \left\langle \left|\delta_{g,\boldsymbol{k}'}\right|^2 \right\rangle \right]. \end{aligned} \tag{4.28}$$

In deriving the second line, we have substituted the estimator defined in Eq. (4.26) and omitted the constant $\mathcal{P}_g^N$, which cancels out in the difference of expectation values.

The expectation value on the right-hand side involves four instances of δ_g, and can be expanded using *Wick's theorem* for Gaussian fields† [4]

$$\begin{aligned} \left\langle \left|\delta_{g,\boldsymbol{k}}\right|^2 \left|\delta_{g,\boldsymbol{k}'}\right|^2 \right\rangle &= \left\langle \delta_{g,\boldsymbol{k}}\, \delta_{g,-\boldsymbol{k}}\, \delta_{g,\boldsymbol{k}'}\, \delta_{g,-\boldsymbol{k}'} \right\rangle \\ &= \left\langle \delta_{g,\boldsymbol{k}}\, \delta_{g,-\boldsymbol{k}} \right\rangle \left\langle \delta_{g,\boldsymbol{k}'}\, \delta_{g,-\boldsymbol{k}'} \right\rangle \\ &\quad + \left\langle \delta_{g,\boldsymbol{k}}\, \delta_{g,\boldsymbol{k}'} \right\rangle \left\langle \delta_{g,-\boldsymbol{k}}\, \delta_{g,-\boldsymbol{k}'} \right\rangle \\ &\quad + \left\langle \delta_{g,\boldsymbol{k}}\, \delta_{g,-\boldsymbol{k}'} \right\rangle \left\langle \delta_{g,-\boldsymbol{k}}\, \delta_{g,\boldsymbol{k}'} \right\rangle \end{aligned} \tag{4.29}$$

*For a more detailed explanation of Poisson noise and discrete derivation, see Appendix A.

†Inflationary theory predicts that the initial fluctuations of the Universe can be well described by a Gaussian random field. Furthermore, as long as the subsequent evolution remains within the linear regime, the statistical properties of the field are preserved and remain Gaussian [5].

The first term in Eq. (4.29) precisely cancels the second term in Eq. (4.28). Thus, only the second and third terms remain. For our discrete Fourier definition in Eq. (4.21), the two-point correlation in Fourier space is given by [4, 26]

$$\left\langle \delta_{g,\boldsymbol{k}}\, \delta_{g,\boldsymbol{k}'} \right\rangle = \delta_{\boldsymbol{k},-\boldsymbol{k}'} \left[\mathcal{P}_{\rm g}(k) + \mathcal{P}_N \right] \tag{4.30}$$

where $\delta_{\boldsymbol{k},-\boldsymbol{k}'}$ is the Kronecker delta, equal to 1 when $\boldsymbol{k} = -\boldsymbol{k}'$ and 0 otherwise. Note that these simple forms follow from the inclusion of the normalization factor $L^{3/2}$ in Eq. (4.21), which allows us to make the correspondence

$$(2\pi)^3 \delta_{\rm D}^{(3)} \left(\boldsymbol{k} + \boldsymbol{k}' \right) \to \delta_{\boldsymbol{k},-\boldsymbol{k}'} \tag{4.31}$$

Returning to Eq. (4.28), we observe that the remaining terms from Eq. (4.29) only contribute when the bins i and j overlap. Therefore, in the typical case of non-overlapping bins*, the covariance matrix is diagonal (i.e., $\mathrm{Cov}_{ij} = 0$ for $i \neq j$). For $i = j$, there are exactly two contributions per $\boldsymbol{k}$: one from $\boldsymbol{k}' = \boldsymbol{k}$, and one from $\boldsymbol{k}' = -\boldsymbol{k}$. Hence, the final expression for the covariance of the auto galaxy power spectrum is [4, 26]

$$\mathrm{Cov}\left[\hat{\mathcal{P}}_{\rm g}\left(k_i\right), \hat{\mathcal{P}}_{\rm g}\left(k_j\right) \right] = \frac{2}{N_{k,i}} \left[\mathcal{P}_{\rm g}\left(k_i\right) + \mathcal{P}_g^N \right]^2 \delta_{ij} \tag{4.32}$$

Even for an infinitely dense galaxy sample, so that $\mathcal{P}_N \to 0$, a minimum error remains, which is the sample variance due to the finite number of modes available in the survey volume V (Eq. (4.25)). For notational convenience, we restrict the indices to k and k', introduce

$$\tilde{\mathcal{P}}_g(\boldsymbol{k}) = \mathcal{P}_{\rm g}(\boldsymbol{k}) + \mathcal{P}_g^N,$$

and rewrite the summation term as

$$\sum_{\boldsymbol{k}}^{|\boldsymbol{k}|-k_i|<\Delta k/2} \longrightarrow \sum_{\boldsymbol{k}}.$$

It follows directly that the estimator for the cross power spectrum between two galaxy populations g and g' observables is given by

*Non-overlapping bins are typically used because they ensure that each Fourier mode contributes to only one k-bin, avoiding redundancy and artificial correlations between bins. This choice simplifies the covariance structure, making it approximately diagonal, which is especially convenient for forecasting and Fisher matrix analyses.

$$\hat{\mathcal{P}}_{gg'}\boldsymbol{k}) = \frac{1}{N_k}\sum_{\boldsymbol{k}}\left\langle \delta_g(\boldsymbol{k})\delta_{g'}(-\boldsymbol{k})\right\rangle - \mathcal{P}^N_{gg'}, \tag{4.33}$$

where $\mathcal{P}^N_{gg'}$ denotes the shot-noise contribution to the cross-spectrum. For two distinct non-overlapping galaxy samples, this term vanishes, i.e.

$$\mathcal{P}^N_{gg'} = 0. \tag{4.34}$$

This statement assumes that the two galaxy populations are statistically independent at the level of Poisson sampling. If the samples overlap, a residual correlated shot-noise contribution may arise. In this work we restrict ourselves to the idealized case of disjoint samples which is we can do using a single catalogue.

In complete analogy with the auto-spectrum case, the covariance of the cross power spectrum is [15, 16]

$$\mathrm{Cov}\left[\hat{\mathcal{P}}_{gg'}\left(k,\mu\right),\hat{\mathcal{P}}_{gg'}\left(k',\mu'\right)\right] = \frac{1}{N_k}\left[\tilde{\mathcal{P}}_g(k,\mu)\tilde{\mathcal{P}}_{g'}(k,\mu) + \mathcal{P}_{gg'}(k,\mu),\mathcal{P}_{g'g}(k,\mu)\right]. \tag{4.35}$$

The first term in brackets accounts for the variance of the two auto-spectra, while the second term encodes correlations arising from the cross-spectrum itself.

From Eq.(4.33), the estimatores of the multipole expasion will given by

$$\hat{\mathcal{P}}^{\ell}_{gg'}(k) = \frac{2\ell+1}{N_k}\sum_{\boldsymbol{k}}\int_{-1}^{1} d\mu\left\langle \delta_g(\boldsymbol{k})\delta_{g'}(-\boldsymbol{k})\right\rangle, \tag{4.36}$$

whose covariance is defined as [18, 26]

$$\begin{aligned}
&\mathrm{Cov}\left[\mathcal{P}^{\ell_1}_{gg'}\left(k\right),\mathcal{P}^{\ell_2}_{gg'}\left(k'\right)\right] = \\
&= \frac{2\ell_1+1}{2}\frac{2\ell_2+1}{2}\int_{-1}^{1}\int_{-1}^{1}\mathrm{d}\mu\mathrm{d}\mu'\mathcal{L}_{\ell_1}(\mu)\mathcal{L}_{\ell_2}(\mu')\,\mathrm{Cov}\left[\mathcal{P}_{gg'}\left(k,\mu\right),\mathcal{P}_{gg'}\left(k',\mu'\right)\right] = \\
&= \frac{2\ell_1+1}{2}\frac{2\ell_2+1}{2}\int_{-1}^{1}\int_{-1}^{1}\mathrm{d}\mu\mathrm{d}\mu'\mathcal{L}_{\ell_1}(\mu)\mathcal{L}_{\ell_2}(\mu')\,(2\pi)^3\times \\
&\times\left[\delta\left(\boldsymbol{k}+\boldsymbol{k}'\right)\tilde{\mathcal{P}}_g\left(k,\mu\right)\tilde{\mathcal{P}}_{g'}\left(k,\mu\right)+\delta\left(\boldsymbol{k}-\boldsymbol{k}'\right)\mathcal{P}_{gg'}\left(k,\mu\right)\mathcal{P}_{g'g}\left(k,\mu\right)\right] = \\
&= \frac{2\ell_1+1}{2}\frac{2\ell_2+1}{2}\int_{-1}^{1}\mathrm{d}\mu\mathcal{L}_{\ell_1}(\mu)\mathcal{L}_{\ell_2}(\mu)\times \\
&\times(2\pi)^3\left[\delta\left(k+k'\right)\tilde{\mathcal{P}}_g\left(k,\mu\right)\tilde{\mathcal{P}}_{g'}\left(k,\mu\right)+\delta\left(k-k'\right)\mathcal{P}_{gg'}\left(k,\mu\right)\mathcal{P}_{g'g}\left(k,\mu\right)\right].
\end{aligned} \tag{4.37}$$

Applying the discretization in k-space (Eq. (4.31)) and summing over all k , we obtain

$$\mathrm{Cov}\left[\mathcal{P}^{\ell_1}_{gg'}(k),\mathcal{P}^{\ell_2}_{gg'}(k')\right] = \frac{(2\ell_1+1)(2\ell_2+1)}{4N_k}\int_{-1}^{1}\mathrm{d}\mu\mathcal{L}_{\ell_1}(\mu)\mathcal{L}_{\ell_2}(\mu)\times \\ \times\left[\tilde{\mathcal{P}}_g(k,\mu)\tilde{\mathcal{P}}_{g'}(k,\mu)+\mathcal{P}_{gg'}(k,\mu)\mathcal{P}_{g'g}(k,\mu)\right]. \tag{4.38}$$

Finally, due to the imaginary component of our observables, it is possible to construct estimators that independently isolate the symmetric and antisymmetric parts of the cross-power spectrum [17]. These correspond, in essence, to the real and imaginary components of the cross-power spectrum itself. For the antisymmetric part, we define [17]

$$\hat{\mathcal{P}}^{I}_{gg'}(k,\mu) = \frac{1}{N_k}\sum_{\boldsymbol{k}}\left\langle \mathrm{Im}\left[\delta_g(\boldsymbol{k})\delta_{g'}(-\boldsymbol{k})\right]\right\rangle \\ = \frac{1}{N_k}\sum_{\boldsymbol{k}}\left\langle\frac{\delta_g(\boldsymbol{k})\delta_{g'}(-\boldsymbol{k})-\delta_{g'}(\boldsymbol{k})\delta_g(-\boldsymbol{k})}{2i}\right\rangle, \tag{4.39}$$

and for the symmetric part, we have

$$\hat{\mathcal{P}}^{R}_{gg'}(k,\mu) = \frac{1}{N_k}\sum_{\boldsymbol{k}}\left\langle \mathrm{Re}\left[\delta_g(\boldsymbol{k})\delta_{g'}(-\boldsymbol{k})\right]\right\rangle \\ = \frac{1}{N_k}\sum_{\boldsymbol{k}}\left\langle\frac{\delta_g(\boldsymbol{k})\delta_{g'}(-\boldsymbol{k})-\delta_{g'}(\boldsymbol{k})\delta_g(-\boldsymbol{k})}{2}\right\rangle. \tag{4.40}$$

These two estimators are expected to contain the same information as Eq. (4.33). However, because the antisymmetric estimator isolates the Doppler effect, it may provide tighter constraints on this signal than Eq. (4.33). Moreover, these estimators can be further expanded into multipoles, following the same procedure used in Eq. (4.36), since the dependence on μ remains. In addition, because parity is now separated by symmetry, the multipoles of the symmetric estimator, $\hat{\mathcal{P}}^{R}_{\ell}$, are non-vanishing only for even ℓ, whereas those of the antisymmetric estimator, $\hat{\mathcal{P}}^{I}_{\ell}$, are non-vanishing only for odd ℓ. A detailed discussion of the covariance of the symmetric and antisymmetric estimators, as well as their multipoles, is deferred to the next chapter.

Having established this final methodological component, we now turn to evaluating the constraining power on the Doppler parameters.

Chapter 5

Prospects of Constraining the Doppler effect in Future Surveys

In the previous chapter, we developed the framework of Legendre multipoles as well as the symmetric and anti-symmetric estimators of the cross-power spectrum. We now turn to the question of how tightly the Doppler effect can be constrained. To this end, we first introduce the reference sample on which our analysis is based, following [15, 16]. As an intermediate step, we evaluate the signal-to-noise ratio of these observables, which enables us to quantify their statistical power and, ultimately, their ability to constrain the Doppler parameters. Finally, we perform a Fisher matrix analysis to assess the achievable parameter constraints and to explore potential degeneracies among them [18, 27].

5.1 DESI-like low redshift Bright Galaxy Sample

The Dark Energy Spectroscopic Instrument (DESI) [20] survey includes a dedicated Bright Galaxy Sample (BGS) designed to target the brightest galaxies at low redshift, complementing higher-redshift tracers such as emission line galaxies and quasars. The DESI BGS is expected to observe over 10 million galaxies up to redshift $z < 0.6$ across $\sim 14{,}000\,\mathrm{deg}^2$[15], making it one of the most powerful low-redshift probes for large-scale structure. Such low-redshift samples are particularly well suited for Doppler contribution studies, as this effect has been shown to dominate in this regime [15, 16, 24].

For this reason, we make use of the DESI-like low-redshift BGS parameter fits provided in [15] to investigate the relativistic Doppler contribution in a realistic observational

setup*. In this sample, apparent magnitudes m are defined from the observed flux F as $m = -2.5 \log_{10} F + \text{const}$. A cut-off magnitude of $m_c = 20.175$ is adopted in the r-band†. The sample further allows for an additional luminosity cut within the BGS, enabling the construction of faint and bright sub-samples, and thus two tracers from a single galaxy population. In this case, the faint sample comprises sources with observed magnitudes in the range $(m_s, m_c]$, while the bright sample includes all galaxies with $m \leq m_s$. The optimal sensitivity to the Doppler amplitude is achieved when the split is set at $m_s = 19.0$ [16], which also corresponds to the parameter values adopted here. We use the fits of [15] at three representative redshifts (see Table 5.1)‡. For this thesis, we will assume a survey area of 10,000 deg^2 which is consistent with DESI DR2 [28] and a ΛCDM cosmology as introduced in Chapter 2.

$\bar{z}$	n_{bright} $[h^3\,\text{Mpc}^{-3}]$	α_{bright}	b_{bright}	n_{faint} $[h^3\,\text{Mpc}^{-3}]$	α_{faint}	b_{faint}
$\bar{z}_1 = 0.13$	1.73×10^{-2}	1.78	1.15	1.38×10^{-2}	11.19	1.10
$\bar{z}_2 = 0.30$	5.62×10^{-4}	−7.50	1.63	2.14×10^{-3}	−1.20	1.30
$\bar{z}_3 = 0.47$	4.01×10^{-6}	−13.06	3.02	1.10×10^{-4}	−5.11	2.06

TABLE 5.1: Survey characteristics for bright (g) and faint (g') galaxies in the DESI-like low-redshift Bright Galaxy Sample (BGS), including number densities (n_g), Doppler (α_g), and bias parameters (b_g) at three mean redshifts $\bar{z}$ [15].

5.2 Signal-to-Noise Ratio Analysis

Although our estimators allow us to isolate the Doppler effect, their detection may not be straightforward and, consequently, they might not yield robust constraints. To address this, we evaluate the expected noise in their signal and assess their constraining power. For this purpose, we employ the signal-to-noise ratio (SNR), defined as

$$\text{SNR} = \frac{X}{\sqrt{\Gamma_X}}, \tag{5.1}$$

where X denotes the estimator (or signal) under consideration and

$$\Gamma_X = \text{Cov}[X, X]. \tag{5.2}$$

*We will not elaborate on how galaxies are modeled, but only highlight the information that is essential for our purposes. For further details, we refer the reader to [15].

†The r-band refers to a photometric filter centered in the red part of the visible spectrum, which is commonly used in galaxy surveys.

‡We thank the authors for kindly sharing the tabulated results, which we employ instead of the analytic fitting functions provided in the paper.

is the corresponding noise.

5.2.1 SNR of Legendre Multipoles of the Cross-Power Spectrum

We begin by evaluating the SNR of the Legendre multipoles $\mathcal{P}_\ell$, whose covariance is defined in Eq. (4.38). Since our aim is to assess the SNR of each multipole individually, we restrict our covariance to the cases with $\ell_1 = \ell_2 = \ell$, which further reduces Eq. (4.38) to

$$\Gamma_\ell(k) = \frac{(2\ell+1)^2}{4N_k} \int_{-1}^{1} \mathrm{d}\mu \left(\mathcal{L}_\ell(\mu)\right)^2 \left[\tilde{\mathcal{P}}_g\left(k,\mu\right) \tilde{\mathcal{P}}_{g'}\left(k,\mu\right) + \mathcal{P}_{gg'}\left(k,\mu\right) \mathcal{P}_{g'g}\left(k,\mu\right)\right]. \quad (5.3)$$

Before computing the SNR, it is important to note that the dipole and octopole multipoles, given in Eqs. (4.17) and (4.19), are purely imaginary. To account for this, we take their absolute values, which leads to a redefinition of the SNR as

$$\mathrm{SNR}(k) = \frac{\left|\mathcal{P}^{\ell}_{gg'}(k)\right|}{\sqrt{\Gamma_\ell(k)}}, \quad (5.4)$$

where $\sqrt{\Gamma_\ell(k)}$ is given by Eq. (5.3).

The results of this calculation are presented in Fig. 5.1, which shows the SNR of the Legendre multipoles of the cross-power spectrum $\mathcal{P}_{gg'}$ (in units of Mpc^3) as a function of the wavenumber k (Mpc^{-1}) for three representative mean redshifts. Each panel corresponds to a different multipole: monopole ($\ell = 0$), dipole ($\ell = 1$), quadrupole ($\ell = 2$), and octopole ($\ell = 3$)* . The monopole exhibits the highest values, peaking above SNR ~ 250 and increasing with k, although the dependence on redshift is non-monotonic. The quadrupole follows a similar trend but with a maximum SNR ~ 25. In contrast, the dipole and octopole display significantly smaller amplitudes, with peak values SNR $\lesssim 0.5$ and SNR $\lesssim 0.06$, respectively.

The most striking feature of these results is that the odd multipoles exhibit SNR < 1. This indicates that the statistical noise dominates over the signal, rendering any potential detection based on these estimators indistinguishable from noise.† While odd multipoles were initially expected to provide a clean probe of Doppler contributions, since these are isolated in the imaginary component, their poor SNR values imply that such estimators are not viable.

*We restrict this analysis to multipoles up to the octopole, since only these are directly sensitive to Doppler effects, even though the remaining even multipoles are much less affected than the odd ones.

†In cosmology, constraints with SNR $\gtrsim 10$ are typically regarded as good, while SNR $\lesssim 5$ are considered poor [29].

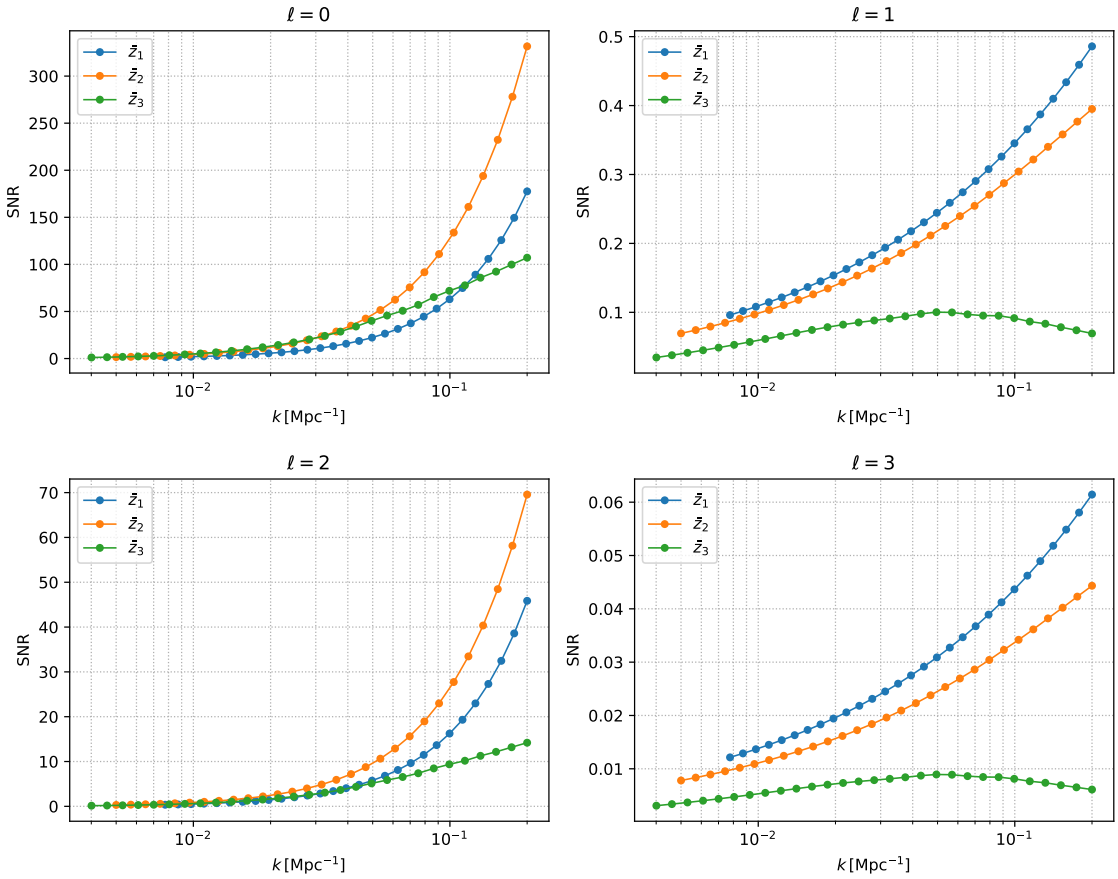


FIGURE 5.1: SNR of the Legendre multipoles ($\ell = 0, 1, 2, 3$) of the cross-power spectrum $\mathcal{P}_{gg'}$ for three mean redshifts ($\bar{z}_1 = 0.133$, $\bar{z}_2 = 0.300$, and $\bar{z}_3 = 0.467$) with the BGS. Each panel corresponds to a different multipole order. The markers represent the discrete values in k, while the solid line denotes the fitted function.

To understand this outcome, recall that Doppler-dependent contributions are intrinsically suppressed compared to the Newtonian terms. Although the odd multipoles isolate these contributions at the level of the power spectrum, the situation changes when computing the covariance,

$$\mathrm{Cov}\left[\mathcal{P}_{gg'}(k,\mu), \mathcal{P}_{gg'}(k',\mu')\right],$$

which has contributions of two terms, namely

$$\left(P_g(k,\mu) + N_g\right)\left(P_{g'}(k,\mu) + N_{g'}\right) \quad \text{and} \quad \mathcal{P}_{gg'}(k,\mu)\,\mathcal{P}_{g'g}(k,\mu).$$

The first is a product of two polynomials containing only even powers in μ, and it is therefore straightforward that the result also remains an even polynomial. The second term involves the product

$$\Big(A + B\mu^2 + C\mu^4 + i(D\mu + E\mu^3)\Big) \times \Big(A + B\mu^2 + C\mu^4 + i(D\mu + E\mu^3)\Big) = \Big(A + B\mu^2 + C\mu^4\Big)^2 + \Big(D\mu + E\mu^3\Big)^2,$$

from which it is again trivial to verify that only even powers of μ remain. As a consequence, all μ-dependencies become even, and the integral is non-vanishing only when $\mathcal{L}_{\ell_1}(\mu)\mathcal{L}_{\ell_2}(\mu)$ is also even. This condition is satisfied whenever $\ell_1 = \ell_2$, in which case the product is a squared polynomial and thus even, or more generally when $\ell_1 + \ell_2$ is even. Therefore, the real contributions inevitably survive in the covariance of the odd multipoles, driving their variance to be larger than their corresponding signal.

This observation, although negative in terms of odd-multipole detectability, is in fact encouraging for the anti-symmetric estimator and its multipoles. By construction, when isolating the imaginary part explicitly, the real contributions are removed at the observational level and do not propagate into the covariance. Hence, in the next analyses, this contamination is absent, potentially leading to more favorable detectability prospects.

5.2.2 SNR of the Anti-Symmetric Estimator of the Cross Power Spectrum and Its Legendre Multipoles

We now turn to the covariance of the anti-symmetric estimator of the cross power spectrum. In [17], the author computes the covariance for a general anti-symmetric estimator; however, the calculation is performed by considering only a single Fourier mode of k. Such procedure effectively restricts the analysis to an individual mode and neglects the statistical averaging over the ensemble of modes contained in the survey volume. In practice, the covariance must account for the full set of Fourier modes contributing to a given bin in k, as these collectively determine the variance of the estimator. For this reason, we must rederive an expression for the covariance of the imaginary part that properly incorporates the contribution of all modes. Since the derivation is too lengthy, we present it in Appendix B. The resulting covariance is

$$\Gamma_I(k) = \frac{1}{N_{\boldsymbol{k}}} \Big(\mathcal{P}^I_{gg'}(k,\mu)\Big)^2. \tag{5.5}$$

This result shows that, when isolating the imaginary part and including the contribution of all Fourier modes, the only source of statistical uncertainty is cosmic variance, with shot noise making no contribution. This finding is particularly interesting because it is

not restricted to the Doppler effect alone, but applies to all "imaginary" contributions to the density contrast, such as the gravitational redshift [17]. Consequently, this may alter the way in which these imaginary contributions are interpreted and detected in practice.

Returning to our case, in order to compute N_k, we must consider binning not only in k but also in μ. The corresponding number of modes is therefore* [15]

$$N_k = \frac{1}{4\pi^2} V k_i^2 \Delta k \Delta \mu, \tag{5.6}$$

and the SNR follows as

$$\mathrm{SNR}(k) = \frac{\mathcal{P}^I_{gg'}(k,\mu)}{\sqrt{\Gamma_I(k,\mu)}} = \sqrt{N_k}. \tag{5.7}$$

with Fig. 5.2 illustrates this result. It simply reflects the behaviour expected from cosmic variance. A noteworthy aspect is that, compared to the SNR of the odd multipoles in Fig. 5.1, the imaginary part exhibits a significantly higher SNR, with some values exceeding 10, making it a strong signal.

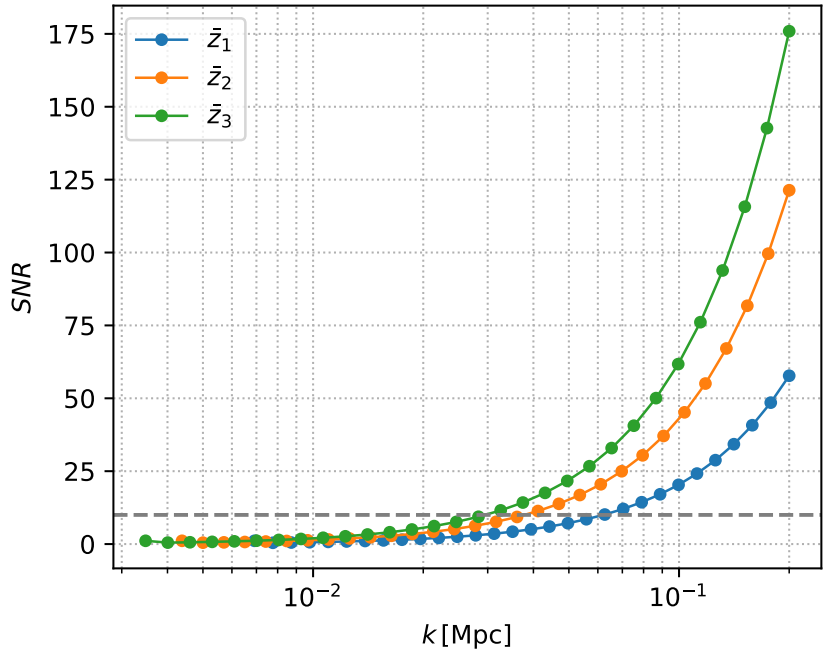


FIGURE 5.2: SNR of the imaginary power spectrum as a function of the wavenumber k for three mean redshifts forecasted with the BGS sample. Dashed grey line represent SNR = 10.

The same procedure used for Eq. (5.3) can now be applied to Eq. (5.5), yielding

*For clarity, we adopt N_k in the first context, and $N_{\boldsymbol{k}}$ in the second.

$$\Gamma^2_\ell(k) = \frac{(2\ell+1)^2}{4N_k} \int_{-1}^{1} \mathrm{d}\mu \left(\mathcal{L}_\ell(\mu)\right)^2 \left(\mathcal{P}^I_{gg'}(k,\mu)\right)^2 . \tag{5.8}$$

The outcome of this calculation is shown in Fig. 5.3. These results are consistent with the trends already observed in Figs. 5.1 and 5.2. In particular, we recover the same favourable signal-to-noise ratios found in Eq. (5.7), as well as the same relative behaviour between the dipole and the octopole from Eq. (5.3). For $\ell = 1$, the SNR exceeds 500, while for $\ell = 3$ it is substantially lower, with values ranging from 0 up to $\lesssim 100$*.

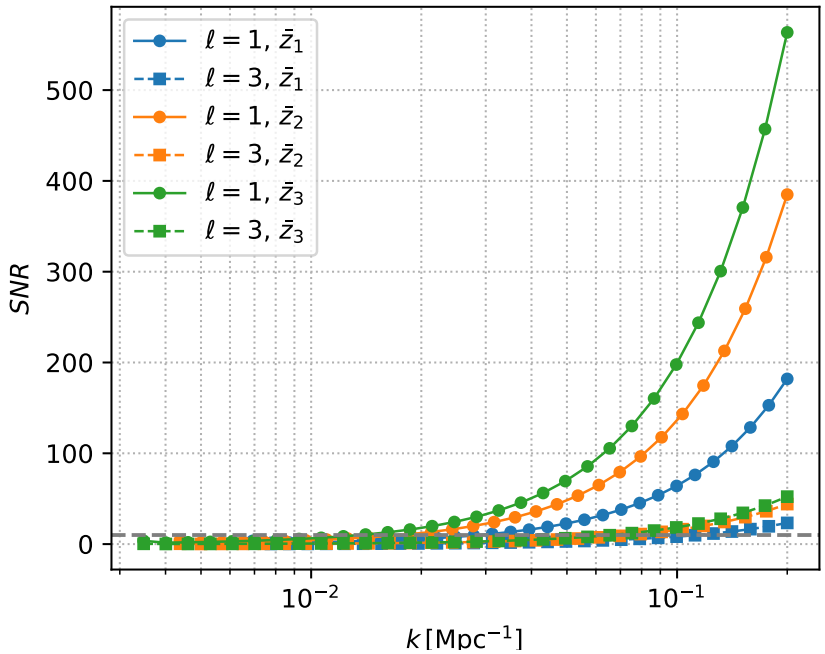


FIGURE 5.3: SNR of the legandre multipoles of the imaginary power spectrum as a function of the wavenumber k for three mean redshifts forecasted with the BGS sample. Dashed grey line represent SNR = 10.

These results confirm that our intuition at the end of the previous subsection was correct: the issue indeed arose because the real part of the cross was also contributing to the odd multipoles. As an additional benefit, we find that the covariance of an anti-symmetric estimator is determined solely by cosmic variance.

Finally, both Fig. (5.2) and Fig. (5.3) show an improvement in the SNR with increasing redshift z. At first glance, this result may appear counterintuitive, since previous studies [15, 16] have shown that higher redshift typically leads to improved performance for a fixed sample.

*This result is somewhat unexpected, as it exceeds the SNR of Eq. (5.7); however, we will return to this point for a more detailed discussion after applying the Fisher matrix formalism.

In the first case, Eqs. (5.7) and (5.6) show that the SNR is directly correlated with the survey volume, which is the only quantity that differs among the three redshift bins considered in this analysis. The survey volume is defined as

$$V_{\rm sur}(z) = \int_{z-\frac{\Delta z}{2}}^{z+\frac{\Delta z}{2}} \frac{r(z')}{H(z')}, dz'. \tag{5.9}$$

This expression makes explicit that increasing the central redshift z leads to a larger survey volume, and consequently to a higher SNR.

For the multipole case, the Legendre multipoles correspond to a linear transformation of the power spectrum involving an average over μ. Therefore, we expect the SNR of the multipoles to scale linearly with the SNR obtained in the previous case, which again explains the observed increase of the SNR with increasing redshift.

5.3 Parameter Analysis

We obtained favourable SNR values for the imaginary estimator and its multipoles, whereas the multipoles of the full cross power spectrum did not exhibit such behaviour. Nevertheless, we include all cases in our analysis to gain a comprehensive understanding of how each contributes to the constraints.

We begin by introducing the Fisher matrix together with a formal definition of the Doppler parameters. We then analyze the degeneracies among them in order to identify which parameters can, and which cannot, be constrained with our observables. Finally, we present the projected relative errors on these parameters to quantify the strength of the constraints.

5.3.1 Fisher Information Matrix

The Fisher information matrix is a central tool in forecasting the constraining power of cosmological surveys. In general, it quantifies the amount of information that an observable carries about a set of parameters $\boldsymbol{\theta} = \{\theta_1, \theta_2, \ldots, \theta_n\}$. Formally, it is defined as the expectation value of the Hessian of the log-likelihood function [27],

$$F_{ij} \equiv -\left\langle \frac{\partial^2 \ln \mathcal{L}(\mathbf{d}|\boldsymbol{\theta})}{\partial\theta_i \, \partial\theta_j} \right\rangle, \tag{5.10}$$

where $\mathcal{L}$ is the likelihood of the data vector $\mathbf{d}$ given the parameters $\boldsymbol{\theta}$.

Under the assumption of Gaussian-distributed observables, the Fisher matrix can be expressed in terms of the derivatives of the model predictions with respect to the parameters and the inverse of the covariance matrix. For a generic data vector $\mathbf{P}$ (in this work, the set of observables), the Fisher matrix in a given redshift bin $\bar{z}_l$ reads [15, 27]

$$F_{ij}(\bar{z}_l) = \sum_{m,n} \frac{\partial \mathbf{P}(\bar{z}_l, \mu_m, k_n)^T}{\partial \theta_i} \, \Gamma^{-1}(\bar{z}_l, \mu_m, k_n) \, \frac{\partial \mathbf{P}(\bar{z}_l, \mu_m, k_n)}{\partial \theta_j}, \tag{5.11}$$

where the sum runs over all configurations in angle μ_m and scale k_n, and Γ denotes the covariance matrix of the power spectra.

When combining multiple redshift bins, the total Fisher information is obtained by summing over the contributions of each bin,

$$F_{ij} = \sum_l F_{ij}(\bar{z}_l), \tag{5.12}$$

so that the cumulative information accounts for the full redshift range of the survey. It is worth noting that in analyses based on power spectrum multipoles, the explicit angular dependence on μ is integrated out. In that case, the Fisher matrix depends only on the wavenumber k.

Finally, the inverse of the Fisher matrix provides the Cramér–Rao bound on the parameter uncertainties. In particular, the marginal error on a parameter θ_α is given by

$$\sigma_{\theta_i} = \sqrt{(F^{-1})_{ii}}. \tag{5.13}$$

This framework thus enables one to quantify the sensitivity of a given survey to the parameters of interest, assess parameter degeneracies, and optimize the analysis strategy.

Since our aim is to test the Doppler contribution, we consider a parameter set that simultaneously includes both the relativistic Doppler coefficients α and the Doppler amplitude A_D, namely

$$\boldsymbol{\theta} = \left\{ \alpha_{g,1}, \alpha_{g',1}, \alpha_{g,2}, \alpha_{g',2}, \alpha_{g,3}, \alpha_{g',3}, A_D \right\}. \tag{5.14}$$

Here the second subscript in the α's labels different mean redshifts. This choice allows us to directly test the relativistic Doppler coefficients α for the different galaxy types and at different redshifts, thus identifying which cases are easier or harder to constrain. The Doppler Amplitude is introduced in Eq. (3.28) as [15]

$$\delta_{g,\mathrm{obs}}(\boldsymbol{k}) = b_g \, \delta_m + f\mu^2 - A_D \, \frac{if\mathcal{H}\mu}{k} \, \alpha_g. \tag{5.15}$$

By definition, the fiducial value is $A_D = 1$ for any galaxy type and redshift, since once the other parameters (including the α's) are known, A_D does not introduce additional freedom. However, this statement holds only if the theoretical framework of GR and in particular the validity of the Euler equation, Eq. (3.21) is assumed. Should GR be violated, the Doppler amplitude may deviate from unity, thereby allowing us to test both the Euler equation and GR itself and that's we tested it.

The Fisher matrix therefore takes the form of a block-diagonal structure of dimension 7×7, in which only terms corresponding to the same redshift interact with each other and with A_D.

As for the data vectors, we will consider the multipoles of the cross-power spectrum, as well as the symmetric and anti-symmetric estimators along with their respective multipoles. The symmetric and anti-symmetric estimators will be evaluated both individually and jointly, and their multipoles will be assessed likewise. The covariance matrix for the real estimator is given by

$$\begin{aligned}\Gamma\left(k,\mu\right) &= \mathrm{Cov}\left[\mathrm{Re}\left[\mathcal{P}_{gg'}\left(k,\mu\right)\right],\mathrm{Re}\left[\mathcal{P}_{gg'}\left(k',\mu'\right)\right]\right] \\ &= \frac{1}{N_{\boldsymbol{k}}}\left[\left(\mathrm{Re}\left[\mathcal{P}_{gg'}\left(k,\mu\right)\right]\right)^2 + \tilde{\mathcal{P}}_g\left(k,\mu\right)\tilde{\mathcal{P}}_{g'}\left(k,\mu\right)\right],\end{aligned} \tag{5.16}$$

while for it's multipoles, one has

$$\begin{aligned}\Gamma_{\ell_1,\ell_2}\left(k\right) = \frac{\left(2\ell_1+1\right)\left(2\ell_2+1\right)}{4N_k}\int_{-1}^{1}\mathrm{d}\mu\left(\mathcal{L}_{\ell_1}(\mu)\right)\left(\mathcal{L}_{\ell_2}(\mu)\right)\times \\ \times\left[\left(\mathrm{Re}\left[\mathcal{P}_{gg'}\left(k,\mu\right)\right]\right)^2 + \tilde{\mathcal{P}}_g\left(k,\mu\right)\tilde{\mathcal{P}}_{g'}\left(k,\mu\right)\right].\end{aligned} \tag{5.17}$$

Combining the symmetric and anti-symmetric parts, we defined the the covariance matrix of as

$$\Gamma\left(k,\mu\right) = \begin{bmatrix}\mathrm{Cov}\left[\mathrm{Re}\left[\mathcal{P}_{gg'}(k,\mu)\right],\mathrm{Re}\left[\mathcal{P}_{gg'}(k',\mu')\right]\right] & \mathrm{Cov}\left[\mathrm{Re}\left[\mathcal{P}_{gg'}(k,\mu)\right],\mathrm{Im}\left[\mathcal{P}_{gg'}(k',\mu')\right]\right] \\ \mathrm{Cov}\left[\mathrm{Im}\left[\mathcal{P}_{gg'}(k,\mu)\right],\mathrm{Re}\left[\mathcal{P}_{gg'}(k',\mu')\right]\right] & \mathrm{Cov}\left[\mathrm{Im}\left[\mathcal{P}_{gg'}(k,\mu)\right],\mathrm{Im}\left[\mathcal{P}_{gg'}(k',\mu')\right]\right]\end{bmatrix} \tag{5.18}$$

and for the multipoles [18],

$$\Gamma_{\ell_1,\ell_2}(k) = \frac{(2\ell_1+1)(2\ell_2+1)}{4}\int_{-1}^{1} \mathrm{d}\mu\, \mathcal{L}_{\ell_1}(\mu)\, \mathcal{L}_{\ell_2}(\mu) \times \\ \times \begin{cases} \mathrm{Cov}\Big[\,\mathrm{Re}\left[\mathcal{P}_{gg'}(k,\mu)\right], \mathrm{Re}\left[\mathcal{P}_{gg'}(k',\mu')\right]\Big], & \ell_1 \text{ and } \ell_2 \text{ even}, \\ \mathrm{Cov}\Big[\,\mathrm{Im}\left[\mathcal{P}_{gg'}(k,\mu)\right], \mathrm{Im}\left[\mathcal{P}_{gg'}(k',\mu')\right]\Big], & \ell_1 \text{ and } \ell_2 \text{odd}, \\ \mathrm{Cov}\Big[\,\mathrm{Re}\left[\mathcal{P}_{gg'}(k,\mu)\right], \mathrm{Im}\left[\mathcal{P}_{gg'}(k',\mu')\right]\Big], & \text{otherwise}. \end{cases} \tag{5.19}$$

where, the mixed covariance reads

$$\mathrm{Cov}\left[\mathrm{Re}\left[\mathcal{P}_{gg'}(k,\mu)\right], \mathrm{Im}\left[\mathcal{P}_{gg'}(k',\mu')\right]\right] = \frac{1}{N_{\boldsymbol{k}}}\,\mathrm{Re}\left[\mathcal{P}_{gg'}(k,\mu)\right]\mathrm{Im}\left[\mathcal{P}_{gg'}(k,\mu)\right]. \tag{5.20}$$

5.3.2 Degeneracies Analysis

We began by testing the imaginary estimator and its dipole individually for $\boldsymbol{\theta}$. However, when performing the calculation, we found that the resulting matrix was not invertible, indicating the presence of degeneracies among our parameters.

To identify possible degeneracies, it is helpful to construct an intuitive framework that allows us to reason directly about the data vector. A natural choice is to base this reasoning on the derivatives of the observables with respect to the parameters. Concretely, let us define J as the matrix whose columns are the vectorized derivatives:

$$J = \Big[\,\partial\mathbf{P}/\partial\theta_1,\ \partial\mathbf{P}/\partial\theta_2,\ \ldots\,\Big].$$

It can then be formally shown that the null space of the Fisher matrix,

$$F = J^T\,\Gamma^{-1}\,J,$$

coincides with the null space of J itself. In other words, any exact linear dependence among the derivatives directly translates into a degeneracy in the Fisher matrix. This provides a rigorous justification for using the derivatives of the data vector as a guide to identify degeneracies.

With this insight, our working hypothesis was that this degeneracy involved the α parameters and A_D. The reasoning behind this proposal is that, upon examining the

structure of the derivatives of the observables with respect to the parameters, we find that the data-vector derivatives satisfy

$$\frac{\partial \mathbf{P}}{\partial A_D} \propto \frac{\partial \mathbf{P}}{\partial \alpha}, \tag{5.21}$$

since A_D acts as a global rescaling of the Doppler contribution already controlled by the α_g*.

One possible strategy to prove this degeneracy is to separate in two different sets

$$\boldsymbol{\theta}_1 = \left\{ \alpha_{g,1}, \alpha_{g',1}, \alpha_{g,2}, \alpha_{g',2}, \alpha_{g,3}, \alpha_{g',3} \right\} \tag{5.22}$$

and

$$\boldsymbol{\theta}_2 = \{A_D\}\,. \tag{5.23}$$

When testing this separation, we found that for the imaginary estimator the degeneracy disappeared, whereas for the dipole it persisted within the set $\boldsymbol{\theta}_1$. This confirmed our hypothesis, while also showing that the degeneracy with A_D is not the only one present in the dipole.

To better understand the nature of this second degeneracy, we examined the parameter derivatives by

$$\frac{\partial \mathbf{P}}{\partial \alpha_g} = \frac{\partial \mathbf{P}}{\partial \alpha_{g'}}. \tag{5.24}$$

For the imaginary component, this condition yields

$$b_{g'} = -(b_g + 2f\mu^2)$$

whereas for the dipole we obtain

$$b_{g'} = -\frac{1}{5}(5b_g + 6f).$$

*Additional intuition supports this interpretation. For instance, one can explicitly verify that $\frac{\partial \mathbf{P}}{\partial A_D} = \frac{\partial \mathbf{P}}{\partial \alpha_g} + \frac{\partial \mathbf{P}}{\partial \alpha_{g'}}$, which again reveals the degeneracy.

We note that the dipole relation is constant at each redshift, implying that the two derivatives are related by a simple rescaling, thereby maintaining the degeneracy. In contrast, the imaginary component depends on μ, a variable quantity, meaning that the relation cannot be reduced to a mere rescaling and the degeneracy is therefore broken.

Since the factor responsible for breaking the degeneracy is precisely the μ-dependence, we considered combining the octopole with the dipole. The reasoning behind this choice is that by including both multipoles, we effectively distribute the μ-dependence across different angular modes. In doing so, the data vector captures the full angular information encoded in μ, rather than restricting it to a single projection, thereby enhancing the ability to disentangle parameter degeneracies. The covariance matrix in this case is the same as in Eq. (5.8), but here we consider $\ell_1 \neq \ell_2$ as in Eq. (4.38) and allow them to take values of 1 or 3. The computational calculations confirmed the breaking of the degeneracy, allowing us to obtain estimates for the parameters in $\boldsymbol{\theta}_1$. However, the original degeneracy persisted.

We now turn to the real estimator. The calculations showed us that for the full parameter set $\boldsymbol{\theta}$, the test unsurprisingly failed, as expected, since it is also subject to the same condition given in Eq. (5.21). We then performed the analysis separately for the parameter subsets $\boldsymbol{\theta}_1$ and $\boldsymbol{\theta}_2$. While the latter worked, the former once again exhibited degeneracies. Applying Eq. (5.24), we obtain

$$\alpha_g = \alpha_{g'}.$$

This confirms the presence of degeneracies analogous to those found for the dipole. In this case, we expect the multipoles to retain the degeneracy, either individually or in combination, since they merely reveal the angular dependence of the real part. Finally, we confirmed computationally that the real multipoles indeed display this same degeneracy.

To see if we could somehow mitigate this degeneracy between the α parameters and A_D, as we did previously, we used the mixed data vector with real and imaginary estimator and a vector of its multipoles. The computational analysis showed that the linear dependence among the α parameters originating from the real estimator does not persist once imaginary-part observables are included. This demonstrates that the imaginary estimator contributes independent information on the α's, thereby rendering the Fisher matrix non-degenerate with respect to these parameters. On the other hand, the α–A_D degeneracy remained as a fundamental limitation. Neither the real nor the imaginary sector, nor their combination or the combination of their multipoles, provides sufficient

information to lift this degeneracy. This also implies that attempting the same analysis for the full cross-power spectrum would not succeed, since the real and imaginary parts together already contain the complete information, which we were able to confirm while working on Appendix C. Furthermore, the multipoles of the cross-power spectrum exhibited the same degeneracies as those of the symmetric and anti-symmetric estimators. A plausible explanation is that all terms involving either α or A_D can be traced back to the same underlying contribution, δ_α in Eq. (5.15), which naturally favours the persistence of this degeneracy.

Finally, in order to explore other potential degeneracies and possible breaking mechanisms, we performed additional tests considering all combinations of the seven parameters. We began by testing each parameter individually and, as expected from the previous analysis, no degeneracies were observed. When moving to two-parameter combinations, we identified two noteworthy results. First, if the parameters included different types of α (or even the same type) but evaluated at different redshifts, the degeneracy previously seen in the real part for α's disappeared. This behaviour was further reinforced by the fact that, when using only the real part but considering α at three different redshifts, no degeneracy reappeared. A natural explanation is that α's at different redshifts do not interact, leading to a block-diagonal Fisher matrix, which in turn implies that the parameter equations are redshift-dependent. Consequently, an analysis with more redshift points would not change the degeneracy structure among the parameters. This motivated us to verify the previously identified degeneracies for a single redshift bin, and we confirmed that they remain unchanged whether one considers one or three bins. The second result is that, when using only one α together with A_D, no degeneracy was present. This breaking persisted, when including the imaginary part, even when combining up to six parameters, provided that one of them was A_D and the others were α's (with one excluded). We also verified that this behaviour holds for a single redshift bin, confirming that it is not simply due to the fact that A_D is defined as the sum of three redshift-dependent terms. This suggests that A_D replaces the missing α by acting as a rescaling, $A_D \times \alpha \to \alpha'$, which then behaves like a new redefined α. The fact that this persists even when including up to five of the six α's indicates that, although completing two sets of equations (two set of α's plus A_D). We ultimately restricted our analysis to the parameter sets $\boldsymbol{\theta}_1$ and $\boldsymbol{\theta}_2$, since in practice one would either aim to constrain all α's across redshifts or to determine the amplitude A_D, but not replace the search for one of the α's by A_D.

5.3.3 Relative Errors Analysis

The previous subsection allowed us to constrain our parameter set choice to two alternatives: $\boldsymbol{\theta}_1$, defined in Eq. (5.22), and $\boldsymbol{\theta}_2$, defined in Eq. (5.23). For the latter, all possible combinations of observables may be employed without restriction. For the former, however, only multipoles of the cross power spectrum, the imaginary estimator, the multipoles of the imaginary estimator (jointly), the combination of the imaginary and real estimators, or the combination of both their multipoles can be consistently used.

To quantify the expected precision with which the parameters can be constrained, we define the relative error associated with a parameter θ_i as*

$$\text{relative error} = \frac{\sigma_{\theta_i}}{|\theta_i|}, \tag{5.25}$$

where σ_{θ_i} represents the forecasted uncertainty. This dimensionless quantity provides a natural measure of parameter sensitivity, as it directly reflects the accuracy relative to the physical scale of the parameter itself. In particular, it allows a straightforward comparison between different parameters, regardless of their units or magnitudes.

As a comparative benchmark to evaluate whether our methods provide an improvement over those reported in the literature, while also verifying their consistency with established trends, we adopt [16] as a reference. Using the same methodology for our sample, we obtained the results presented in Table C.1.

α Parameter Set

The analysis of the α parameter set yields the relative errors reported in Table 5.2.

Observables	$\alpha_{g,1}$	$\alpha_{g',1}$	$\alpha_{g,2}$	$\alpha_{g',2}$	$\alpha_{g,3}$	$\alpha_{g',3}$
$\mathcal{P}_{gg'}$	139.8	21.51	33.23	173.1	32.02	58.35
$\mathcal{P}_0, \mathcal{P}_1, \mathcal{P}_2, \mathcal{P}_3, \mathcal{P}_4$	99.20	15.27	23.76	123.8	22.30	40.67
$\mathcal{P}^I$	2.932	0.449	0.053	0.275	0.021	0.037
$\mathcal{P}^I_1, \mathcal{P}^I_3$	3.609	0.555	0.063	0.327	0.023	0.042
$\mathcal{P}^R, \mathcal{P}^I$	2.092	0.320	0.041	0.212	0.021	0.037
$\mathcal{P}^R_0, \mathcal{P}^I_1, \mathcal{P}^R_2, \mathcal{P}^I_3, \mathcal{P}^R_4$	2.571	0.395	0.048	0.248	0.023	0.041

TABLE 5.2: Relative errors for α_g and $\alpha_{g'}$ at the three mean redshifts for the possible data vectors.

*Relative errors are computed with respect to the absolute value of the parameters, since some of them may take both positive and negative values, as shown in Table 5.1.

On the one hand, we find that decomposing the cross-power spectrum into symmetric and anti-symmetric estimators yields improved relative error values for the α parameters compared to those derived from the full cross-power spectrum, demonstrating that our approach provides a more effective tool. However, not all parameters achieve precise detection (< 0.1)*, indicating that further development of optimized data vectors is necessary to achieve tighter constraints on the α parameters.

On the other hand, when comparing multipoles to their full angular counterparts, we observe that while the multipoles generally follow the same scaling, they perform somewhat less effectively, resulting in relative errors up to 60% higher than those obtained from the full angular analysis, which is a deviation larger than what has been reported in the literature [18]. An exception was found when converting the cross-power spectrum to its multipoles, which in one case produced a smaller relative error. A detailed discussion of the multipoles results is provided later, after evaluating the relative errors for A_D.

Furthermore, when comparing values obtained exclusively from the imaginary estimator with those derived from the combined data vector, we find that the latter yields smaller relative errors. This outcome is expected, as extending the data vector by including additional estimators can only improve or, at worst, leave unchanged our ability to infer the underlying parameters†.

A_D Parameter Set

For the parameter set $\boldsymbol{\theta}_2$, we tested the same data vectors as in the previous analysis, while additionally including the anti-symmetric estimator and its multipoles. The resulting analysis of the A_D parameter yields the relative errors presented in Table 5.3.

Once again, we observe that the anti-symmetric estimator, as well as the combined anti-symmetric and symmetric data vector, yield better results than the standard cross-power spectrum. Moreover, the relative errors obtained are well below 0.1, placing them within the range considered to constitute a strong constraint. However, a decrease in relative errors when transitioning from the full angular spectrum to its multipoles, which was previously an exception, has now become the general rule, with the multipoles improving the relative errors across all cases, something that should not happen.

*In general, values below the 10% level (< 0.1) are regarded as strong constraints in cosmological parameter estimation [29].

†This trend is evident when comparing [16] and [15]. In the former, the analysis relies exclusively on the cross-power spectrum, resulting in larger marginal errors. In contrast, the latter employs a multi-tracer approach (more observables), combining cross and auto power spectra, thereby achieving significantly improved constraints.

Observables	Relative Error
$\mathcal{P}_{gg'}$	6.90×10^{-1}
$\mathcal{P}_0, \mathcal{P}_1, \mathcal{P}_2, \mathcal{P}_3, \mathcal{P}_4$	4.89×10^{-1}
$\mathcal{P}^I$	8.25×10^{-4}
$\mathcal{P}^I_1, \mathcal{P}^I_3$	7.01×10^{-4}
$\mathcal{P}^R$	4.01×10^{1}
$\mathcal{P}^R_0, \mathcal{P}^R_2, \mathcal{P}^R_4$	2.85×10^{1}
$\mathcal{P}^R, \mathcal{P}^I$	7.23×10^{-4}
$\mathcal{P}^R_0, \mathcal{P}^I_1, \mathcal{P}^R_2, \mathcal{P}^I_3, \mathcal{P}^R_4$	6.11×10^{-4}

TABLE 5.3: Relative errors for α_g and $\alpha_{g'}$ at the three mean redshifts for the possible data vectors.

Discussion

To conclude, there are two points that deserve further discussion: first, why treating the real and imaginary parts of the cross-spectrum as separate estimators leads to tighter constraints than using the full cross-power spectrum, as done in [16], taken here as our reference, despite both approaches being expected to encode the same information; second, why the transition from the full angular spectrum to its multipoles produces results that differ from theoretical expectations.

As for the first point, let us illustrate why treating the real and imaginary parts separately may improve constraints. Consider the Portuguese saying, "*cada macaco no seu galho*", which translates directly as "each monkey on its branch". Imagine a tree with multiple branches, where each branch could host different types of monkeys, say, two distinct species. If one were to perform a statistical analysis without distinguishing between branches, some confusion could arise due to the presence of multiple species. Now, imagine instead that there are two separate trees, each hosting a different species. In this scenario, it becomes much easier to analyze each species individually, rather than analyzing all species together on a single tree. In our context, each species of monkey represents either the real or the imaginary part of the cross-spectrum. By isolating the imaginary part, which captures the Doppler contribution, the covariance of the power spectrum no longer depends directly on the real part, dominated by linear bias and redshift-space distortions. Consequently, it becomes easier to extract insights specifically related to the Doppler effect than when considering the full expression, where the covariance still couples both components. This finding is consistent with our SNR analysis and is now further

confirmed in the parameter-space study. It highlights that the improvement does not necessarily arise from additional information, but rather from how the information is framed. Furthermore, in the real part, we still account for both the Doppler contribution and the dominant terms from linear bias and redshift-space distortions. In this context, if we could possible separate these contributions further, it would make the analysis of Doppler parameters even more straightforward, potentially yielding even tighter constraints on the Doppler effect than in our current approach.

Regarding the second point, the results obtained from the multipoles have, in most cases, shown better relative errors than those from the full angular spectrum. Yet we found no evidence of such behavior in the literature [18, 30], and from a theoretical standpoint this outcome appears difficult to justify. As Eq. (4.36) shows, transforming into multipoles is a linear operation in which information should inevitably be lost due to averaging over μ. Consequently, the Fisher matrix should at best retain the same information content, not improve upon it. One might argue, by analogy, that just as separating the real and imaginary parts of the cross-power spectrum allows us to isolate the Doppler effect and obtain tighter constraints, a similar mechanism could be at play for the multipoles, since they also isolate the Doppler contribution. However, this interpretation lacks consistency: the improvement is not observed for all test parameters, whereas in the case of the antisymmetric estimator we consistently obtained stronger constraints for the α parameters with respect to multipoles but not for A_D. Another possible explanation is that the covariance matrices for the multipoles have not been properly constructed. For instance, if we compare the SNR of $\mathcal{P}^I$ (Fig. 5.2) with that of $\mathcal{P}^I_1$ and $\mathcal{P}^I_3$ (Fig. 5.3), we find that the dipole has a higher SNR than $\mathcal{P}^I$, whereas it should be lower [18]. This suggests that issues in the construction of the multipole covariance could be driving the discrepancy, and thus require careful reassessment. However, even this cannot fully explain the inconsistency: if the covariance construction systematically favored multipoles over their full angular counterparts, then improvements should appear across all estimators and parameters, which is not the case. The fact that the multipole transformation yields inconsistent results prevents us from drawing firm conclusions. Instead, our findings point to the need for a more rigorous investigation before reliable inferences can be made.

Chapter 6

Conclusion

In this dissertation we have investigated the detectability of the relativistic Doppler effect in galaxy clustering and its role as a probe of gravity on cosmological scales. To achieve this goal, we first introduce the theoretical foundation required to describe the relativistic Doppler contribution in the observed density field of galaxies and in the corresponding power spectra. Starting from the homogeneous and isotropic background of the ΛCDM cosmological model, we introduced the impact of peculiar velocities on galaxy redshifts, extending the Newtonian treatment to the relativistic regime. In this context, we showed that the relativistic Doppler effect introduces an imaginary component in Fourier space, which is suppressed in auto power spectra but preserved in cross power spectra between different galaxy populations. This property establishes cross-correlations as promising estimator for isolating relativistic contributions.

Building on this, we developed a theoretical framework that enables the construction of an antisymmetric (imaginary) estimator from the cross power spectrum, which isolates its imaginary part and thus the Doppler effect. In parallel, we applied a Legendre multipole expansion of the cross power spectrum as a less data-demanding approach to approximate the information contained in the full angular spectrum, since the odd multipoles also isolate the Doppler contribution.

For the second approach, tests based on signal-to-noise and Fisher forecast analyses did not yield consistent results, as the relative errors compared with those from the full power spectrum fluctuated between being larger or smaller without any clear justification. Consequently, no robust conclusions could be drawn, and further investigation is required.

On the other hand, for the antisymmetric estimator we derived a new covariance matrix. The only formulation previously available in the literature considered a single Fourier mode of k [17], effectively restricting the analysis to individual modes and neglecting the statistical averaging over the ensemble of modes within the survey volume. Our new derivation revealed that, for this estimator, the only source of statistical uncertainty is cosmic variance. Thus, the signal-to-noise ratio is directly determined by it. We then investigated how this result affects parameter constraints within a Fisher forecast analysis. The forecasts were performed for a DESI-like Bright Galaxy Sample at low redshift, providing a realistic configuration for upcoming spectroscopic surveys. We first considered a complete set of relativistic Doppler amplitudes α_g and $\alpha_{g'}$, as well as the overall amplitude $A_D = 1$. The Fisher analysis revealed degeneracies between the α's and A_D, which required separating the parameters into two sets.

Subsequently, we tested the parameter constraints for the imaginary estimator as well as for the combination of the antisymmetric and symmetric (real part) estimators of the cross power spectrum. In both cases, and particularly for the combined estimator, we obtained significantly smaller relative errors than with the standard cross power spectrum. For the Doppler amplitudes α, the relative errors typically ranged between approximately 32% and 2%, with one exception where the result yielded an anomalously large relative error. For the overall amplitude A_D, the constraints achieved an unprecedented precision of order 7×10^{-4}, representing a substantial improvement over previous results in the literature, which reported values around 7×10^{-3} [15, 16].

These results demonstrate that the relativistic Doppler effect, although subdominant, can be realistically constrained with forthcoming large-scale galaxy surveys. The combination of the real and imaginary parts emerges as a powerful observable capable of isolating relativistic contributions that would otherwise remain hidden.

That said, these tests were carried out only for a single sample, which may not be sufficient to draw definitive conclusions. A more robust validation would require testing different samples, or ideally using real data from surveys such as *Euclid*, DESI, and their cross-correlations with SKAO [20, 31]. This is necessary, as we cannot rely solely on sample-based results, and additional information would strengthen (or possibly challenge) the conclusions we have reached. Nevertheless, even if the results turn out slightly weaker with real data, the strategy of isolating the imaginary part of the observable through its antisymmetry appears robust enough to retain significant constraining power.

Another possible extension would be to include a larger set of parameters in the analysis. Our focus here was exclusively on testing the detectability of the Doppler contribution, so we restricted ourselves to the parameters listed above. However, one could attempt to incorporate additional parameters such as galaxy biases, the growth rate, or even the Hubble parameter. Doing so through the imaginary part could potentially lead to new insights about the Universe. This also extends beyond Doppler alone, since other relativistic effects with imaginary contributions, such as gravitational redshift [17], could be tested within the same framework.

Finally, a further avenue would be to explore the use of the multitracer technique, as in [15], which has been shown to yield stronger constraints than relying solely on the information from the cross power spectrum [16].

Appendix A

On the Derivation of the Discrete Fourier Power Spectrum and Poisson Noise

The statistical treatment of galaxy surveys often relies on the assumption that galaxies constitute a Poisson sampling of the underlying continuous density field. This approximation assumes that galaxy positions are independent random events drawn from such a field, leading to the characteristic property of Poisson statistics: the variance of the number of galaxies within a given volume is equal to its mean. As a consequence, the shot noise contribution to the galaxy power spectrum is scale-independent and takes the simple form of the inverse mean number density of galaxies.

This assumption is particularly convenient in forecasting analyses, where the primary goal is to estimate the constraining power of future surveys. In such contexts, the detailed modeling of galaxy bias, clustering, redshift uncertainties, or survey selection effects is either unavailable or still under development. The Poisson model therefore provides a conservative and analytically tractable baseline for noise, allowing for straightforward propagation of uncertainties into the power spectrum or cosmological parameter forecasts. While more sophisticated descriptions (e.g., based on halo occupation distributions, exclusion effects, or realistic survey geometries) can capture deviations from Poisson statistics, these are generally incorporated only at later stages of analysis, once observational data or advanced simulations become available.

To describe this more formally, we need to expand our consideration of Section 4.4 [32].

Consider our survey volume grid as cells of size V_i. In each cell i, the number of galaxies is then modeled as a Poisson random variable with mean $\bar{n}_{g,i}V_i$. Ignoring the Fourier modes for the moment, this consideration allows us to discretize Eq. (4.21) as

$$\delta_{g,\boldsymbol{k}} = \frac{1}{\bar{n}_g}\sum_i n_{g,i}e^{i\boldsymbol{k}\cdot\mathbf{r}_i} - \delta^K_{\boldsymbol{k},0} \tag{A.1}$$

where δ^K is the Kronecker delta, and the discrete limit arises from partitioning the volume into sufficiently small cells dV_i such that each contains either zero or one galaxy, $n_i \in 0, 1$. A hallmark of the Poisson distribution then appears: $\langle n_{g,i}\rangle = \langle n^2_{g,i}\rangle$.

Using the ensemble averages

$$\left\langle n_{g,i}\right\rangle = \bar{n}_g dV_i \quad \text{and} \tag{A.2}$$

$$\left\langle n_{g,i}n_{g,j}\right\rangle_{i\neq j} = \bar{n}^2_g dV_i dV_j\left[1 + \left\langle \delta_g\left(\mathbf{x}_i\right)\delta_g\left(\mathbf{x}_j\right)\right\rangle\right], \tag{A.3}$$

we can calculate the discrete ensemble average $\left\langle \delta_{g,\boldsymbol{k}_1}\delta^*_{g,\boldsymbol{k}_2}\right\rangle$, which yields

$$\begin{aligned}
\left\langle \delta_{g,\boldsymbol{k}_1}\delta^*_{g,\boldsymbol{k}_2}\right\rangle &= \left\langle \frac{1}{\bar{n}^2_g}\sum_{ij} n_{g,i}n_{g,j}e^{i\boldsymbol{k}_1\cdot\mathbf{r}_i}e^{-i\boldsymbol{k}_2\cdot\mathbf{r}_j} - \frac{1}{\bar{n}_g}\sum_i n_{g,i}e^{i\boldsymbol{k}_1\cdot\mathbf{r}_i}\delta^K_{\boldsymbol{k}_2,0}\right. \\
&\quad \left. -\frac{1}{\bar{n}_g}\sum_j n_{g,j}e^{i\boldsymbol{k}_2\cdot\mathbf{r}_j}\delta^K_{\boldsymbol{k}_1,0} + \delta^K_{\boldsymbol{k}_1,0}\delta^K_{\boldsymbol{k}_2,0}\right\rangle \\
&= \frac{1}{\bar{n}^2_g}\sum_{ij}\left\langle n_{g,i}n_{g,j}\right\rangle e^{i\boldsymbol{k}_1\cdot\mathbf{r}_i}e^{-i\boldsymbol{k}_2\cdot\mathbf{r}_j} - \delta^K_{\boldsymbol{k}_1,0}\delta^K_{\boldsymbol{k}_2,0} \\
&= \frac{1}{\bar{n}^2_g}\sum_{i\neq j}\left\langle n_{g,i}n_{g,j}\right\rangle e^{i\boldsymbol{k}_1\cdot\mathbf{r}_i}e^{-i\boldsymbol{k}_2\cdot\mathbf{r}_j} + \frac{1}{\bar{n}^2_g}\sum_i\left\langle n_{g,i}\right\rangle e^{i\mathbf{r}_i\cdot(\boldsymbol{k}_1-\boldsymbol{k}_2)} - \delta^K_{\boldsymbol{k}_1,0}\delta^K_{\boldsymbol{k}_2,0} \\
&= \left\langle \delta_g\left(\boldsymbol{k}_1\right)\delta^*_g\left(\boldsymbol{k}_2\right)\right\rangle + \frac{\delta^K_{\boldsymbol{k}_1,\boldsymbol{k}_2}}{\bar{n}_g},
\end{aligned} \tag{A.4}$$

where the last step comes from taking the continuum limit to retrieve the initial expected value, and assumes $\boldsymbol{k}_1$ or $\boldsymbol{k}_2 \neq 0$. We can rewrite this as

$$\begin{aligned}
\hat{\mathcal{P}}_g(k_i) = \left\langle \delta_g\left(\boldsymbol{k}_i\right)\delta^*_g\left(\boldsymbol{k}_i\right)\right\rangle &= \frac{1}{N_{k,i}}\sum_{\boldsymbol{k}}^{\left||\boldsymbol{k}|-k_i\right|<\Delta k/2}\left\langle \delta_{g,\boldsymbol{k}}\delta^*_{g,\boldsymbol{k}}\right\rangle - \frac{1}{\bar{n}_g} \\
&= \frac{1}{N_{k,i}}\sum_{\boldsymbol{k}}^{\left||\boldsymbol{k}|-k_i\right|<\Delta k/2}\left\langle\left|\delta_{g,\boldsymbol{k}}\right|^2\right\rangle - \mathcal{P}^N_g,
\end{aligned} \tag{A.5}$$

which corresponds to Eq. (4.26).

This result is telling us two things. First, for a given distribution of galaxies, the power spectrum will have an added noise which is correspondent to the inverse global number density of those galaxies. This reflects the fact that increasing the number density of tracers improves the fidelity with which the continuous field is reconstructed. In the idealized limit $\bar{n} \to \infty$, the Poisson shot noise vanishes and the continuous field is perfectly recovered.

Secondly, the Kronecker delta enforces that shot noise contributes only to the diagonal components in Fourier space. In other words, Poisson fluctuations do not correlate distinct Fourier modes. Conceptually, the shot noise can be thought of as the artificial "self-correlation" of a galaxy with itself. This effect does not carry cosmological information and must be subtracted from the measured power spectrum.

Appendix B

Detailed Derivation of the Covariance of the Real, Imaginary, and Mixed Components of the Cross Power Spectrum

In the main text, we omitted the proofs of Eqs. (5.5), (5.16), and (5.20) for reasons of length. Nevertheless, their derivation is essential to our analysis, particularly Eq. (5.5), which constitutes one of our central results and cannot be disregarded. For this reason, we devote this appendix to presenting the full derivation, beginning with the imaginary part and subsequently extending the argument to the remaining cases.

We start with the imaginary part, whose covariance with itself is defined as

$$\begin{aligned}
&\mathrm{Cov}[\hat{\mathcal{P}}^I_{gg'}(k,\mu)\,\hat{\mathcal{P}}^I_{gg'}(k',\mu')] = \left\langle \hat{\mathcal{P}}^I_{gg'}(k,\mu)\,\hat{\mathcal{P}}^I_{gg'}(k',\mu') \right\rangle - \left\langle \hat{\mathcal{P}}^I_{gg'}(k,\mu) \right\rangle \left\langle \hat{\mathcal{P}}^I_{gg'}(k',\mu') \right\rangle \\
&= \frac{1}{N_k} \sum_{\boldsymbol{k}} \frac{1}{N_{k'}} \sum_{\boldsymbol{k}'} \left(\left\langle \left[\mathrm{Im}\left(\delta_{g,\boldsymbol{k}}\, \delta^*_{g',\boldsymbol{k}} \right) \right] \left[\mathrm{Im}\left(\delta_{g,\boldsymbol{k}'}\, \delta^*_{g',\boldsymbol{k}'} \right) \right] \right\rangle \right. \\
&\left. - \left\langle \left[\mathrm{Im}\left(\delta_{g,\boldsymbol{k}}\, \delta^*_{g',\boldsymbol{k}} \right) \right] \right\rangle \left\langle \left[\mathrm{Im}\left(\delta_{g,\boldsymbol{k}'}\, \delta^*_{g',\boldsymbol{k}'} \right) \right] \right\rangle \right)
\end{aligned} \tag{B.1}$$

Expanding the first expectation value, we obtain

$$\left\langle \left[\mathrm{Im}\left(\delta_{g,k}\,\delta^*_{g',k}\right)\right]\left[\mathrm{Im}\left(\delta_{g,k'}\,\delta^*_{g',k'}\right)\right]\right\rangle = \left\langle \left(\frac{\delta_{g,k}\,\delta^*_{g',k}-\delta_{g',k}\,\delta^*_{g,k}}{2i}\right)\times \right.$$
$$\left.\times\left(\frac{\delta_{g,k'}\,\delta^*_{g',k}-\delta_{g',k'}\,\delta^*_{g,k'}}{2i}\right)\right\rangle =$$
$$=-\frac{1}{4}\left(\left\langle \delta_{g,k}\,\delta^*_{g',k}\,\delta_{g,k'}\delta^*_{g',k'}\right\rangle-\left\langle \delta_{g,k}\,\delta^*_{g',k}\,\delta_{g',k'}\,\delta^*_{g,k'}\right\rangle\right.$$
$$\left.-\left\langle \delta_{g',k}\,\delta^*_{g,k}\,\delta_{g,k'}\,\delta^*_{g',k'}\right\rangle+\left\langle \delta_{g',k}\,\delta^*_{g,k}\,\delta_{g',k'}\,\delta^*_{g,k'}\right\rangle\right). \tag{B.2}$$

Each of these four-point functions can be expanded using Wick's theorem. For instance, the first term reads

$$\left\langle \delta_{g,k}\,\delta^*_{g',k}\,\delta_{g,k'}\,\delta^*_{g',k'}\right\rangle=\left\langle \delta_{g,k}\,\delta^*_{g',k}\right\rangle\left\langle \delta_{g,k'}\,\delta^*_{g',k'}\right\rangle$$
$$+\left\langle \delta_{g,k}\,\delta_{g,k'}\right\rangle\left\langle \delta^*_{g',k}\,\delta^*_{g',k'}\right\rangle+\left\langle \delta_{g,k}\,\delta^*_{g',k'}\right\rangle\left\langle \delta^*_{g',k}\,\delta_{g,k'}\right\rangle$$
$$=\mathcal{P}_{gg'}\left(k,\mu\right)\mathcal{P}_{gg'}\left(k',\mu'\right)+\delta_{\boldsymbol{k},-\boldsymbol{k}'}\tilde{\mathcal{P}}_g\left(k,\mu\right)\tilde{\mathcal{P}}_{g'}\left(k,\mu\right)+\delta_{\boldsymbol{k},\boldsymbol{k}'}\left(\mathcal{P}_{gg'}\left(k,\mu\right)\right)^2. \tag{B.3}$$

Proceeding analogously, the remaining three terms yield

$$\left\langle \delta_{g,k}\,\delta^*_{g',k}\,\delta_{g',k'}\,\delta^*_{g,k'}\right\rangle=\mathcal{P}_{gg'}\left(k,\mu\right)\mathcal{P}_{g'g}\left(k',\mu'\right)$$
$$+\,\delta_{\boldsymbol{k},\boldsymbol{k}'}\tilde{\mathcal{P}}_g\left(k,\mu\right)\tilde{\mathcal{P}}_{g'}\left(k,\mu\right)+\delta_{\boldsymbol{k},-\boldsymbol{k}'}\mathcal{P}_{gg'}\left(k,\mu\right)\mathcal{P}_{g'g}(k,\mu), \tag{B.4}$$

$$\left\langle \delta_{g',k}\,\delta^*_{g,k}\,\delta_{g,k'}\,\delta^*_{g',k'}\right\rangle=\mathcal{P}_{g'g}\left(k,\mu\right)\mathcal{P}_{gg'}\left(k',\mu'\right)$$
$$+\,\delta_{\boldsymbol{k},\boldsymbol{k}'}\tilde{\mathcal{P}}_g\left(k,\mu\right)\tilde{\mathcal{P}}_{g'}\left(k,\mu\right)+\delta_{\boldsymbol{k},-\boldsymbol{k}'}\mathcal{P}_{g'g}\left(k,\mu\right)\mathcal{P}_{gg'}\left(k,\mu\right), \tag{B.5}$$

and

$$\left\langle \delta_{g'}(\boldsymbol{k})\,\delta^*_g(\boldsymbol{k})\,\delta_{g'}(\boldsymbol{k}')\,\delta^*_g(\boldsymbol{k}')\right\rangle=\mathcal{P}_{g'g}\left(k,\mu\right)\mathcal{P}_{g'g}\left(k',\mu'\right)$$
$$+\,\delta_{\boldsymbol{k},-\boldsymbol{k}'}\tilde{\mathcal{P}}_g\left(k,\mu\right)\tilde{\mathcal{P}}_{g'}\left(k,\mu\right)+\delta_{\boldsymbol{k},\boldsymbol{k}'}\left(\mathcal{P}_{g'g}\left(k,\mu\right)\right)^2. \tag{B.6}$$

Adding together the leading terms of Eqs. (B.3)–(B.6) with the second term in Eq. (B.1), we see that they cancel. Furthermore, when summing over all possible $\boldsymbol{k}$, i.e. including the cases $\boldsymbol{k}=\boldsymbol{k}'$ or $\boldsymbol{k}=-\boldsymbol{k}'$, the symmetry between the second Wick terms ensures their

cancellation as well. Hence, after accounting for the summation over modes, Eq. (B.1) reduces to

$$\begin{aligned}
&\mathrm{Cov}[\hat{\mathcal{P}}^I_{gg'}(k,\mu)\,\hat{\mathcal{P}}^I_{gg'}(k',\mu')] = \left\langle \hat{\mathcal{P}}^I_{gg'}(k,\mu)\,\hat{\mathcal{P}}^I_{gg'}(k',\mu')\right\rangle - \left\langle \hat{\mathcal{P}}^I_{gg'}(k,\mu)\right\rangle \left\langle \hat{\mathcal{P}}^I_{gg'}(k',\mu')\right\rangle \\
&= -\frac{1}{4N_k}\left(\left(\mathcal{P}_{gg'}(k,\mu)\right)^2 - 2\mathcal{P}_{gg'}(k,\mu)\,\mathcal{P}_{g'g}(k,\mu) + \left(\mathcal{P}_{g'g}(k,\mu)\right)^2\right) \\
&= -\frac{1}{4N_k}\left(\mathcal{P}_{gg'}(k,\mu) - \mathcal{P}_{g'g}(k,\mu)\right)^2 \\
&= \frac{1}{N_k}\left(\mathcal{P}^I_{gg'}(k,\mu)\right)^2 .
\end{aligned} \tag{B.7}$$

The derivation for the real part proceeds identically, with the only difference being the change of sign in the middle terms of Eq. (B.2) (from negative to positive). This leads that the noise terms ($\tilde{\mathcal{P}}$) aren't symmetry, and after simplification the result is

$$\begin{aligned}
&\mathrm{Cov}[\hat{\mathcal{P}}^R_{gg'}(k,\mu),\hat{\mathcal{P}}^R_{gg'}(k',\mu')] = \left\langle \hat{\mathcal{P}}^R_{gg'}(k,\mu)\,\hat{\mathcal{P}}^R_{gg'}(k',\mu')\right\rangle - \left\langle \hat{\mathcal{P}}^R_{gg'}(k,\mu)\right\rangle \left\langle \hat{\mathcal{P}}^R_{gg'}(k',\mu')\right\rangle \\
&= \frac{1}{4N_k}\left(\left(\mathcal{P}_{gg'}(k,\mu)\right)^2 + 2\mathcal{P}_{gg'}(k,\mu)\,\mathcal{P}_{g'g}(k,\mu) + \left(\mathcal{P}_{g'g}(k,\mu)\right)^2 + 4\tilde{\mathcal{P}}_g(k,\mu)\,\tilde{\mathcal{P}}_{g'}(k,\mu)\right) \\
&= \frac{1}{4N_k}\left[\left(\mathcal{P}_{gg'}(k,\mu) + \mathcal{P}_{g'g}(k,\mu)\right)^2 + 4\tilde{\mathcal{P}}_g(k,\mu)\,\tilde{\mathcal{P}}_{g'}(k,\mu)\right] \\
&= \frac{1}{N_k}\left[\left(\mathcal{P}^R_{gg'}(k,\mu)\right)^2 + \tilde{\mathcal{P}}_g(k,\mu)\,\tilde{\mathcal{P}}_{g'}(k,\mu)\right].
\end{aligned} \tag{B.8}$$

in agreement with Eq. (5.16).

Finally, for the mixed covariance, the same process happen, except in this time the second and fourth terms appear with opposite signs. In this case, the noise terms vanish, leaving

$$\begin{aligned}
&\mathrm{Cov}[\hat{\mathcal{P}}^R_{gg'}(k,\mu)\,\hat{\mathcal{P}}^I_{gg'}(k',\mu')] = \left\langle \hat{\mathcal{P}}^R_{gg'}(k,\mu)\,\hat{\mathcal{P}}^I_{gg'}(k',\mu')\right\rangle - \left\langle \hat{\mathcal{P}}^R_{gg'}(k,\mu)\right\rangle \left\langle \hat{\mathcal{P}}^I_{gg'}(k',\mu')\right\rangle \\
&= \frac{1}{4iN_k}\left(\mathcal{P}^2_{gg'}(k,\mu) - \mathcal{P}_{gg'}(k,\mu)\mathcal{P}_{g'g}(k,\mu) + \mathcal{P}_{gg'}(k,\mu)\mathcal{P}_{g'g}(k,\mu) - \mathcal{P}^2_{g'g}(k,\mu)\right) \\
&= \frac{1}{4iN_k}\left(\mathcal{P}^2_{gg'}(k,\mu) - \mathcal{P}^2_{g'g}(k,\mu)\right) \\
&= \frac{1}{N_k}\left(\mathrm{Re}\left[\mathcal{P}_{gg'}(k,\mu)\right]\mathrm{Im}\left[\mathcal{P}_{gg'}(k,\mu)\right]\right),
\end{aligned} \tag{B.9}$$

which matches Eq. (5.20).

There are two important remarks that validate our results. First, when restricting to the case $\boldsymbol{k} = -\boldsymbol{k}'$ in Eq. (B.1), we obtain

$$\mathrm{Cov}[\hat{\mathcal{P}}^I_{gg'}\left(k,\mu\right)\hat{\mathcal{P}}^I_{gg'}\left(k',\mu'\right)] = \frac{1}{N_k}\left[\left(\mathcal{P}^I_{gg'}\left(k,\mu\right)\right)^2 + \tilde{\mathcal{P}}_g(k,\mu)\tilde{\mathcal{P}}_{g'}(k,\mu)\right] \tag{B.10}$$

which coincides with the expression found in [17]. Second, when adding the covariance of the imaginary part Eq. (B.7) to that of the real part Eq. (B.8), we recover the full covariance Eq. (4.35). This confirms that the real and imaginary contributions consistently combine to yield the total covariance, providing an additional check of the correctness of our derivations.

Appendix C

Detecting the Relativistic Doppler Effect with Auto- and Cross-Power Spectra

To verify the consistency of our results, we reproduced the analysis presented in [16]. This comparison allows us to assess whether our computational methods are consistent with those employed in the literature, to identify and interpret any discrepancies, and to contrast these with the results obtained in the main text.

We begin by outlining the setup adopted in [16], which differs slightly from ours. We then perform the detection significance analysis for A_D and examine whether our results are consistent with theirs. Subsequently, we derive parameter constraints in order to obtain the relative errors reported in their work and compare them to our findings. Finally, we apply our own setup and parameter sets $\boldsymbol{\theta}$ to obtain results that can be directly compared with those presented in the main text.

C.1 Analysis Setup

In that work, the authors carried out both a detection significance and a Fisher analysis of the auto- and cross-correlation, using Eqs. (4.8) and (4.7) to model the respective signals. For the Fisher analysis, however, only the latter was considered. The associated covariance matrices are given by

$$\mathrm{Cov}[\mathcal{P}_g(k), \mathcal{P}_g(k')] = \frac{2}{N_{\boldsymbol{k}}} \tilde{\mathcal{P}}_g^2, \tag{C.1}$$

for the auto-correlation, and by Eq. (4.35) for the cross-correlation, respectively. The authors appear to have employed the same BGS model as in our study, but under the full-sky which correspond corresponds to the idealized case in which the entire celestial sphere is observed equivalent to $\approx$ 41,253 deg^2. They also adopted the parameter set $\boldsymbol{\theta}_1$, albeit in an extended form such that $\boldsymbol{\theta}_1$ (Eq. (5.22)) becomes

$$\boldsymbol{\theta}_{1+} = \{A_N, A_K, A_D\}\,, \tag{C.2}$$

where A_N denotes the linear amplitude, A_K parametrizes the redshift-space distortion, and A_D corresponds to the relativistic Doppler contribution. Accordingly, the observed galaxy overdensity can be written as

$$\delta_{g,\mathrm{obs}}(\boldsymbol{k}) = A_N\, b_g\, \delta_m \;+\; A_K\, f\, \mu^2 \;-\; A_D\, \frac{i f \mathcal{H} \mu}{k}\, \alpha_g. \tag{C.3}$$

C.2 Detection Significance Analysis

The first step in [16] was to quantify the presence of a relativistic Doppler signal in the data and to assess its statistical significance against the null hypothesis of no relativistic contributions. This was achieved using the Δ^2_χ test statistic, which for the cross-power spectrum is given by*

$$\Delta^2_{\chi_{gg'}}(\bar{z}_i) = \sum_{m,n} \frac{\left|\mathcal{P}_{gg'}\left(\bar{z}_i, \mu_m, k_n\right) - \mathcal{P}^{A_D=0}_{gg'}\left(\bar{z}_i, \mu_m, k_n\right)\right|^2}{\Gamma\left(\bar{z}_i, \mu_m, k_n\right)}, \tag{C.4}$$

where $\bar{z}_i$ denotes the central redshift of the bin, and Γ is the covariance matrix given by Eq. (4.35). For the auto-correlation case, one simply sets $g = g'$ and employs Γ as in Eq. (C.1).

The results for each redshift bin are displayed in Fig. (C.1). Our figure closely resembles the left panel of Fig. 2 in [16], as intended†. This comparison demonstrates that our computational methods are consistent with those of [16] (and, by extension, [15]).

In our case, we considered a survey area of 10,000 deg^2, which yields the results shown in Fig. (C.2). As expected, the statistical significance is weaker than in the full-sky case due to the reduced sky coverage. However, the qualitative behavior of the relations between

*We did not adopt this method, as our focus was instead on constraining cosmological parameters.

†There could be minor discrepancies, which could plausibly be attributed to differences in the cosmological model assumed, the use of alternative Boltzmann solvers (e.g. not employing `CAMB`), or other implementation details.

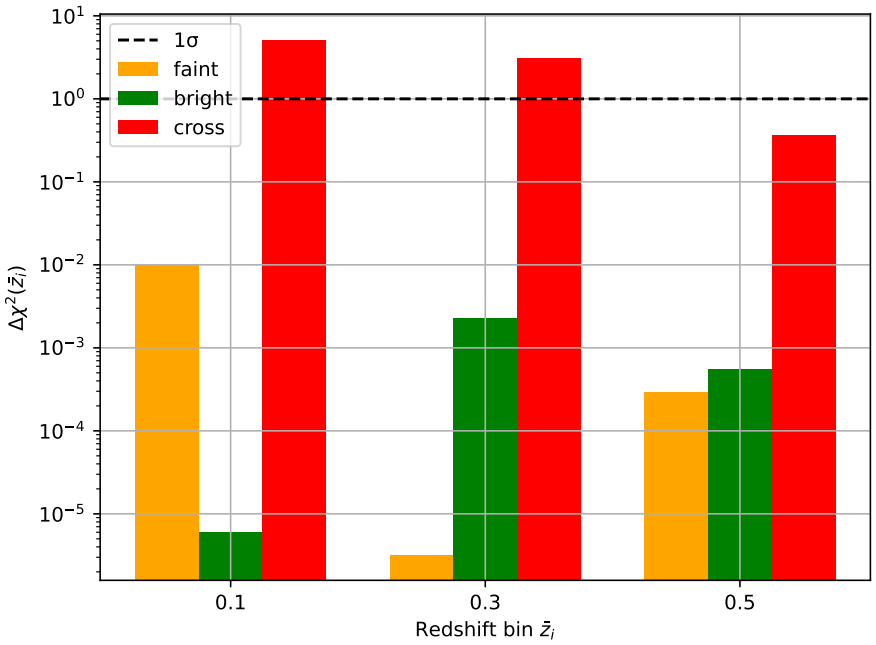


FIGURE C.1: Detection significance of the relativistic Doppler contribution for the model described in Section 5.1, assuming full-sky coverage. The test statistic Δ^2_χ is evaluated with respect to the null hypothesis of no Doppler contribution to the galaxy power spectrum. The colour coding is as follows: orange/yellow for the auto-correlation power spectrum of the faint sample, green for the auto-correlation of the bright sample, and red for the cross-correlation between the faint and bright samples.

the auto-power spectrum and the cross-power spectrum remains the same, in agreement with [16]. It is noteworthy that, even with limited sky coverage, the constraint for $\bar{z}_1$ remains above the $1\,\sigma$ level*.

*In this context, a detection significance above the $1\,\sigma$ level indicates a positive result.

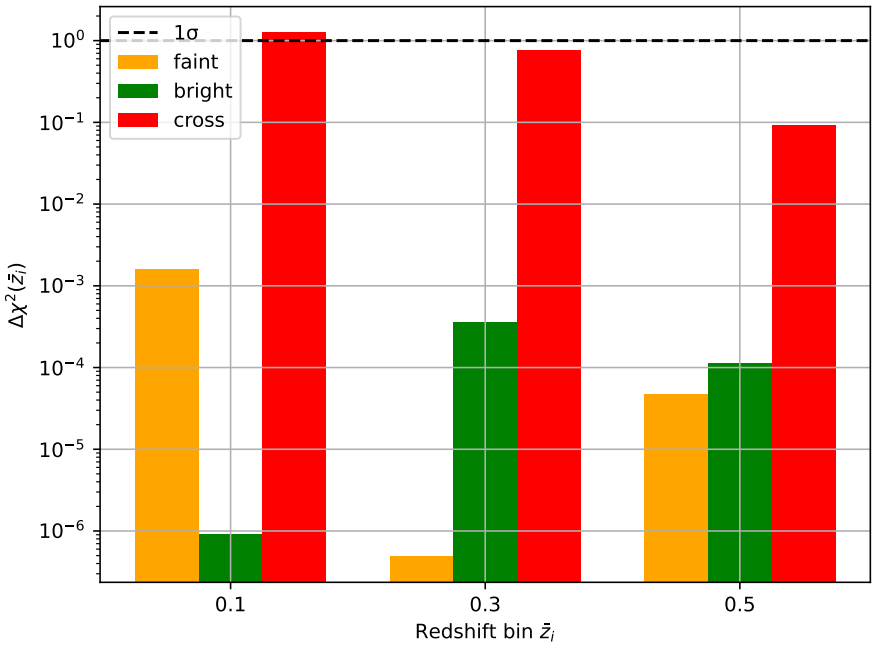


FIGURE C.2: Detection significance of the relativistic Doppler contribution for the model described in Section 5.1. The test statistic Δ^2_χ is evaluated with respect to the null hypothesis of no Doppler contribution to the galaxy power spectrum. The colour coding is as follows: orange/yellow for the auto-correlation power spectrum of the faint sample, green for the auto-correlation of the bright sample, and red for the cross-correlation between the faint and bright samples.

C.3 Parameter Constraints

For the Fisher analysis, [16] employed the extended parameter set $\boldsymbol{\theta}_{1+}$. Their study was primarily focused on optimizing galaxy models in order to obtain the most informative constraints, rather than presenting a detailed discussion of the constraints themselves. Nevertheless, they reported that the marginal error on A_D using our magnitude would be around 0.4, that on A_N is around 0.001, and that on A_K is below 0.01 (see. Figs 5 and 6 of [16]). Since all amplitudes have a fiducial value of unity, the marginal errors correspond directly to relative errors.

In Fig. (C.3), we present bar plots of the relative errors for both the full-sky case and a survey area of 10,000 deg^2, alongside the reference values reported in [16] (shown as horizontal lines). We find that the relative errors on the amplitudes are in line with those reported in [16] (i.e. around or bellow the reference line).

We further confirm that the proportionality between the relative errors of A_K, A_N, and A_D is preserved when the sky coverage is reduced, consistent with the conclusions of the previous section (namely, that decreasing sky coverage degrades the constraints).

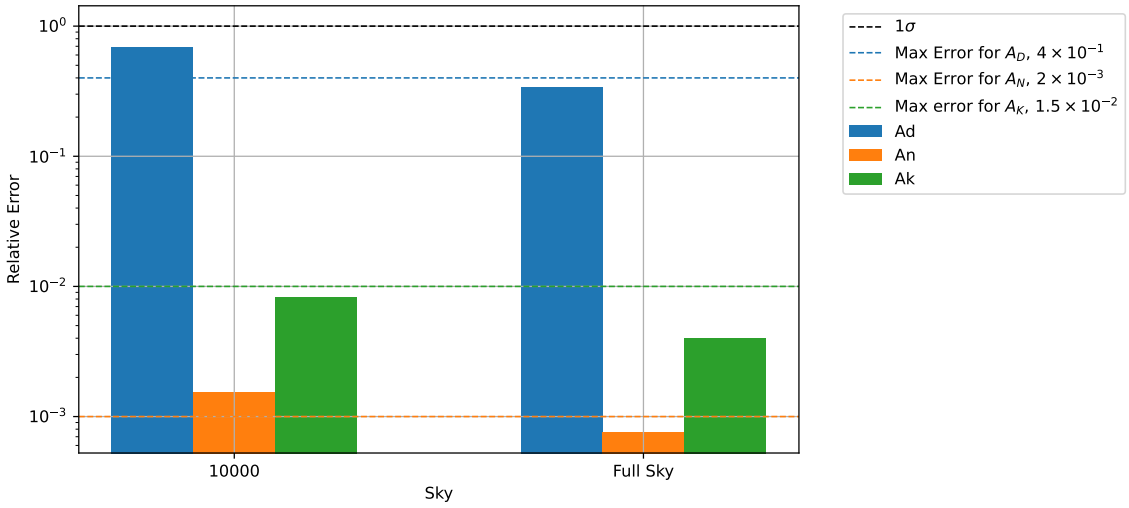


FIGURE C.3: Relative errors on the amplitudes A_N, A_K, and A_D obtained for survey areas of 10,000 deg^2 and full sky coverage. The dashed horizontal lines indicate the maximum errors reported in [16]: A_D 0.4, A_N 0.002, and $A_K < 0.01$. The black dashed line marks the 1σ level.

Moreover, the overall scale of our results remains comparable to that reported in [16], providing additional evidence of consistency. Nevertheless, given the differences in the adopted parameter sets and sky coverage, it is essential to compute parameter constraints tailored to our analysis.

Accordingly, we now focus on our sky coverage (10,000, deg^2) considering the parameter sets $\boldsymbol{\theta}_1$ and $\boldsymbol{\theta}_2$, with the results summarized in Table C.1. We find that the value of A_D obtained with $\boldsymbol{\theta}1$ differs from that obtained with $\boldsymbol{\theta}1+$ only at low decimal. This outcome is consistent with expectations, as the Doppler amplitude is theoretically orthogonal to the other parameters and should remain unaffected [15]. By contrast, we verified that the constraints on the other amplitudes exhibit larger differences (see Fig. C.4), as anticipated for both A_N and A_K.

	A_D	$\alpha_{g,1}$	$\alpha_{g',1}$	$\alpha_{g,2}$	$\alpha_{g',2}$	$\alpha_{g,3}$	$\alpha_{g',3}$
$\mathcal{P}_{gg'}$	0.690	139.8	21.51	33.23	173.1	32.02	58.35

TABLE C.1: Relative errors on the Doppler amplitude A_D of set θ_1 and parameters $\alpha_{g,i}$ and $\alpha_{g',i}$ of set θ_2 obtained from the cross power spectrum $\mathcal{P}_{gg'}$, assuming a survey area of 10,000 deg^2.

Finally, the comparison between the values obtained for $\boldsymbol{\theta}_1$ using the cross-correlation and those reported in the main text is discussed in detail in the main text itself.

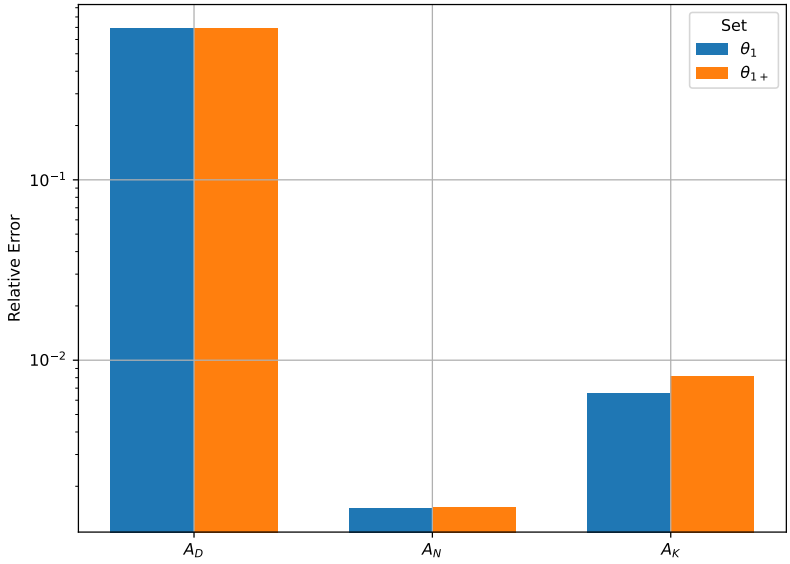


FIGURE C.4: Relative errors on the amplitudes A_N and A_K for the survey area of 10,000 deg^2, obtained using the Doppler-only parameter set θ_1 and the extended set θ_{1+}.

Bibliography

[1] G. Efstathiou, W. J. Sutherland, and S. J. Maddox, "The cosmological constant and cold dark matter," *Nature*, vol. 348, no. 6303, pp. 705–707, Dec. 1990. [Cited on page 1.]

[2] S. Perlmutter, G. Aldering, G. Goldhaber, R. A. Knop, P. Nugent, P. G. Castro, S. Deustua, S. Fabbro, A. Goobar, D. E. Groom, I. M. Hook, A. G. Kim, M. Y. Kim, J. C. Lee, N. J. Nunes, R. Pain, C. R. Pennypacker, R. Quimby, C. Lidman, R. S. Ellis, M. Irwin, R. G. McMahon, P. Ruiz-Lapuente, N. Walton, B. Schaefer, B. J. Boyle, A. V. Filippenko, T. Matheson, A. S. Fruchter, N. Panagia, H. J. M. Newberg, W. J. Couch, and T. S. C. Project, "Measurements of Ω and Λ from 42 High-Redshift Supernovae," *The Astrophysical Journal*, vol. 517, no. 2, pp. 565–586, Jun. 1999. [Cited on page 1.]

[3] A. G. Riess, A. V. Filippenko, P. Challis, A. Clocchiatti, A. Diercks, P. M. Garnavich, R. L. Gilliland, C. J. Hogan, S. Jha, R. P. Kirshner, B. Leibundgut, M. M. Phillips, D. Reiss, B. P. Schmidt, R. A. Schommer, R. C. Smith, J. Spyromilio, C. Stubbs, N. B. Suntzeff, and J. Tonry, "Observational Evidence from Supernovae for an Accelerating Universe and a Cosmological Constant," *The Astronomical Journal*, vol. 116, no. 3, pp. 1009–1038, Sep. 1998. [Cited on page 1.]

[4] S. Dodelson and F. Schmidt, *Modern Cosmology*. Academic Press, 2020. [Cited on pages xv, 1, 5, 8, 13, 14, 17, 23, 29, 30, 31, and 32.]

[5] D. Baumann, *Cosmology*. Cambridge: Cambridge University Press, 2022. [Cited on pages xv, 1, 5, 7, 23, 24, and 31.]

[6] J. Bardeen, J. Bond, N. Kaiser, and A. Szalay, "The Statistics of Peaks of Gaussian Random Fields," *The Astrophysical Journal*, vol. 304, pp. 15–61, May 1986. [Online]. Available: https://ui.adsabs.harvard.edu/abs/1986ApJ...304...15B [Cited on pages 1 and 17.]

[7] N. Kaiser, "Clustering in real space and in redshift space," *Monthly Notices of the Royal Astronomical Society*, vol. 227, no. 1, pp. 1–21, Jul. 1987. [Online]. Available: https://doi.org/10.1093/mnras/227.1.1 [Cited on pages 17, 18, and 19.]

[8] A. Challinor and A. Lewis, "Linear power spectrum of observed source number counts," *Phys. Rev. D*, vol. 84, no. 4, p. 043516, Aug. 2011. [Online]. Available: https://link.aps.org/doi/10.1103/PhysRevD.84.043516 [Cited on pages 13 and 20.]

[9] C. Bonvin and R. Durrer, "What galaxy surveys really measure," *Phys. Rev. D*, vol. 84, no. 6, p. 063505, Sep. 2011. [Online]. Available: https://link.aps.org/doi/10.1103/PhysRevD.84.063505 [Cited on page 21.]

[10] C. Bonvin, "Isolating relativistic effects in large-scale structure," *Classical and Quantum Gravity*, vol. 31, no. 23, p. 234002, Nov. 2014. [Online]. Available: https://dx.doi.org/10.1088/0264-9381/31/23/234002 [Cited on pages 20 and 21.]

[11] E. D. Dio and F. Beutler, "The relativistic galaxy number counts in the weak field approximation," *Journal of Cosmology and Astroparticle Physics*, vol. 2020, no. 09, p. 058–058, Sep. 2020. [Online]. Available: http://dx.doi.org/10.1088/1475-7516/2020/09/058 [Cited on page 1.]

[12] L. R. Abramo and D. Bertacca, "Disentangling the effects of doppler velocity and primordial non-gaussianity in galaxy power spectra," *Phys. Rev. D*, vol. 96, no. 12, p. 123535, Dec. 2017. [Online]. Available: https://link.aps.org/doi/10.1103/PhysRevD.96.123535 [Cited on pages 1, 2, 25, and 27.]

[13] C. Guandalin, J. Adamek, P. Bull, C. Clarkson, L. R. Abramo, and L. Coates, "Observing relativistic features in large-scale structure surveys – i. multipoles of the power spectrum," *Monthly Notices of the Royal Astronomical Society*, vol. 501, no. 2, p. 2547–2561, Dec. 2020. [Online]. Available: http://dx.doi.org/10.1093/mnras/staa3890 [Cited on pages 2, 21, 27, and 28.]

[14] J. Fonseca and C. Clarkson, "Anti-symmetric clustering signals in the observed power spectrum," *Journal of Cosmology and Astroparticle Physics*, vol. 2021, no. 12, p. 003, Dec. 2021. [Online]. Available: http://dx.doi.org/10.1088/1475-7516/2021/12/003 [Cited on page 2.]

[15] F. Montano and S. Camera, "Detecting relativistic doppler by multi-tracing a single galaxy population," *Physics of the Dark Universe*, vol. 46, p. 101634, Dec. 2024. [Online]. Available: https://www.sciencedirect.com/science/article/pii/S2212686424002164 [Cited on pages 3, 20, 21, 22, 26, 30, 31, 33, 35, 36, 40, 41, 43, 50, 54, 55, 66, and 69.]

[16] ——, "Detecting relativistic doppler in galaxy clustering with tailored galaxy samples," *Physics of the Dark Universe*, vol. 46, p. 101570, Dec. 2024. [Online]. Available: https://www.sciencedirect.com/science/article/pii/S2212686424001523 [Cited on pages xvi, 1, 2, 3, 21, 25, 26, 30, 31, 33, 35, 36, 41, 49, 50, 51, 54, 55, 65, 66, 67, 68, and 69.]

[17] P. McDonald, "Gravitational redshift and other redshift-space distortions of the imaginary part of the power spectrum," *Journal of Cosmology and Astroparticle Physics*, vol. 2009, no. 11, p. 026, Nov. 2009. [Online]. Available: https://dx.doi.org/10.1088/1475-7516/2009/11/026 [Cited on pages 2, 34, 39, 40, 54, 55, and 64.]

[18] T. Inoue, T. Okumura, S. Saga, and A. Taruya, "Information content in anisotropic cosmological fields: Impact of different multipole expansion scheme for galaxy density and ellipticity correlations," *Phys. Rev. D*, vol. 111, no. 2, p. 023507, Jan. 2025. [Online]. Available: https://link.aps.org/doi/10.1103/PhysRevD.111.023507 [Cited on pages 2, 27, 33, 35, 44, 50, and 52.]

[19] A. Lewis and A. Challinor, "CAMB: Code for Anisotropies in the Microwave Background," Astrophysics Source Code Library, Feb. 2011. [Online]. Available: https://ui.adsabs.harvard.edu/abs/2011ascl.soft02026L [Cited on page 3.]

[20] E. F. Schlafly, D. Kirkby, D. J. Schlegel, A. D. Myers, A. Raichoor, K. Dawson, J. Aguilar, C. Allende Prieto, S. Bailey, S. BenZvi, J. Bermejo-Climent, D. Brooks, A. de la Macorra, A. Dey, P. Doel, K. Fanning, A. Font-Ribera, J. E. Forero-Romero, J. García-Bellido, S. Gontcho A Gontcho, J. Guy, C. Hahn, K. Honscheid, M. Ishak, S. Juneau, R. Kehoe, T. Kisner, A. Kremin, M. Landriau, D. A. Lang, J. Lasker, M. E. Levi, C. Magneville, C. J. Manser, P. Martini, A. M. Meisner, R. Miquel, J. Moustakas, J. A. Newman, J. Nie, N. Palanque-Delabrouille, W. J. Percival, C. Poppett, C. Rockosi, A. J. Ross, G. Rossi, G. Tarlé, B. A. Weaver, C. Yèche, R. Zhou, and

D. Collaboration, "Survey operations for the dark energy spectroscopic instrument," *The Astronomical Journal*, vol. 166, no. 6, p. 259, Nov. 2023. [Online]. Available: https://dx.doi.org/10.3847/1538-3881/ad0832 [Cited on pages 3, 35, and 54.]

[21] N. Aghanim, Y. Akrami, M. Ashdown, J. Aumont, C. Baccigalupi, M. Ballardini, A. J. Banday, R. B. Barreiro, N. Bartolo, S. Basak, R. Battye, K. Benabed, J.-P. Bernard, M. Bersanelli, P. Bielewicz, J. J. Bock, J. R. Bond, J. Borrill, F. R. Bouchet, F. Boulanger, M. Bucher, C. Burigana, R. C. Butler, E. Calabrese, J.-F. Cardoso, J. Carron, A. Challinor, H. C. Chiang, J. Chluba, L. P. L. Colombo, C. Combet, D. Contreras, B. P. Crill, F. Cuttaia, P. de Bernardis, G. de Zotti, J. Delabrouille, J.-M. Delouis, E. Di Valentino, J. M. Diego, O. Doré, M. Douspis, A. Ducout, X. Dupac, S. Dusini, G. Efstathiou, F. Elsner, T. A. Enßlin, H. K. Eriksen, Y. Fantaye, M. Farhang, J. Fergusson, R. Fernandez-Cobos, F. Finelli, F. Forastieri, M. Frailis, A. A. Fraisse, E. Franceschi, A. Frolov, S. Galeotta, S. Galli, K. Ganga, R. T. Génova-Santos, M. Gerbino, T. Ghosh, J. González-Nuevo, K. M. Górski, S. Gratton, A. Gruppuso, J. E. Gudmundsson, J. Hamann, W. Handley, F. K. Hansen, D. Herranz, S. R. Hildebrandt, E. Hivon, Z. Huang, A. H. Jaffe, W. C. Jones, A. Karakci, E. Keihänen, R. Keskitalo, K. Kiiveri, J. Kim, T. S. Kisner, L. Knox, N. Krachmalnicoff, M. Kunz, H. Kurki-Suonio, G. Lagache, J.-M. Lamarre, A. Lasenby, M. Lattanzi, C. R. Lawrence, M. Le Jeune, P. Lemos, J. Lesgourgues, F. Levrier, A. Lewis, M. Liguori, P. B. Lilje, M. Lilley, V. Lindholm, M. López-Caniego, P. M. Lubin, Y.-Z. Ma, J. F. Macías-Pérez, G. Maggio, D. Maino, N. Mandolesi, A. Mangilli, A. Marcos-Caballero, M. Maris, P. G. Martin, M. Martinelli, E. Martínez-González, S. Matarrese, N. Mauri, J. D. McEwen, P. R. Meinhold, A. Melchiorri, A. Mennella, M. Migliaccio, M. Millea, S. Mitra, M.-A. Miville-Deschênes, D. Molinari, L. Montier, G. Morgante, A. Moss, P. Natoli, H. U. Nørgaard-Nielsen, L. Pagano, D. Paoletti, B. Partridge, G. Patanchon, H. V. Peiris, F. Perrotta, V. Pettorino, F. Piacentini, L. Polastri, G. Polenta, J.-L. Puget, J. P. Rachen, M. Reinecke, M. Remazeilles, A. Renzi, G. Rocha, C. Rosset, G. Roudier, J. A. Rubiño-Martín, B. Ruiz-Granados, L. Salvati, M. Sandri, M. Savelainen, D. Scott, E. P. S. Shellard, C. Sirignano, G. Sirri, L. D. Spencer, R. Sunyaev, A.-S. Suur-Uski, J. A. Tauber, D. Tavagnacco, M. Tenti, L. Toffolatti, M. Tomasi, T. Trombetti, L. Valenziano, J. Valiviita, B. Van Tent, L. Vibert, P. Vielva, F. Villa, N. Vittorio, B. D. Wandelt, I. K. Wehus, M. White, S. D. M. White, A. Zacchei, and A. Zonca, "Planck2018 results:

Vi. cosmological parameters," *Astronomy and Astrophysics*, vol. 641, p. A6, Sep. 2020. [Online]. Available: https://doi.org/10.1051/0004-6361/201833910 [Cited on pages 3, 7, and 9.]

[22] R. Durrer, *The Cosmic Microwave Background*. Cambridge: Cambridge University Press, 2008. [Cited on pages 5 and 14.]

[23] W. J. Percival and B. M. Schäfer, "Galaxy peculiar velocities and evolution-bias," *Monthly Notices of the Royal Astronomical Society: Letters*, vol. 385, no. 1, pp. L78–L82, Mar. 2008. [Online]. Available: https://doi.org/10.1111/j.1745-3933.2008.00437.x [Cited on page 16.]

[24] F. Beutler and E. D. Dio, "Modeling relativistic contributions to the halo power spectrum dipole," *Journal of Cosmology and Astroparticle Physics*, vol. 2020, no. 07, p. 048–048, Jul. 2020. [Online]. Available: http://dx.doi.org/10.1088/1475-7516/2020/07/048 [Cited on pages 22 and 35.]

[25] G. B. Arfken, H. J. Weber, and F. E. Harris, "Chapter 15 - legendre functions," in *Mathematical Methods for Physicists (Seventh Edition)*, seventh edition ed. Boston: Academic Press, 2013, pp. 715–772. [Online]. Available: https://www.sciencedirect.com/science/article/pii/B9780123846549000153 [Cited on page 27.]

[26] J. N. Grieb, A. G. Sánchez, S. Salazar-Albornoz, and C. Dalla Vecchia, "Gaussian covariance matrices for anisotropic galaxy clustering measurements," *Monthly Notices of the Royal Astronomical Society*, vol. 457, no. 2, p. 1577–1592, Feb. 2016. [Online]. Available: http://dx.doi.org/10.1093/mnras/stw065 [Cited on pages 32 and 33.]

[27] A. Heavens, "Statistical techniques in cosmology," Jun. 2010. [Online]. Available: https://arxiv.org/abs/0906.0664 [Cited on pages 35, 42, and 43.]

[28] M. Abdul Karim, J. Aguilar, S. Ahlen, S. Alam, L. Allen, C. A. Prieto, O. Alves, A. Anand, U. Andrade, E. Armengaud, A. Aviles, S. Bailey, C. Baltay, P. Bansal, A. Bault, J. Behera, S. BenZvi, D. Bianchi, C. Blake, S. Brieden, A. Brodzeller, D. Brooks, E. Buckley-Geer, E. Burtin, R. Calderon, R. Canning, A. C. Rosell, P. Carrilho, L. Casas, F. J. Castander, M. Charles, E. Chaussidon, J. Chaves-Montero, D. Chebat, X. Chen, T. Claybaugh, S. Cole, A. P. Cooper, A. Cuceu, K. S. Dawson, A. de la Macorra, A. de Mattia, N. Deiosso, J. Della Costa, R. Demina, A. Dey,

B. Dey, Z. Ding, P. Doel, J. Edelstein, D. J. Eisenstein, W. Elbers, P. Fagrelius, K. Fanning, E. Fernández-García, S. Ferraro, A. Font-Ribera, J. E. Forero-Romero, C. S. Frenk, C. Garcia-Quintero, L. H. Garrison, E. Gaztañaga, H. Gil-Marín, S. G. A. Gontcho, D. Gonzalez, A. X. Gonzalez-Morales, C. Gordon, D. Green, G. Gutierrez, J. Guy, B. Hadzhiyska, C. Hahn, S. He, M. Herbold, H. K. Herrera-Alcantar, M.-F. Ho, K. Honscheid, C. Howlett, D. Huterer, M. Ishak, S. Juneau, N. V. Kamble, N. G. Karaçayl*i*, R. Kehoe, S. Kent, A. G. Kim, D. Kirkby, T. Kisner, S. E. Koposov, A. Kremin, A. Krolewski, O. Lahav, C. Lamman, M. Landriau, D. Lang, J. Lasker, J. M. Le Goff, L. Le Guillou, A. Leauthaud, M. E. Levi, Q. Li, T. S. Li, K. Lodha, M. Lokken, F. Lozano-Rodríguez, C. Magneville, M. Manera, P. Martini, W. L. Matthewson, A. Meisner, J. Mena-Fernández, A. Menegas, T. Mergulhão, R. Miquel, J. Moustakas, A. Muñoz Gutiérrez, D. Muñoz Santos, A. D. Myers, S. Nadathur, K. Naidoo, L. Napolitano, J. A. Newman, G. Niz, H. E. Noriega, E. Paillas, N. Palanque-Delabrouille, J. Pan, J. A. Peacock, M. P. Ibanez, W. J. Percival, A. Pérez-Fernández, I. Pérez-Ràfols, M. M. Pieri, C. Poppett, F. Prada, D. Rabinowitz, A. Raichoor, C. Ramírez-Pérez, M. Rashkovetskyi, C. Ravoux, J. Rich, A. Rocher, C. Rockosi, J. Rohlf, J. O. Román-Herrera, A. J. Ross, G. Rossi, R. Ruggeri, V. Ruhlmann-Kleider, L. Samushia, E. Sanchez, N. Sanders, D. Schlegel, M. Schubnell, H. Seo, A. Shafieloo, R. Sharples, J. Silber, F. Sinigaglia, D. Sprayberry, T. Tan, G. Tarlé, P. Taylor, W. Turner, L. A. Ureña López, R. Vaisakh, F. Valdes, G. Valogiannis, M. Vargas-Magaña, L. Verde, M. Walther, B. A. Weaver, D. H. Weinberg, M. White, M. Wolfson, C. Yèche, J. Yu, E. A. Zaborowski, P. Zarrouk, Z. Zhai, H. Zhang, C. Zhao, G. B. Zhao, R. Zhou, and H. Zou, "Desi dr2 results. ii. measurements of baryon acoustic oscillations and cosmological constraints," *Phys. Rev. D*, vol. 112, p. 083515, Oct 2025. [Online]. Available: https://link.aps.org/doi/10.1103/tr6y-kpc6 [Cited on page 36.]

[29] S. Yahia-Cherif, A. Blanchard, S. Camera, S. Casas, S. Ilić, K. Marković, A. Pourtsidou, Z. Sakr, D. Sapone, and I. Tutusaus, "Validating the fisher approach for stage iv spectroscopic surveys," *Astronomy and Astrophysics*, vol. 649, p. A52, May 2021. [Online]. Available: http://dx.doi.org/10.1051/0004-6361/201937312 [Cited on pages 37 and 50.]

[30] A. Taruya, S. Saito, and T. Nishimichi, "Forecasting the cosmological constraints with anisotropic baryon acoustic oscillations from multipole expansion," *Phys.*

Rev. D, vol. 83, no. 10, p. 103527, May 2011. [Online]. Available: https://link.aps.org/doi/10.1103/PhysRevD.83.103527 [Cited on page 52.]

[31] E. Collaboration, Y. Mellier, Abdurro'uf, J. A. A. Barroso, A. Achúcarro, J. Adamek, R. Adam, G. E. Addison, N. Aghanim, M. Aguena, V. Ajani, Y. Akrami, A. Al-Bahlawan, A. Alavi, I. S. Albuquerque, G. Alestas, G. Alguero, A. Allaoui, S. W. Allen, V. Allevato, A. V. Alonso-Tetilla, B. Altieri, A. Alvarez-Candal, S. Alvi, A. Amara, L. Amendola, J. Amiaux, I. T. Andika, S. Andreon, A. Andrews, G. Angora, R. E. Angulo, F. Annibali, A. Anselmi, S. Anselmi, S. Arcari, M. Archidiacono, G. Aricò, M. Arnaud, S. Arnouts, M. Asgari, J. Asorey, L. Atayde, H. Atek, F. Atrio-Barandela, M. Aubert, E. Aubourg, T. Auphan, N. Auricchio, B. Aussel, H. Aussel, P. P. Avelino, A. Avgoustidis, S. Avila, S. Awan, R. Azzollini, C. Baccigalupi, E. Bachelet, D. Bacon, M. Baes, M. B. Bagley, B. Bahr-Kalus, A. Balaguera-Antolinez, E. Balbinot, M. Balcells, M. Baldi, I. Baldry, A. Balestra, M. Ballardini, O. Ballester, M. Balogh, E. Bañados, R. Barbier, S. Bardelli, M. Baron, T. Barreiro, R. Barrena, J. C. Barriere, B. J. Barros, A. Barthelemy, N. Bartolo, A. Basset, P. Battaglia, A. J. Battisti, C. M. Baugh, L. Baumont, L. Bazzanini, J. P. Beaulieu, V. Beckmann, A. N. Belikov, J. Bel, F. Bellagamba, M. Bella, E. Bellini, K. Benabed, R. Bender, G. Benevento, C. L. Bennett, K. Benson, P. Bergamini, J. R. Bermejo-Climent, F. Bernardeau, D. Bertacca, M. Berthe, J. Berthier, M. Bethermin, F. Beutler, C. Bevillon, S. Bhargava, R. Bhatawdekar, D. Bianchi, L. Bisigello, A. Biviano, R. P. Blake, A. Blanchard, J. Blazek, L. Blot, A. Bosco, C. Bodendorf, T. Boenke, H. Böhringer, P. Boldrini, M. Bolzonella, A. Bonchi, M. Bonici, D. Bonino, L. Bonino, C. Bonvin, W. Bon, J. T. Booth, S. Borgani, A. S. Borlaff, E. Borsato, A. Bosco, B. Bose, M. T. Botticella, A. Boucaud, F. Bouche, J. S. Boucher, D. Boutigny, T. Bouvard, R. Bouwens, H. Bouy, R. A. A. Bowler, V. Bozza, E. Bozzo, E. Branchini, G. Brando, S. Brau-Nogue, P. Brekke, M. N. Bremer, M. Brescia, M. A. Breton, J. Brinchmann, T. Brinckmann, C. Brockley-Blatt, M. Brodwin, L. Brouard, M. L. Brown, S. Bruton, J. Bucko, H. Buddelmeijer, G. Buenadicha, F. Buitrago, P. Burger, C. Burigana, V. Busillo, D. Busonero, R. Cabanac, L. Cabayol-Garcia, M. S. Cagliari, A. Caillat, L. Caillat, M. Calabrese, A. Calabro, G. Calderone, F. Calura, B. C. Quevedo, S. Camera, L. Campos, G. Canas-Herrera, G. P. Candini, M. Cantiello, V. Capobianco, E. Cappellaro, N. Cappelluti, A. Cappi, K. I. Caputi, C. Cara, C. Carbone, V. F. Cardone, E. Carella, R. G. Carlberg, M. Carle, L. Carminati,

F. Caro, J. M. Carrasco, J. Carretero, P. Carrilho, J. C. Duque, B. Carry, A. Carvalho, C. S. Carvalho, R. Casas, S. Casas, P. Casenove, C. M. Casey, P. Cassata, F. J. Castander, D. Castelao, M. Castellano, L. Castiblanco, G. Castignani, T. Castro, C. Cavet, S. Cavuoti, P. Y. Chabaud, K. C. Chambers, Y. Charles, S. Charlot, N. Chartab, R. Chary, F. Chaumeil, H. Cho, G. Chon, E. Ciancetta, P. Ciliegi, A. Cimatti, M. Cimino, M. R. L. Cioni, R. Claydon, C. Cleland, B. Clément, D. L. Clements, N. Clerc, S. Clesse, S. Codis, F. Cogato, J. Colbert, R. E. Cole, P. Coles, T. E. Collett, R. S. Collins, C. Colodro-Conde, C. Colombo, F. Combes, V. Conforti, G. Congedo, S. Conseil, C. J. Conselice, S. Contarini, T. Contini, L. Conversi, A. R. Cooray, Y. Copin, P. S. Corasaniti, P. Corcho-Caballero, L. Corcione, O. Cordes, O. Corpace, M. Correnti, M. Costanzi, A. Costille, F. Courbin, L. C. Mifsud, H. M. Courtois, M. C. Cousinou, G. Covone, T. Cowell, C. Cragg, G. Cresci, S. Cristiani, M. Crocce, M. Cropper, P. E. Crouzet, B. Csizi, J. G. Cuby, E. Cucchetti, O. Cucciati, J. C. Cuillandre, P. A. C. Cunha, V. Cuozzo, E. Daddi, M. D'Addona, C. Dafonte, N. Dagoneau, E. Dalessandro, G. B. Dalton, G. D'Amico, H. Dannerbauer, P. Danto, I. Das, A. D. Silva, R. da Silva, W. d'Assignies Doumerg, G. Daste, J. E. Davies, S. Davini, P. Dayal, T. de Boer, R. Decarli, B. D. Caro, H. Degaudenzi, G. Degni, J. T. A. de Jong, L. F. de la Bella, S. de la Torre, F. Delhaise, D. Delley, G. Delucchi, G. D. Lucia, J. Denniston, F. D. Paolis, M. D. Petris, A. Derosa, S. Desai, V. Desjacques, G. Despali, G. Desprez, J. D. Vicente-Albendea, Y. Deville, J. D. F. Dias, A. Díaz-Sánchez, J. J. Diaz, S. D. Domizio, J. M. Diego, D. D. Ferdinando, A. M. D. Giorgio, P. Dimauro, J. Dinis, K. Dolag, C. Dolding, H. Dole, H. D. Sánchez, O. Doré, F. Dournac, M. Douspis, H. Dreihahn, B. Droge, B. Dryer, F. Dubath, P. A. Duc, F. Ducret, C. Duffy, F. Dufresne, C. A. J. Duncan, X. Dupac, V. Duret, R. Durrer, F. Durret, S. Dusini, A. Ealet, A. Eggemeier, P. R. M. Eisenhardt, D. Elbaz, M. Y. Elkhashab, A. Ellien, J. Endicott, A. Enia, T. Erben, J. A. E. Vigo, S. Escoffier, I. E. Sanz, J. Essert, S. Ettori, M. Ezziati, G. Fabbian, M. Fabricius, Y. Fang, A. Farina, M. Farina, R. Farinelli, S. Farrens, F. Faustini, A. Feltre, A. M. N. Ferguson, P. Ferrando, A. G. Ferrari, A. Ferré-Mateu, P. G. Ferreira, I. Ferreras, I. Ferrero, S. Ferriol, P. Ferruit, D. Filleul, F. Finelli, S. L. Finkelstein, A. Finoguenov, B. Fiorini, F. Flentge, P. Focardi, J. Fonseca, A. Fontana, F. Fontanot, F. Fornari, P. Fosalba, M. Fossati, S. Fotopoulou, D. Fouchez, N. Fourmanoit, M. Frailis, D. Fraix-Burnet, E. Franceschi, A. Franco, P. Franzetti, J. Freihoefer, C. . S. Frenk,

G. Frittoli, P. A. Frugier, N. Frusciante, A. Fumagalli, M. Fumagalli, M. Fumana, Y. Fu, L. Gabarra, S. Galeotta, L. Galluccio, K. Ganga, H. Gao, J. García-Bellido, K. Garcia, J. P. Gardner, B. Garilli, L. M. Gaspar-Venancio, T. Gasparetto, V. Gautard, R. Gavazzi, E. Gaztanaga, L. Genolet, R. G. Santos, F. Gentile, K. George, M. Gerbino, Z. Ghaffari, F. Giacomini, F. Gianotti, G. P. S. Gibb, W. Gillard, B. Gillis, M. Ginolfi, C. Giocoli, M. Girardi, S. K. Giri, L. W. K. Goh, P. Gómez-Alvarez, V. Gonzalez-Perez, A. H. Gonzalez, E. J. Gonzalez, J. C. Gonzalez, S. G. Beauchamps, G. Gozaliasl, J. Gracia-Carpio, S. Grandis, B. R. Granett, M. Granvik, A. Grazian, A. Gregorio, C. Grenet, C. Grillo, F. Grupp, C. Gruppioni, A. Gruppuso, C. Guerbuez, S. Guerrini, M. Guidi, P. Guillard, C. M. Gutierrez, P. Guttridge, L. Guzzo, S. Gwyn, J. Haapala, J. Haase, C. R. Haddow, M. Hailey, A. Hall, D. Hall, N. Hamaus, B. S. Haridasu, J. Harnois-Déraps, C. Harper, W. G. Hartley, G. Hasinger, F. Hassani, N. A. Hatch, S. V. H. Haugan, B. Häußler, A. Heavens, L. Heisenberg, A. Helmi, G. Helou, S. Hemmati, K. Henares, O. Herent, C. Hernández-Monteagudo, T. Heuberger, P. C. Hewett, S. Heydenreich, H. Hildebrandt, M. Hirschmann, J. Hjorth, J. Hoar, H. Hoekstra, A. D. Holland, M. S. Holliman, W. Holmes, I. Hook, B. Horeau, F. Hormuth, A. Hornstrup, S. Hosseini, D. Hu, P. Hudelot, M. J. Hudson, M. Huertas-Company, E. M. Huff, A. C. N. Hughes, A. Humphrey, L. K. Hunt, D. D. Huynh, R. Ibata, K. Ichikawa, S. Iglesias-Groth, O. Ilbert, S. Ilić, L. Ingoglia, E. Iodice, H. Israel, U. E. Israelsson, L. Izzo, P. Jablonka, N. Jackson, J. Jacobson, M. Jafariyazani, K. Jahnke, B. Jain, H. Jansen, M. J. Jarvis, J. Jasche, M. Jauzac, N. Jeffrey, M. Jhabvala, Y. Jimenez-Teja, A. J. Muñoz, B. Joachimi, P. H. Johansson, S. Joudaki, E. Jullo, J. J. E. Kajava, Y. Kang, A. Kannawadi, V. Kansal, D. Karagiannis, M. Kärcher, A. Kashlinsky, M. V. Kazandjian, F. Keck, E. Keihänen, E. Kerins, S. Kermiche, A. Khalil, A. Kiessling, K. Kiiveri, M. Kilbinger, J. Kim, R. King, C. C. Kirkpatrick, T. Kitching, M. Kluge, M. Knabenhans, J. H. Knapen, A. Knebe, J. P. Kneib, R. Kohley, L. V. E. Koopmans, H. Koskinen, E. Koulouridis, R. Kou, A. Kovács, I. Kovačić, A. Kowalczyk, K. Koyama, K. Kraljic, O. Krause, S. Kruk, B. Kubik, U. Kuchner, K. Kuijken, M. Kümmel, M. Kunz, H. Kurki-Suonio, F. Lacasa, C. G. Lacey, F. L. Franca, N. Lagarde, O. Lahav, C. Laigle, A. L. Marca, O. L. Marle, B. Lamine, M. C. Lam, A. Lançon, H. Landt, M. Langer, A. Lapi, C. Larcheveque, S. S. Larsen, M. Lattanzi, F. Laudisio, D. Laugier, R. Laureijs, V. Laurent, G. Lavaux, A. Lawrenson, A. Lazanu, T. Lazeyras, Q. L. Boulc'h, A. M. C. L. Brun, V. L. Brun,

F. Leclercq, S. Lee, J. L. Graet, L. Legrand, K. N. Leirvik, M. L. Jeune, M. Lembo, D. L. Mignant, M. D. Lepinzan, F. Lepori, A. L. Reun, G. Leroy, G. F. Lesci, J. Lesgourgues, L. Leuzzi, M. E. Levi, T. I. Liaudat, G. Libet, P. Liebing, S. Ligori, P. B. Lilje, C. C. Lin, D. Linde, E. Linder, V. Lindholm, L. Linke, S. S. Li, S. J. Liu, I. Lloro, F. S. N. Lobo, N. Lodieu, M. Lombardi, L. Lombriser, P. Lonare, G. Longo, M. López-Caniego, X. L. Lopez, J. L. Alvarez, A. Loureiro, J. Loveday, E. Lusso, J. Macias-Perez, T. Maciaszek, G. Maggio, M. Magliocchetti, F. Magnard, E. A. Magnier, A. Magro, G. Mahler, G. Mainetti, D. Maino, E. Maiorano, E. Maiorano, N. Malavasi, G. A. Mamon, C. Mancini, R. Mandelbaum, M. Manera, A. Manjón-García, F. Mannucci, O. Mansutti, M. M. Outeiro, R. Maoli, C. Maraston, S. Marcin, P. Marcos-Arenal, B. Margalef-Bentabol, O. Marggraf, D. Marinucci, M. Marinucci, K. Markovic, F. R. Marleau, J. Marpaud, J. Martignac, J. Martín-Fleitas, P. Martin-Moruno, E. L. Martin, M. Martinelli, N. Martinet, H. Martin, C. J. A. P. Martins, F. Marulli, D. Massari, R. Massey, D. C. Masters, S. Matarrese, Y. Matsuoka, S. Matthew, B. J. Maughan, N. Mauri, L. Maurin, S. Maurogordato, K. McCarthy, A. W. McConnachie, H. J. McCracken, I. McDonald, J. D. McEwen, C. J. R. McPartland, E. Medinaceli, V. Mehta, S. Mei, M. Melchior, J. B. Melin, B. Ménard, J. Mendes, J. Mendez-Abreu, M. Meneghetti, A. Mercurio, E. Merlin, R. B. Metcalf, G. Meylan, M. Migliaccio, M. Mignoli, L. Miller, M. Miluzio, B. Milvang-Jensen, J. P. Mimoso, R. Miquel, H. Miyatake, B. Mobasher, J. J. Mohr, P. Monaco, M. Monguió, A. Montoro, A. Mora, A. M. Dizgah, M. Moresco, C. Moretti, G. Morgante, N. Morisset, T. J. Moriya, P. W. Morris, D. J. Mortlock, L. Moscardini, D. F. Mota, S. Mottet, L. A. Moustakas, T. Moutard, T. Müller, E. Munari, G. Murphree, C. Murray, N. Murray, P. Musi, S. Nadathur, B. C. Nagam, T. Nagao, K. Naidoo, R. Nakajima, C. Nally, P. Natoli, A. Navarro-Alsina, D. N. Girones, C. Neissner, A. Nersesian, S. Nesseris, H. N. Nguyen-Kim, L. Nicastro, R. C. Nichol, M. Nielbock, S. M. Niemi, S. Nieto, K. Nilsson, J. Noller, P. Norberg, A. Nouri-Zonoz, P. Ntelis, A. A. Nucita, P. Nugent, N. J. Nunes, T. Nutma, I. Ocampo, J. Odier, P. A. Oesch, M. Oguri, D. M. Oliveira, M. Onoue, T. Oosterbroek, F. Oppizzi, C. Ordenovic, K. Osato, F. Pacaud, F. Pace, C. Padilla, K. Paech, L. Pagano, M. J. Page, E. Palazzi, S. Paltani, S. Pamuk, S. Pandolfi, D. Paoletti, M. Paolillo, P. Papaderos, K. Pardede, G. Parimbelli, A. Parmar, C. Partmann, F. Pasian, F. Passalacqua, K. Paterson, L. Patrizii, C. Pattison, A. Paulino-Afonso, R. Paviot, J. A. Peacock, F. R. Pearce,

K. Pedersen, A. Peel, R. F. Peletier, M. P. Ibanez, R. Pello, M. T. Penny, W. J. Percival, A. Perez-Garrido, L. Perotto, V. Pettorino, A. Pezzotta, S. Pezzuto, A. Philippon, M. Pierre, O. Piersanti, M. Pietroni, L. Piga, L. Pilo, S. Pires, A. Pisani, A. Pizzella, L. Pizzuti, C. Plana, G. Polenta, J. E. Pollack, M. Poncet, M. Pöntinen, P. Pool, L. A. Popa, V. Popa, J. Popp, C. Porciani, L. Porth, D. Potter, M. Poulain, A. Pourtsidou, L. Pozzetti, I. Prandoni, G. W. Pratt, S. Prezelus, E. Prieto, A. Pugno, S. Quai, L. Quilley, G. D. Racca, A. Raccanelli, G. Rácz, S. Radinović, M. Radovich, A. Ragagnin, U. Ragnit, F. Raison, N. Ramos-Chernenko, C. Ranc, Y. Rasera, N. Raylet, R. Rebolo, A. Refregier, P. Reimberg, T. H. Reiprich, F. Renk, A. Renzi, J. Retre, Y. Revaz, C. Reylé, L. Reynolds, J. Rhodes, F. Ricci, M. Ricci, G. Riccio, S. O. Ricken, S. Rissanen, I. Risso, H. W. Rix, A. C. Robin, B. Rocca-Volmerange, P. F. Rocci, M. Rodenhuis, G. Rodighiero, M. R. Monroy, R. P. Rollins, M. Romanello, J. Roman, E. Romelli, M. Romero-Gomez, M. Roncarelli, P. Rosati, C. Rosset, E. Rossetti, W. Roster, H. J. A. Rottgering, A. Rozas-Fernández, K. Ruane, J. A. Rubino-Martin, A. Rudolph, F. Ruppin, B. Rusholme, S. Sacquegna, I. Sáez-Casares, S. Saga, R. Saglia, M. Sahlén, T. Saifollahi, Z. Sakr, J. Salvalaggio, R. Salvaterra, L. Salvati, M. Salvato, J. C. Salvignol, A. G. Sánchez, E. Sanchez, D. B. Sanders, D. Sapone, M. Saponara, E. Sarpa, F. Sarron, S. Sartori, B. Sartoris, B. Sassolas, L. Sauniere, M. Sauvage, M. Sawicki, R. Scaramella, C. Scarlata, L. Scharré, J. Schaye, J. A. Schewtschenko, J. T. Schindler, E. Schinnerer, M. Schirmer, F. Schmidt, F. Schmidt, M. Schmidt, A. Schneider, M. Schneider, P. Schneider, N. Schöneberg, T. Schrabback, M. Schultheis, S. Schulz, N. Schuster, J. Schwartz, D. Sciotti, M. Scodeggio, D. Scognamiglio, D. Scott, V. Scottez, A. Secroun, E. Sefusatti, G. Seidel, M. Seiffert, E. Sellentin, M. Selwood, E. Semboloni, M. Sereno, S. Serjeant, S. Serrano, G. Setnikar, F. Shankar, R. M. Sharples, A. Short, A. Shulevski, M. Shuntov, M. Sias, G. Sikkema, A. Silvestri, P. Simon, C. Sirignano, G. Sirri, J. Skottfelt, E. Slezak, D. Sluse, G. P. Smith, L. C. Smith, R. E. Smith, S. J. A. Smit, F. Soldano, B. G. B. Solheim, J. G. Sorce, F. Sorrenti, E. Soubrie, L. Spinoglio, A. S. Mancini, J. Stadel, L. Stagnaro, L. Stanco, S. A. Stanford, J. L. Starck, P. Stassi, J. Steinwagner, D. Stern, C. Stone, P. Strada, F. Strafella, D. Stramaccioni, C. Surace, F. Sureau, S. H. Suyu, I. Swindells, M. Szafraniec, I. Szapudi, S. Taamoli, M. Talia, P. Tallada-Crespí, K. Tanidis, C. Tao, P. Tarrío, D. Tavagnacco, A. N. Taylor, J. E. Taylor, P. L. Taylor, E. M. Teixeira, M. Tenti, P. T. Idiago, H. I. Teplitz, I. Tereno,

N. Tessore, V. Testa, G. Testera, M. Tewes, R. Teyssier, N. Theret, C. Thizy, P. D. Thomas, Y. Toba, S. Toft, R. Toledo-Moreo, E. Tolstoy, E. Tommasi, O. Torbaniuk, F. Torradeflot, C. Tortora, S. Tosi, S. Tosti, M. Trifoglio, A. Troja, T. Trombetti, A. Tronconi, M. Tsedrik, A. Tsyganov, M. Tucci, I. Tutusaus, C. Uhlemann, L. Ulivi, M. Urbano, L. Vacher, L. Vaillon, P. Valageas, I. Valdes, E. A. Valentijn, L. Valenziano, C. Valieri, J. Valiviita, M. V. den Broeck, T. Vassallo, R. Vavrek, J. Vega-Ferrero, B. Venemans, A. Venhola, S. Ventura, G. V. Kleijn, D. Vergani, A. Verma, F. Vernizzi, A. Veropalumbo, G. Verza, C. Vescovi, D. Vibert, M. Viel, P. Vielzeuf, C. Viglione, A. Viitanen, F. Villaescusa-Navarro, S. Vinciguerra, F. Visticot, K. Voggel, M. von Wietersheim-Kramsta, W. J. Vriend, S. Wachter, M. Walmsley, G. Walth, D. M. Walton, N. A. Walton, M. Wander, L. Wang, Y. Wang, J. R. Weaver, J. Weller, M. Wetzstein, D. J. Whalen, I. H. Whittam, A. Widmer, M. Wiesmann, J. Wilde, O. R. Williams, H. A. Winther, A. Wittje, J. H. W. Wong, A. H. Wright, V. Yankelevich, H. W. Yeung, M. Yoon, S. Youles, L. Y. A. Yung, A. Zacchei, L. Zalesky, G. Zamorani, A. Z. Vitorelli, M. Z. Marc, M. Zennaro, F. M. Zerbi, I. A. Zinchenko, J. Zoubian, E. Zucca, and M. Zumalacarregui, "Euclid. i. overview of the euclid mission," *Astronomy and Astrophysics*, vol. 697, p. A1, Apr. 2025. [Online]. Available: https://doi.org/10.1051/0004-6361/202450810 [Cited on page 54.]

[32] L. F. Secco, "Estimadores do espectro de potência em levantamentos de galáxias," Master's Dissertation in Física, Instituto de Física, University of São Paulo, São Paulo, 2015, [Acesso em 2025-09-27]. [Online]. Available: http://www.teses.usp.br/teses/disponiveis/43/43134/tde-05072018-171414/pt-br.php [Cited on page 57.]